THE GEOLOGICAL SOCIETY
OF AMERICA®

Petrogenesis of the cogenetic Stewart pegmatite-aplite, Pala, California: Regional implications

Douglas M. Morton[1], J. Blue Sheppard[2], Fred K. Miller[3], and Cin-Ty A. Lee[4]
[1]U.S. GEOLOGICAL SURVEY AND DEPARTMENT OF EARTH SCIENCES, UNIVERSITY OF CALIFORNIA, RIVERSIDE, CALIFORNIA 92521, USA
[2]STEWART LITHIA MINES, P.O. BOX 382, PALA, CALIFORNIA 92059, USA
[3]U.S. GEOLOGICAL SURVEY, SPOKANE, WASHINGTON 99201, USA
[4]DEPARTMENT OF EARTH, ENVIRONMENTAL, AND PLANETARY SCIENCES, RICE UNIVERSITY, HOUSTON, TEXAS 77005, USA

ABSTRACT

The Stewart pegmatite-aplite dike in Pala, California (USA) is well known as a source of lithium, gem minerals, and unusual phosphate minerals. We reinterpret the petrogenesis of the dike based on a combination of new regional and detailed geochemical isotopic and textural data. The Stewart dike, like other pegmatites in the Pala district and other major pegmatite districts in the northern Peninsular Ranges batholith, is enclosed within gabbro/mafic tonalite. The $^{40}Ar/^{39}Ar$ method of dating on muscovite from the dike, and U/Pb dating of zircon from the gabbro yield essentially the same age. Initial $^{87}Sr/^{86}Sr$ is similar for the dike, 0.7042, and the gabbro, 0.7036–0.7037, indicating a juvenile and likely common source for both.

The extreme mineralogic, lithologic, and textural variations within the dike are interpreted to have resulted from in situ mineral segregation, autometasomatism, and migration of volatiles within an essentially closed system. Contacts between the pegmatite dike and the host gabbro are diffuse.

All previous interpretations of the Stewart pegmatite dike invoked an allogenic origin, formed by fluids derived externally from a nearby or distant granitic body, with the fluids subsequently migrating to, and intruding, their gabbro/mafic tonalite host. These previously proposed sources of pegmatite-forming fluid(s) are ruled out here on the basis of similar ages of the host and pegmatite, similar initial $^{87}Sr/^{86}Sr$ isotopes, unrealistic 25–40 km distances between any proposed potential source and the host gabbro-tonalite pluton, and mineralogic and textural relationships indicating internal differentiation. For these reasons, we suggest an autogenic origin, whereby the gem-bearing pegmatites are petrogenetically limited to their gabbroic hosts and likely represent late-stage, internal segregation of magmatic fluids. We note that nearly every gem-bearing pegmatite in the northern Peninsular Ranges batholith is hosted within gabbro/mafic tonalite bodies, not within the more silicic plutons.

INTRODUCTION

The Stewart pegmatite-aplite, Pala pegmatite district, is located 2 km northeast of Pala, San Diego County, California. It is well known as a source of gem minerals, lithium, and a number of unusual minerals, attracting the attention of petrologists, mineralogists, and gemologists for more than 100 years (e.g., Fairbanks, 1893; Kunz, 1905; Schaller, 1912).

There have been numerous and conflicting interpretations of the petrogenesis of the Stewart dike. However, they all invoke an allogenic source of the pegmatite-forming fluid(s) for the Pala district pegmatites, and other major lithium-bearing pegmatite districts in San Diego County, from designated or undesignated nearby granitic bodies, not from the gabbroic plutons in which the pegmatites are hosted (e.g., Jahns and Wright, 1951; Taylor et al., 1979, Foord and Shigley, 1991; Webber et al., 1999; Patterson, 2009). Interpretations for the emplacement of the Stewart dike pegmatite-forming melt range from a single magma injection to 10 or more over weeks to years. Internal deformation features within the dike have been misinterpreted to represent repeated magma injections.

Based on regional geologic setting, new chemical and isotopic data, detailed subsurface studies, and detailed rock and mineral chemistry, we

clarify some of the fundamental aspects of the dike's paragenesis. Our primary goals were to determine the source of the pegmatite-forming fluid, the crystallization and structural history, and the nature and spatial extent of metasomatism. Like most other studies of the Stewart dike, we focused on the southern part, because it has the best surface and subsurface exposures and appears to have the most completely developed textural and mineralogical zonation.

GEOLOGIC SETTING

The Stewart dike is located within the northern Peninsular Ranges batholith (NPRB) (Fig. 1). North of 33°N, the NPRB includes a number of well-known complex pegmatite districts that include world-class gem- and lithium-bearing pegmatites and rare earth element (REE)–bearing pegmatites. The NPRB consists of four autochthonous zones formed during magmatic emplacement attendant to subduction from 126 to 91 Ma (Premo et al., 2014). As subduction progressed eastward from beneath thin oceanic crust to beneath thick continental crust, pluton emplacement migrated eastward. Changing subduction conditions through 35 Ma, and autochthonous batholith formation, resulted in progressively modified
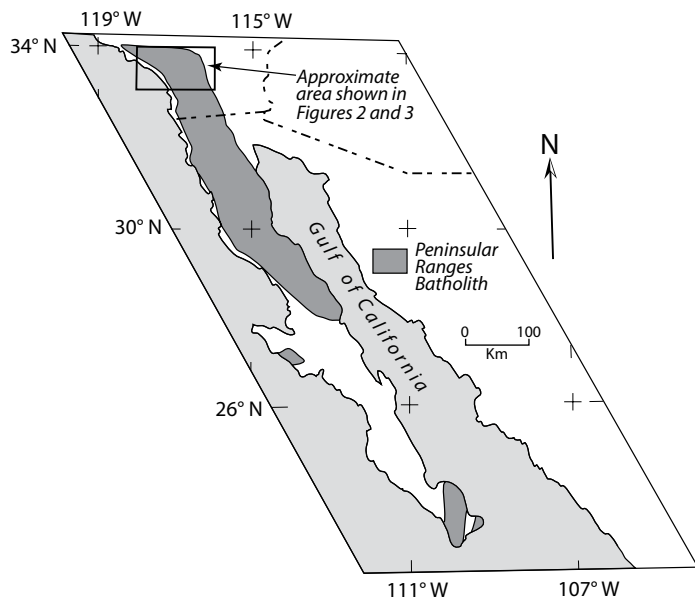
Figure 1. Index map of the Peninsular Ranges batholith outlining the northern part that contains the gem-bearing and rare-earth–bearing pegmatite districts and the area covered by Figures 2 and 3.

chemical and physical environments for pluton generation, producing a wide variety of compositions, textures, and fabrics. Circa 85 Ma allochthonous batholithic rocks occur east of the Eastern Peninsular Ranges mylonite zone (Fig. 2; Premo et al., 2014), and the batholith is structurally terminated on the east by the much younger San Andreas fault zone.

The western zone in which most of the lithium-bearing pegmatites (Li-pegmatites) are located consists of plutons that were passively emplaced during an early 126 Ma to 108 Ma extensional phase of subduction (Morton et al., 2014a; Premo et al., 2014). Most plutons emplaced during this extensional subduction phase have initial $^{87}Sr/^{86}Sr$ ratios (Sr_i) < 0.7045 and average 0.7039, reflecting their oceanic crust affinity. Western zone plutons range in composition from low-silica gabbro to high-silica granite, and their Sr_i values are notably independent of both rock composition and silica content (Lee et al., 2007; Clausen et al., 2014; Kistler et al., 2014). Gabbro bodies are large and numerous in the western zone (Fig. 2) and decrease in number and size eastward. Inverse to the eastward-diminishing size and number of gabbro bodies, Sr_i values have a moderate, but regular increase eastward (Morton et al., 2014a).

Pluton emplacement in the western zone terminated as subduction began transitioning from beneath oceanic crust to beneath continental crust, forming a western transition zone and an eastern transition zone. The emplacement environment of western transition zone plutons, from 111 to 98 Ma, radically changed from passive to extremely dynamic and forceful. Western transitional zone plutons characteristically have well-developed foliations and commonly lineations. Average initial Sr_i values increase from 0.7039 in the western zone to 0.7049 in the western transition zone (Fig. 3). Eastern transition zone plutons, also dynamically emplaced ca. 99–93 Ma, have Sr_i values ranging from 0.7050 to 0.7054, and average 0.7053. In both transition zones, Sr_i and average silica content generally increase eastward.

Further eastward, the eastern zone (98–91 Ma) originated as subduction was occurring beneath continental crust, and it formed large calcic tonalite plutons, commonly referred to as La Posta–type plutons (e.g., Tulloch and Kimbrough, 2003). Eastern zone Sr_i values range from 0.7060 to 0.7075 and average 0.7070. East of the four autochthonous batholith zones, there is an allochthonous upper-plate zone (Morton et al., 2014a).

Except for one occurrence, all known lithium pegmatites are located in the western NPRB. The exception is the pegmatites within the easternmost olivine gabbro in the NPRB (Fig. 2) at Thomas Mountain. Thomas Mountain gabbro zircons have a U/Pb age of 101.4 Ma (Kimbrough et al., 2015). Compared to Sr_i values in the western part of the NPRB, Thomas Mountain gabbro has a relatively high value of 0.7057; the Sr_i values of adjacent tonalite are equal to, or greater than, 0.7060. The first reported occurrence of lithium tourmaline in southern California (Kunz, 1905) was from Li-pegmatites in the Thomas Mountain gabbro.

Pegmatites in all the major Li-pegmatite districts occur exclusively within mafic plutonic rocks that range in composition from gabbro to mafic tonalite (e.g., Jahns, 1979; Foord, 1991). Only a few Li-pegmatites extend into prebatholithic metamorphic host rocks adjacent to gabbro/tonalite plutons. No granodiorite, monzogranite, or granite plutons in any NPRB zone have been shown to host REE- and Li-pegmatites. (Note, while Patterson [2009, p. 287] stated the Rincon district, Ramona district, and Pala Chief and Harriet Mountains in the Pala district pegmatites are hosted by granodiorite, this association is not supported by geologic maps of Rincon [Hanley, 1951], Ramona [Todd et al., 2014; Weber, 1963], and Pala [Jahns and Wright, 1951], which show the host is mafic tonalite and diorite.)

All of the mafic plutons hosting REE- and Li-pegmatites have Sr_i values that increase from west to east, reflecting the eastward-increasing component of continental crust within the batholith. Even so, Sr_i values of these mafic plutons never exceed 0.7060 (Fig. 3).

Initial Sr values of the Stewart dike, $Sr_i = 0.7042$, clearly indicate it is an I-type pegmatite (e.g., London, 2008). Based on mineralogy, the Stewart dike is a lepidolite type within the Li subclass of the miarolitic class of the LCT (Li-Cs-Ta) family (Cerny et al., 2012). The Stewart dike, however, in at least one respect differs from typical I-type pegmatites in that it contains an abundance of phosphate minerals. This abundance of phosphate mineral appears to be an anomaly, because as London (2008, p. 163) stated,

"…the S- and I-type suites are separated by one clear distinction: those that dominantly originate from S-type sources are enriched in P and contain a number of phosphate minerals other than apatite, whereas in the I-type suites, the P content of melt falls with the continued crystallization of apatite. The evolved pegmatites derived from I-type sources are very poor in P and lack the complex assemblages of phosphates, or at least their abundance."

Cerny et al. (2012, p. 291) concluded, "The main characteristics of the LCT pegmatites, however, are derived from previously unmelted, mica-rich metamorphic rocks, irrespective of the tectonic regime in which their initial partial melting occurs." The major Li-pegmatite districts are in the western part of the NPRB, where the metamorphic grade is greenschist, and where there is no evidence of anatexis.

The low Sr_i values of the Stewart pegmatite and host gabbro/tonalite, however, indicate that clearly neither are S-type. That notwithstanding, the Stewart dike contains 14 phosphate minerals, five of which are primary, including large masses of amblygonite and common lithiophilite.

Overviews of the gem-bearing pegmatites in San Diego County were provided by Weber (1963) and Foord and Shigley (1991), and production from the Pala district pegmatites was described in Jahns and Wright (1951), Jahns (1979), and Weber (1963).

PALA PEGMATITE DISTRICT

Geologic Setting

The Stewart pegmatite-aplite lies entirely within a 17 km² gabbro-tonalite pluton, originally referred to by the generic name San Marcos gabbro (Larsen, 1948). Because the San Marcos name has been applied
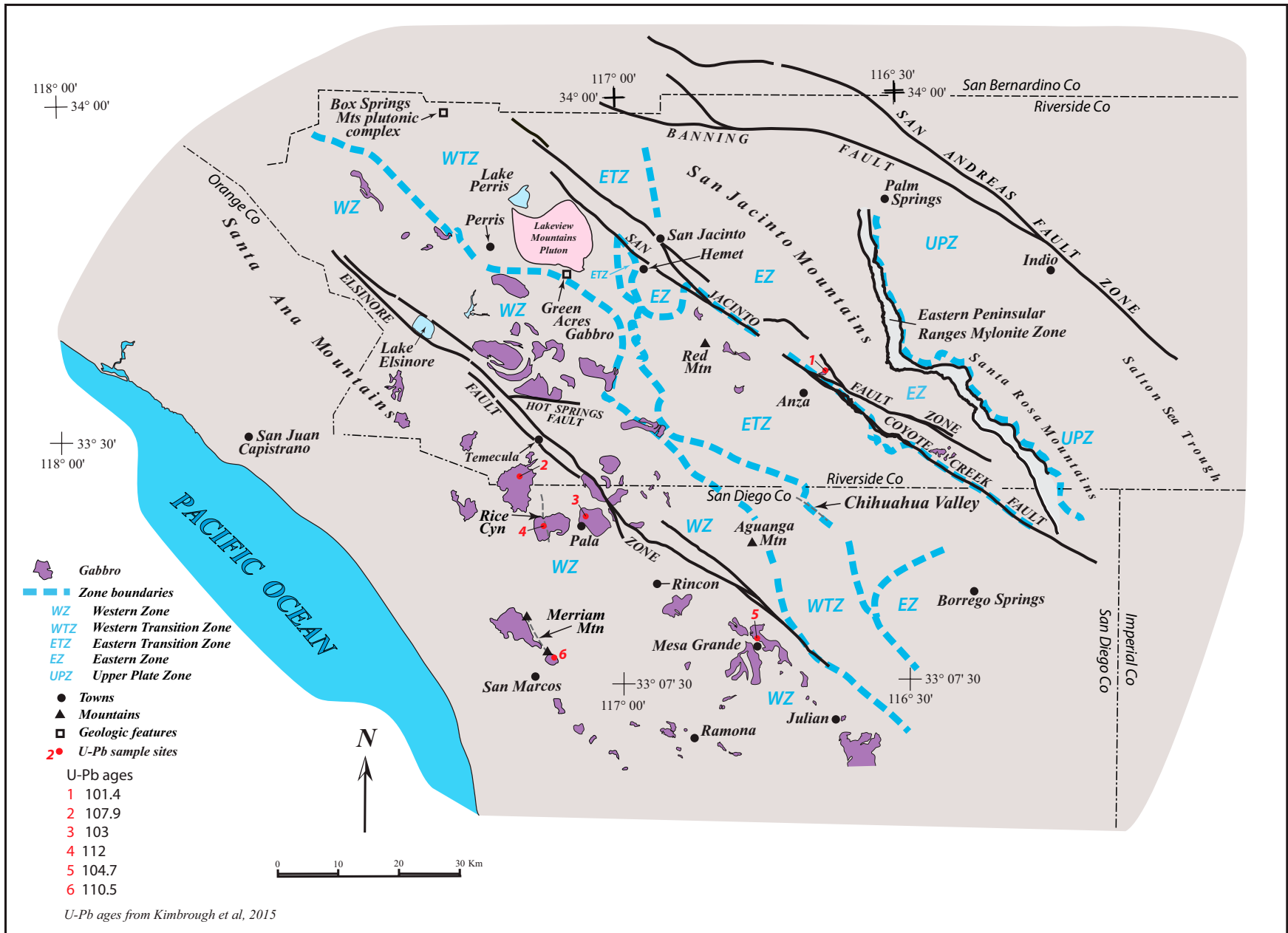
Figure 2. Northern Peninsular Ranges batholith, showing batholith zones, gabbro bodies, and U/Pb ages. Almost all of the gabbro bodies and pegmatite districts are in the western zone. Both the size and concentration of gabbro plutons decrease eastward from the western zone.

Legend:

- Gabbro
- Zone boundaries
- WZ   Western Zone
- WTZ Western Transition Zone
- ETZ Eastern Transition Zone
- EZ   Eastern Zone
- UPZ Upper Plate Zone
- ● Towns
- ▲ Mountains
- □ Geologic features
- 2● U-Pb sample sites

U-Pb ages
1 101.4
2 107.9
3 103
4 112
5 104.7
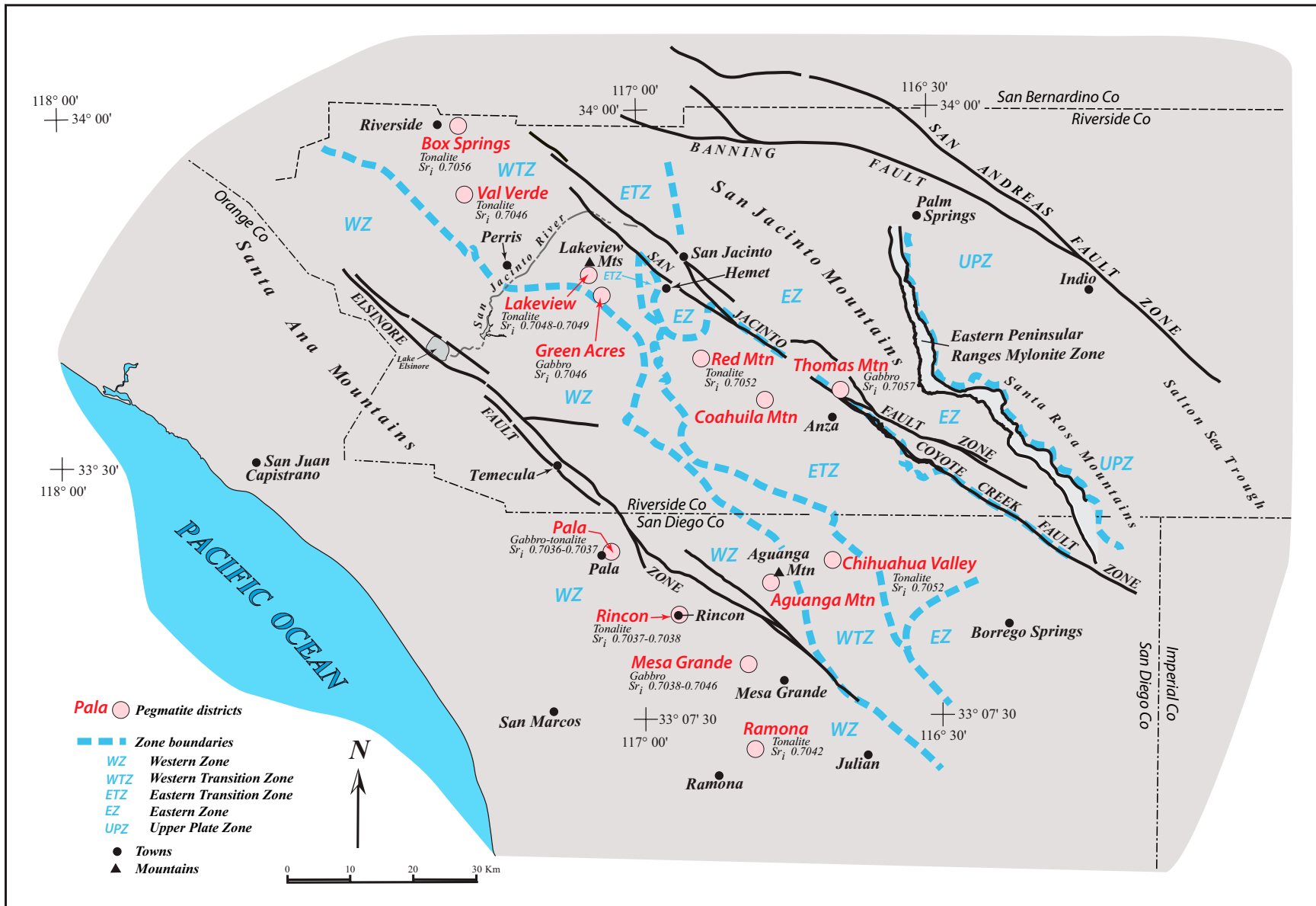6 110.5

U-Pb ages from Kimbrough et al, 2015

Figure 3. Northern Peninsular Ranges batholith showing batholith zones, pegmatite districts, and Sr_i values of various gabbro and mafic tonalite plutons. Sr_i values show a relatively systematic increase from west to east.

to most gabbroic rocks in the NPRB, many of which vary greatly in age and lithologic character, we refer to the Pala district pegmatite-aplite host rock as the Pala gabbro. The Pala gabbro is bisected by the San Luis Rey River, and all known significant Li-pegmatites are located within 7 km^2 of the pluton north of the San Luis Rey River: Only this northern part of the pluton is considered in the following discussion. The pluton is ~80% olivine and hornblende gabbro and ~20% tonalite. Zircons from olivine gabbro collected 240 m west of the Stewart pegmatite-aplite have a U/Pb age of 103 Ma (Kimbrough et al., 2015). The Sr_i of two Pala gabbro samples is 0.7037, and a third is 0.7036 (Kistler et al., 2014; R.J. Fleck, 2009, personal commun.). All batholithic rocks surrounding the Pala gabbro for a distance of at least 15 km have Sr_i values ranging between 0.7032 and 0.7042.

Host rock surrounding the northern part of the Pala gabbro consists of quartzite, quartz conglomerate, quartz mica schist, minor amphibolite and marble, and fine-grained granodiorite (Jahns and Wright, 1951). The metasedimentary rocks have been interpreted to grade into the fine-grained granodiorite (Jahns, 1948; Jahns and Wright, 1951). Beyond this zone of mixed lithology, there is a large pluton of medium-grained granodiorite, initially termed the Woodson Mountain granodiorite (Larsen, 1948) and more recently referred to as the granodiorite of Rainbow (Kennedy, 2000). Emplacement of the granodiorite pluton predated the Pala gabbro by at least 10 m.y., based on a hornblende $^{40}Ar/^{39}Ar$ age of 113 Ma for the granodiorite (Snee and Foord, 1991). The granodiorite has an isotropic texture, except within 600 m of the zone of mixed lithologies surrounding the Pala gabbro. There, the granodiorite is crudely foliated and concordant with the outer form of the Pala gabbro pluton. The Sr_i of the granodiorite is the same as that of the Pala gabbro, 0.7036.

Isotopic Age Constraints

At the time of Jahns and Wright's (1951) work, ages of pluton emplacement in the NPRB were not known. The Upper Cretaceous age then assigned to the overall batholith was largely based on relative age relationships of rock units in northern Baja California (Bose and Wittich, 1913; Woodford and Harris, 1938). The accepted sequence of pluton emplacement at that time was from lithology based on a simple conceptual model of magmatic differentiation: gabbro, tonalite, granodiorite, and granite. This emplacement sequence apparently derives from Larsen (1948), who, based on his field work, stated this succession was "commonly found in batholiths" (Larsen, 1948, p. 136).

Decades after the work of Jahns and Wright (1951), it was well established that the emplacement ages of granitic plutons of the NPRB, irrespective of lithology, systematically decrease from west to east (e.g., Armstrong and Suppe, 1973; Silver and Chappell, 1988; Ortega-Rivera, 2003; Todd et al., 2003; Premo et al., 2014). West to east, granitic pluton ages decrease from 126 to 92 Ma (Premo et al., 2014). Gabbro U/Pb ages obtained for nine gabbro bodies in the NPRB (Fig. 2) likewise decrease west to east, from 112 to 101.4 Ma (Kimbrough et al., 2015). Clearly, gabbro bodies of the NPRB are not the oldest rocks of the batholith, and there appears to be no systematic correlation between the ages of plutons and their compositions, or between compositions of plutons and their sequence of emplacement.

An $^{40}Ar/^{39}Ar$ age of muscovite from the Stewart dike was found to be 100.4 Ma (L.W. Snee, 2009, personal commun), essentially the same as the 99.4 Ma $^{40}Ar/^{39}Ar$ age of muscovite from the Pala Chief mine (Snee and Foord, 1991), 1.2 km from the Stewart mine. Considering that the 103 Ma zircon age of the Pala gabbro was established when the gabbro was at least 900 °C and Ar retention in the muscovite was ~330 °C, there is basically no difference in the age of the Pala gabbro and the Stewart dike.

Pala District Pegmatites

The Pala pegmatite district map (Jahns and Wright, 1951) shows pegmatites are essentially within the Pala gabbro, with only a few dikes extending a short distance into surrounding host lithologies. Later, Jahns (1979, p. 6) stated: "With few exceptions, the gem-bearing (pegmatites) and closely associated dikes are confined to plutons of gabbroic rocks and mafic tonalites." Regarding the gem-bearing pegmatites in San Diego County, Foord and Shigley (1991, p. 130) also stated: "With few exceptions the gem-bearing pegmatites are confined to gabbroic or tonalitic plutons, and on approaching the contacts with other rocks types, they are commonly observed to either pinch out or abruptly terminate."

Most of the larger pegmatites in the Pala district have a footwall zone consisting of aplitic to fine- and medium-grained granite (Jahns and Wright, 1951). Jahns (1979) noted that pegmatite dikes having fine-grained textured footwall rocks are so widespread that they might more accurately be termed pegmatite-aplite dikes. Taylor et al. (1979) agreed, applying the name pegmatite-aplite dikes to the Pala district pegmatite bodies. That terminology has been used by subsequent workers and is followed here. Idealized cross sections of Pala district dikes are shown in figure 25 of Jahns and Wright (1951).

In addition to the larger mapped pegmatite-aplite dikes, there are numerous small pegmatites, commonly only a few centimeters thick and only one to a few meters in length. These small pegmatites are irregular in geometry and lack the aplite-textured footwall of the larger dikes. Most of the larger dikes strike north and dip west 20° to 30°. They vary in thickness along strike, branch, and/or anastomose, commonly in a complex fashion (Jahns and Wright, 1951).

STEWART PEGMATITE-APLITE DIKE

Mining History of the Stewart Pegmatite-Aplite

The Stewart mine has a two-phase mining history: the first phase, 1882–1929, as a source of lithium, and the second phase, 1968 to the present, as a source of gem minerals. During the first phase, the Stewart mine produced lepidolite and amblygonite from the core zone of the dike, and was, for a number of years, the principal domestic source of lithium. The mine consisted of open cuts along a ridge top and a series of adits at different elevations on the west side of the ridge that penetrated the hanging wall of the dike. For safety reasons, the underground workings were backfilled and are no longer accessible. North of the Stewart mine, there are the Lepidolite Workings, Little Joe, Joe Two, North Star, Gem Star, and the North Star (Ashley) adits.

In the early lithium mining days, more than 80 of the 128 Stewart miners were Chinese. The mine owner, American Lithia and Chemical Corporation of New York, allowed off-duty Chinese to mine for pink elbaite, which was shipped to China, where it was highly valued. With enforcement of the Chinese Exclusion Act of 1882, the Chinese miners quickly covered their adit and left Pala by 1888. The Chinese adit, ~30 m north of the Stewart mine adit, was apparently forgotten by the time of Jahns and Wright's (1951) work.

In 1969, a new adit was developed 18 m north of the original Stewart mine adit to explore for gem minerals. Within 20 m, the new mine intersected the Chinese workings, where mining implements and three ore cars were found. Two of the ore cars contained dump material, and the third contained gem tourmaline, beryl, and quartz.

Current mining is above the core zone and includes enlargement of the old excavations along the ridge summit and development of a complex network of drifts and stopes from the new Stewart mine adit. Currently

(2018), the total length of new underground workings is ~5.5 km. Most of our observations, data, and interpretations are from the new underground and surface excavations, supplemented by observations and material collected in the early to mid-1950s.

GEOLOGY, MINERALOGY, AND CHEMISTRY OF THE STEWART DIKE

The exposed length of the Stewart dike is 1.1 km, splaying into three dikes in the northern 200 m. Each splay terminates at the gabbro-tonalite contact with surrounding schist and quartzite host rock. The central and northern part of the dike, located along the east side of Queen Mountain, is semitabular, consisting of a series of undulating bulges along strike. In the southern part of the dike, which is exposed along a ridge crest, the west side of the ridge is the hanging wall of the dike. The maximum thickness of the Stewart dike in the southern part is at least 56 m.

Except for the southern part, the Stewart dike strikes north and dips 20° to 35°W. In the southern part, the hanging wall in the area of the old and new Stewart Mine adits strikes N30°W and dips 25° to 35°SW. Twenty meters south of the original Stewart mine adit, the hanging-wall contact veers abruptly to a N80°W strike and a 35° south dip. The dike's southern terminus is not exposed.

Footwall and Hanging-Wall Gabbro

The Stewart dike is entirely contained within olivine and hornblende gabbro of the Pala gabbro pluton. Fabric of the gabbro is mostly isotropic, but in places, the rock is crudely layered. The composition of unaltered gabbro sampled near the Stewart dike is given in Table 1. The chondrite-normalized REE pattern of the gabbro is essentially flat (Fig. 4).

Gabbro adjacent to the dike has been altered to chloritic and clay material. The extent of alteration is more pronounced in the hanging wall than it is in the footwall. Footwall gabbro samples were collected from the contact with the dike, for a distance of 127 cm into the gabbro, normal to the contact. At a distance of 127 cm, the gabbro megascopically appears unaltered. Hanging-wall gabbro samples were collected normal to the contact for a distance of 300 cm into the gabbro. Hanging-wall gabbro even at 3 m from the contact is altered, but lack of exposure did not permit sampling beyond 3 m. The chemistry of footwall and hanging-wall gabbro is given in Table 1 and Figure 5.

Dike Zones

All descriptions of the Stewart pegmatite-aplite have enumerated a variety of textural-compositional zones within the dike. In Jahns' pegmatite classification, based on segregation of minerals within pegmatite bodies, the Stewart dike is classified as an "asymmetrically zoned pegmatite with aplitic footwall portion" (Jahns, 1982, p. 297), but on a scale of meters rather than centimeters. Jahns and Wright (1951) described the Stewart dike in the area of the Stewart mine as consisting of eight zones, three below and four above a discontinuous quartz-spodumene core zone. Later, Jahns (1979) simplified the zonation to six zones, a quartz-spodumene core zone overlain by three zones and underlain by two zones. For the pegmatite-aplite dikes in the Pala district, Jahns (1979, p. 9) stated, "Where present, the main pocket horizon or zone ordinarily is found along their footwall portions."

Shigley and Brown (1985, p. 397) described nine zones, including a quartz-spodumene core zone overlain by four upper hanging-wall zones. Below the core zone, they described a pocket zone consisting of "gem-bearing pockets and massive lepidolite ore bodies." Below the pocket zone,

they defined three zones; the lowest, a footwall zone, was described as "albite-quartz-microcline-schorl (line rock)." Later, Shigley (1991, p. 132) described the Stewart pegmatite zones as "mineral assemblages arranged in subparallel, originally sub horizontal (but now tilted) layered zones above and below a discontinuous quartz spodumene core." He described seven zones in the dike, three above and three below a core zone, and added, "Much of the lower portion of the dike, however, consists of a coarse-grained assemblage of albite-quartz-muscovite and a sugary, fine-grained albite-quartz-muscovite-schorl unit" (Shigley, 1991, p. 132–133). He described gem-bearing pockets as located "within the core zone or along its margin" and that the gem-bearing pockets "are unsystematically distributed within the enclosing pegmatite" (Shigley, 1991, p. 133).

Patterson (2009) interpreted the Stewart dike to have 22 zones formed from at least 10 pulses of pegmatite-forming fluids. In his tenth pulse, two saccharoidal aplite zones, one 3 m thick and the second 2 m thick, were formed 2.5 m above the footwall contact. Jahns and Wright (1951) and subsequent workers interpreted the lower aplitic part of the Pala district pegmatite-aplite dikes to have formed early in the dike formation.

We recognize six main compositional-textural zones in the southern part of the dike (Fig. 6). A footwall zone, composed of aplite and fine- to coarse-grained hypidiomorphic-granular granite, has an average thickness of ~3 m and transitions upward through an increase in grain size into a lower intermediate zone of coarse pegmatitic-textured schorl-muscovite-quartz-albite–K-feldspar–granite. Above the lower intermediate zone, there is a core zone, ranging from essentially lepidolite to heterogeneous assemblages of lepidolite, spodumene, petalite, amblygonite, lithiophilite, albite, and quartz. Above the lepidolite core zone, there is an upper intermediate zone of coarse pegmatitic-textured granite that is commonly layered and includes graphic granite, composed of schorl-muscovite-quartz-albite–K-feldspar granite.

Where the core zone is composed of a heterogeneous assemblage of lepidolite, spodumene, petalite, and amblygonite, a perthite zone is located between the core zone and the upper intermediate zone. The perthite zone consists essentially of giant perthite crystals in large part replaced by numerous upward-tapering autometasomatic bodies emanating from the core zone. In contact with gabbro, an ~1-m-thick hanging-wall zone, above the upper intermediate zone, is composed largely of graphic granite that is characterized by clusters of radiating muscovite crystals within coarse-grained granite.

Footwall Zone

Typical of the larger pegmatite-aplite dikes in the Pala district, the footwall zone of the Stewart dike consists of aplite and fine- to coarse-grained granite. However, unlike most other large dikes in the Pala district, the
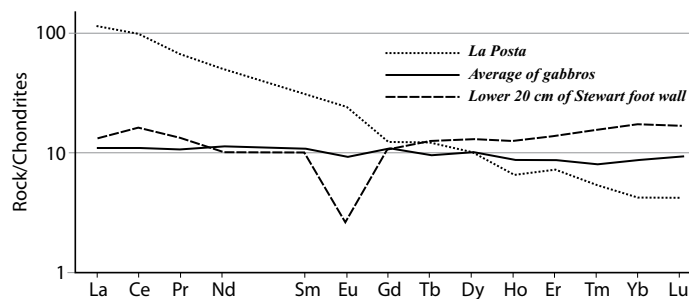

Figure 4. Chondrite-normalized rare earth element (REE) plot for the Stewart dike, Pala gabbro, and a typical La Posta–type tonalite pluton. Plot demonstrates the REE similarity between the Stewart dike and the lithologically contrasting gabbro, and the pronounced dissimilarity between the Stewart dike and the relatively silicic and alkalic La Posta pluton.

TABLE 1. GABBRO CHEMISTRY

Distance from pegmatite (cm)	Sample no.	SiO$_2$ (%)	TiO$_2$ (%)	Al$_2$O$_3$ (%)	Fe$_2$O$_3$ (%)	CaO (%)	MnO (%)	MgO (%)	Na$_2$O (%)	K$_2$O (%)	P$_2$O$_5$ (%)	LOI (%)	Sum (%)	F (ppm)	B (ppm)	Ba (ppm)	Co (ppm)	Cr (ppm)	Cs (ppm)	Li (ppm)	Rb (ppm)	Sr (ppm)	Zn (ppm)
	Unaltered gabbro																						
	PGb-1	46.5	0.82	18.3	10.90	13.2	0.17	8.57	1.15	0.10	0.02	1.29	101.02	170	30	34.9	43.2	100	4.6	90	11.9	271	29
	PGb-2	42.5	0.23	23.0	9.57	13.0	0.13	10.50	0.75	0.02	<0.1	0.22	99.92	N.A.	<0.1	7.0	55.9	130	0.3	<0.1	1.2	328	100
	PGb-3	42.9	0.05	27.3	6.51	14.8	0.10	7.46	0.70	<0.1	<0.1	0.32	100.14	N.A.	<0.1	8.4	36.3	<0.1	0.1	<0.1	0.4	396	62
	PGb-4	44.1	1.39	19.5	14.1	13.2	0.22	6.37	1.41	0.05	0.05	0.06	100.45	N.A.	<0.1	24.6	37.6	<0.1	0.2	<0.1	0.4	320	38
	PGb-5	43.2	0.03	29.1	4.90	15.2	0.09	5.89	0.74	0.01	<0.1	0.66	99.82	N.A.	N.A.	25.1	30.3	<0.1	<0.1	<0.1	0.4	423	112
	Avg.	43.8	0.50	23.4	9.20	13.9	0.14	7.76	0.95	0.04	0.04	0.51											
	Hanging-wall gabbro																						
0	HWGb-1	60.3	0.56	16.5	6.11	2.17	0.10	1.93	2.22	1.08	0.03	8.38	99.38	550	1830	163	14.7	30	28.7	160	89.8	141	151
38	HWGb-2	47.4	0.77	19.7	9.61	6.75	0.16	6.41	0.92	0.35	0.02	8.18	100.27	310	<0.1	43.8	36.3	70	9.9	270	25.3	186	84
89	HWGb-3	49.4	0.99	18.7	10.30	9.50	0.16	5.35	2.45	0.32	0.07	3.09	100.33	200	<0.1	91	29.7	40	3.1	130	12.7	354	80
117	HWGb-4	45.9	1.16	19.3	11.70	11.4	0.18	6.63	1.49	0.14	0.05	2.48	100.43	220	<0.1	19.4	35.8	60	2.5	110	5.5	385	90
211	HWGb-5	47.2	1.14	19.0	11.10	10.4	0.15	6.71	1.26	0.13	0.05	3.77	100.91	140	<0.1	9.4	36.2	60	1.8	120	5.2	333	86
300	HWGb-6	46.8	1.14	19.1	11.80	11.2	0.20	6.39	1.77	0.14	0.11	2.41	100.06	280	<0.1	13.9	31.3	90	1.4	80	5.7	397	101
	Avg.	49.5	0.96	18.7	9.94	8.57	0.16	5.57	1.69	0.36	0.06	4.72											
	Footwall gabbro																						
0	FWGb-0	51.4	0.71	18.6	7.77	2.50	0.14	4.03	0.49	1.11	<0.1	14.0	100.75	600	20	450	24.0	90	33.0	130	90.5	180	65
25	FWGb-1	49	0.71	17.5	9.80	3.84	0.20	5.74	0.45	0.16	0.01	13.1	100.51	380	20	81.4	32.1	110	33.2	130	10.0	242	92
51	FWGb-2	48.1	0.72	18.5	9.68	7.15	0.20	6.83	0.87	0.23	0.02	8.28	100.58	270	<0.1	94.8	32.9	110	40.5	150	16.0	249	90
76	FWGb-3	46.8	0.60	21.9	7.98	7.43	0.15	5.39	0.97	0.13	0.02	9.00	100.37	270	<0.1	42.3	32.7	100	31.6	140	10.3	186	64
102	FWGb-4	48.1	0.64	20.3	8.44	7.01	0.13	4.88	0.97	0.35	0.03	10.4	100.25	220	<0.1	99.1	28.6	100	116	120	21.2	157	68
127	FWGb-5	47.7	0.64	19.7	9.58	13.5	0.16	7.71	1.33	0.06	0.03	0.77	100.17	100	<0.1	46.6	33.6	130	4.7	50	1.7	324	86
	Avg.	48.5	0.67	19.4	8.88	6.91	0.16	5.76	0.85	0.34	0.02	9.26											
	Average unaltered gabbro	43.8	0.50	23.4	9.20	13.9	0.14	7.76	0.95	0.04	0.04	0.51											
	Average hanging-wall gabbro	49.5	0.96	18.7	9.94	8.57	0.16	5.57	1.69	0.36	0.06	4.72											
	Difference	**+5.7**	**+0.46**	**−4.7**	**+0.74**	**−5.33**	**+0.02**	**−2.19**	**+0.74**	**+0.32**	**+0.02**	**+4.21**											
	Average unaltered gabbro	43.8	0.50	23.4	9.20	13.9	0.14	7.76	0.95	0.04	0.04	0.51											
	Average footwall gabbro	48.5	0.67	19.4	8.88	6.91	0.16	5.76	0.85	0.34	0.02	9.26											
	Difference	**+4.7**	**+0.17**	**−4.0**	**−0.32**	**−6.99**	**+0.02**	**−2.00**	**−0.10**	**+0.30**	**−0.02**	**+8.75**											
	Average hanging-wall gabbro	49.5	0.96	18.7	9.94	8.57	0.16	5.57	1.69	0.36	0.06	4.72											
	Average footwall gabbro	48.5	0.67	19.4	8.88	6.91	0.16	5.76	0.85	0.34	0.02	9.26											
	Difference	**−1.0**	**−0.29**	**+0.7**	**−1.06**	**−1.66**	**0.00**	**+0.19**	**−0.84**	**−0.02**	**−0.04**	**+4.54**											

Note: Includes unaltered gabbro collected well away from the Stewart dike, and altered gabbro adjacent to the hanging wall and footwall. See also Figure 5 for graphical representation of alteration adjacent to the dike. LOI—loss on ignition.
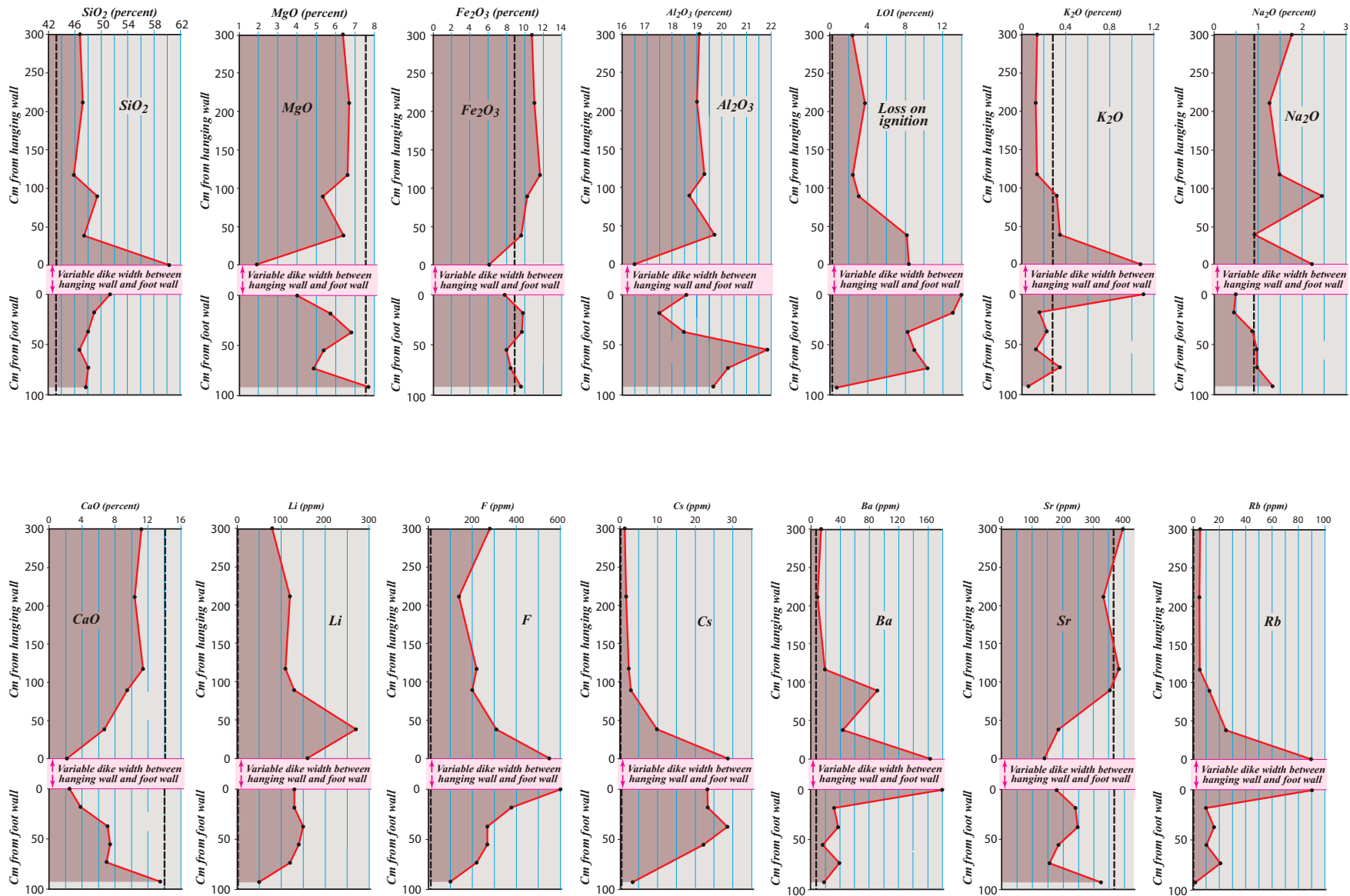
Black heavy-dashed lines represent the average of 4 gabbro analyses collected more than 10 m from the Stewert Pegmatite

Figure 5. Plots showing chemical variation in the footwall and hanging-wall gabbro. Alteration effects on the gabbro near the dike are noticeable in both the footwall and hanging-wall gabbro, but overall, they are more pronounced in the hanging wall, particularly for SiO₂, Na₂O, and Li. Lines connecting analyses are a visual aid for comparisons between elements and do not imply that analyses fall on the lines. LOI—loss on ignition.
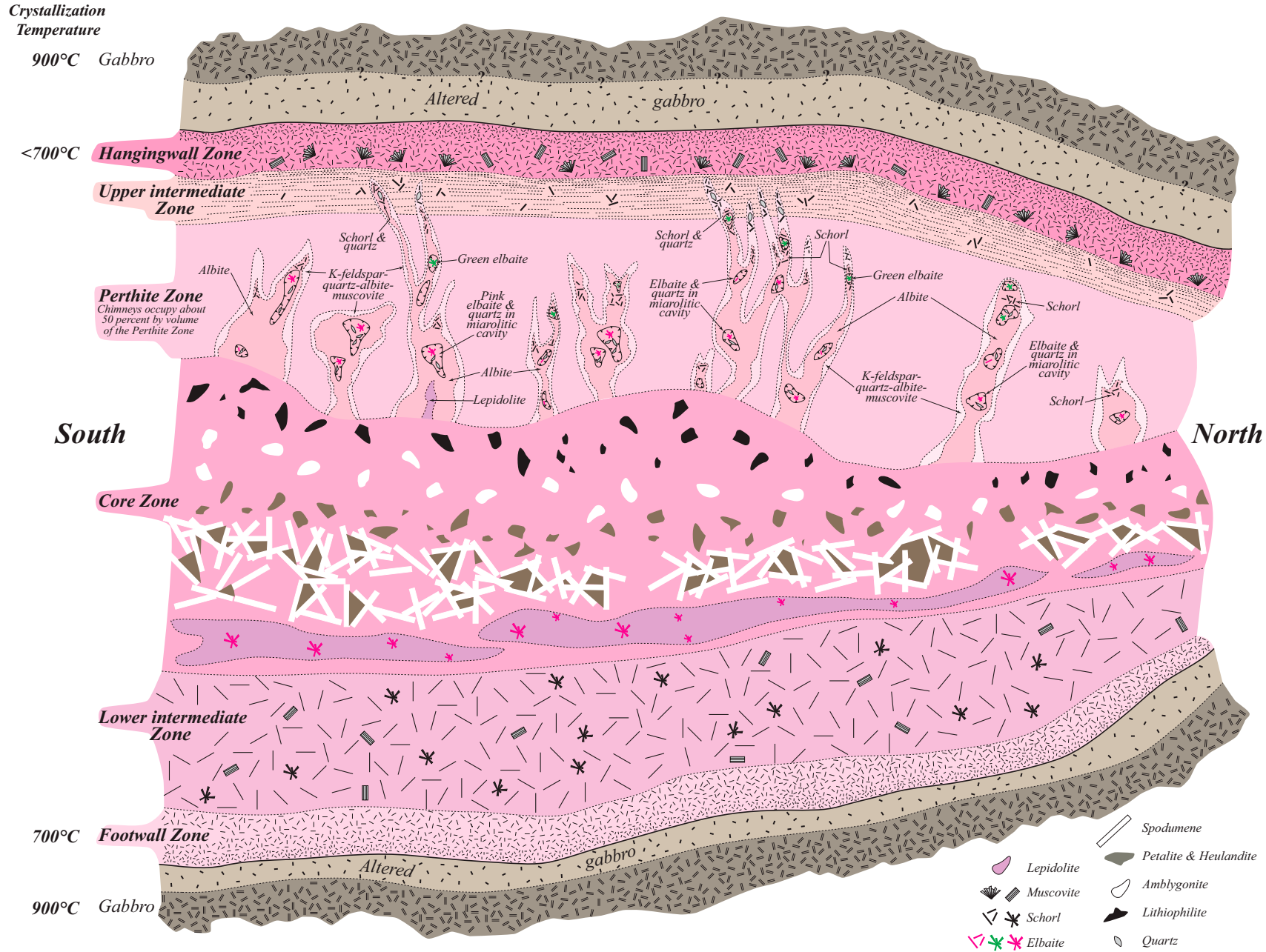
Figure 6. Longitudinal cross section through the southern part of the Stewart pegmatite where the complex core zone is well developed and well exposed. Cross section is roughly parallel to the dike, not across the dike. Downdip thicknesses of individual zones vary. The entire perthite zone and the upper part of the core zone pinch to zero thickness in places, putting the massive lepidolite bodies directly against the upper intermediate zone. Depiction of zone compositions and thicknesses is diagrammatic, but it is as representative as possible of both those properties. Chimneys make up ~50% by volume of the perthite zone in this part of the dike.

footwall zone lacks pronounced mineralogic layering, termed "line rock" (e.g., Jahns and Wright, 1951). The basal part of the footwall zone consists of K-feldspar–albite-quartz aplite that grades upward, away from the contact, into fine- to coarse-grained isotropic-textured granite. Tourmaline and muscovite are absent in the basal part of the zone, but the intermediate and upper parts include 1 cm schorl prisms and muscovite. Schorl-rich layers occur but are rare in the upper part of the footwall (Fig. 7), and locally the coarse-grained granite is foliated or protoclastic (Fig. 8). The Sr_i of the lower part of the footwall zone is 0.7042 (R.J. Fleck, 2009, personal commun.).

From the gabbro contact, the footwall zone was sampled, normal to the dip of the dike, for 340 cm into the dike (Table 2), at which point the texture of the rock transitions from coarse-grained granite into pegmatitic-textured granite. Samples 1–8 were collected in 5 cm segments

at 30 cm intervals in the aplite and fine- to medium-grained granite, and samples 9–12 were collected in 10 cm segments at 30 cm intervals in the medium- and coarse-grained granite (Table 2). Overall, the composition of the footwall zone varies somewhat systematically, but it shows erratic variations within the overall trends (Fig. 9). High values of MgO and CaO in the basal part of the footwall zone probably reflect chemical interchange with the gabbro. Boron variation clearly reflects the lack of tourmaline in the lower part of the zone and the progressively increasing amount of tourmaline in the upper part. The most pronounced chemical change through the footwall zone is barium content, which decreases from 1380 ppm at the gabbro contact to 17 ppm only 90 cm above the contact.

Chondrite-normalized REE patterns from the basal 15 cm of the dike are essentially flat, with the exception of Eu (Fig. 4).
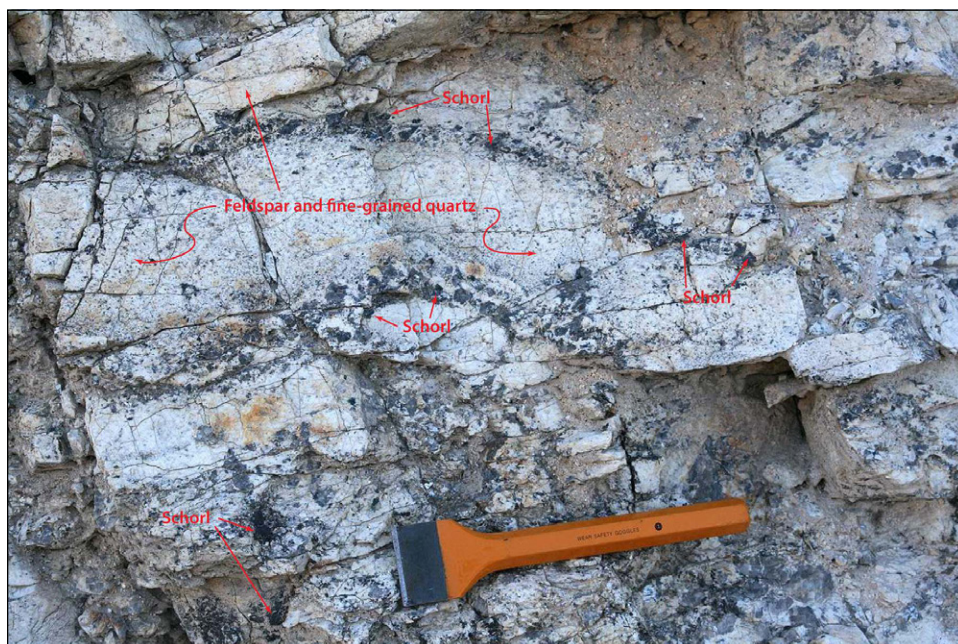

Figure 7. Schorl-rich layers in the upper part of the footwall zone. Tool is ~23 cm long.


Figure 8. Protoclastic-textured upper part of the footwall zone. Rock is well layered, and constituent minerals are disaggregated.

TABLE 2. FOOTWALL ZONE CHEMISTRY

Sample no.	Distance from gabbro (cm)	SiO$_2$ (%)	TiO$_2$ (%)	Al$_2$O$_3$ (%)	Fe$_2$O$_3$ (%)	MgO (%)	MnO (%)	CaO (%)	Na$_2$O (%)	K$_2$O (%)	P$_2$O$_5$ (%)	LOI (%)	Sum (%)	F (ppm)	B (ppm)	Ba (ppm)	Cs (ppm)	Li (ppm)	Ga (ppm)	Ge (ppm)	Rb (ppm)	Sr (ppm)	Y (ppm)	Zn (ppm)	Zr (ppm)
FW-0	0	75.2	0.01	13.9	0.25	0.40	0.03	1.20	4.68	1.32	0.03	1.91	100.84	300	40	1380	16.3	100	13	1	31.0	140	35.1	8	63.1
FW-1	30	78.6	0.01	12.9	0.17	0.19	<0.01	1.26	5.22	0.79	0.04	0.93	101.3	110	20	431	8.50	80	11	1	13.6	110	18.9	<5	114
FW-2	60	75.3	0.02	14.5	0.93	0.42	0.03	0.62	4.19	2.19	0.06	2.00	102.26	300	50	35.1	15.1	170	18	2	66.0	26.9	32.0	22	28.2
FW-3	90	73.8	0.02	15.8	1.00	0.09	0.43	0.52	5.30	2.20	0.08	0.93	101.10	130	20	16.7	2.0	140	25	3	63.2	10.3	63.2	12	78.7
FW-4	120	76.3	0.02	14.6	0.39	0.07	0.13	0.53	6.00	1.24	0.05	0.70	100.73	110	10	11.8	1.4	100	20	3	42.5	7.0	17.8	8	29.5
FW-5	150	71.2	0.01	17.1	0.73	0.10	0.31	0.38	7.05	1.72	0.07	0.78	100.23	460	500	20.3	21.7	220	24	4	107	8.3	22.1	22	21.2
FW-6	180	70.9	0.01	15.9	2.84	0.13	2.11	0.30	5.82	1.24	0.07	0.43	100.18	620	500	7.4	23.3	260	26	6	80.7	6.4	34.3	253	58.7
FW-7	210	74.3	0.01	14.9	0.97	0.09	0.56	0.17	6.11	1.99	0.07	0.30	99.77	200	600	7.0	26.7	120	20	4	140	4.8	3.4	136	17.6
FW-8	245	70.6	0.01	17.7	1.03	0.09	0.62	0.20	8.52	0.54	0.10	0.94	101.28	440	1080	147	26.5	220	25	6	76.9	9.1	5.0	134	9.3
FW-9	275	70.4	0.01	17.9	0.95	0.06	0.73	0.07	8.58	0.64	0.11	0.81	101.06	690	1320	65.9	71.1	330	29	7	133	7.2	3.4	69	19.1
FW-10	305	71.0	0.01	17.6	0.59	0.07	0.41	0.06	8.53	0.77	0.10	0.81	100.75	550	1180	14.0	84.1	280	29	6	161	4.5	2.3	53	32.3
FW-11	340	70.7	0.01	16.9	0.48	0.06	0.28	0.06	8.52	0.49	0.10	0.64	99.97	600	1290	10.3	68.7	330	26	6	102	1.4	2.2	58	20.3
Avg.		73.2	0.01	15.8	0.86	0.15	0.51	0.45	6.54	1.26	0.07	0.93		376	551	178.9	31.0	196	22	4	84.7	28.0	20.0	70	41.0

Note: Footwall samples were taken where the core zone is lepidolite. Note the systematic increase in boron relative to height above gabbro-pegmatite contact. See also Figure 9 for graphical representation of footwall chemistry. LOI—loss on ignition.
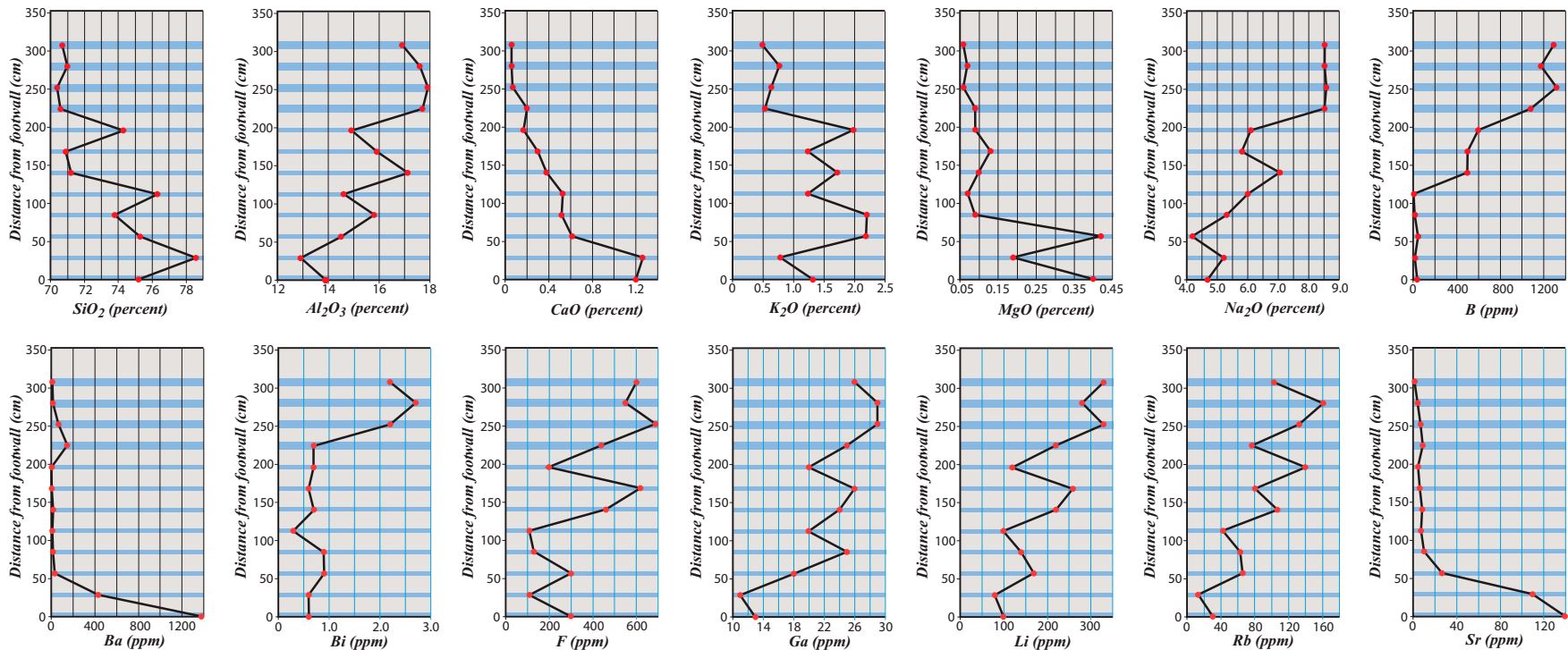
Thicknesses of blue horizontal bars represent the 5 cm or 10 cm sampling interval at each sample site.

Figure 9. Chemical variation in the footwall zone. Overall trends, but especially those of SiO$_2$, Al$_2$O$_3$, CaO, MgO, Na$_2$O, Li, and Sr suggest chemical interchange between the host gabbro and the lower part of the footwall zone. Lines connecting analyses are a visual aid for comparisons between elements and do not imply that analyses fall on the lines.

Lower Intermediate Zone

Above the footwall zone, the lower intermediate zone is normal pegmatitic-textured schorl-muscovite-perthite-albite granite. This zone was termed "undivided pegmatite" by Jahns and Wright (1951), and later termed coarse albite-quartz-perthite-muscovite pegmatite (Jahns, 1979). The thickness of the zone varies from 2 to 4.5 m. Schorl crystals, 15–40 cm in length, commonly occur in radiating clusters, in which the thickness of the individual crystals increases from the cluster core to their outer terminus. Locally, 15–30 cm intervals of the lower intermediate zone have been protoclastically deformed.

Core Zone

The lower intermediate zone grades upward into the core zone through a discontinuous quartz-rich layer of tourmaline-albite-quartz pegmatite or a mixture of intermediate zone pegmatite and lenticular masses of lepidolite. The quartz-rich layer appears to have been better developed in the old workings than in currently available exposures. The core zone, typically 3–8 m thick, is extremely variable in mineralogy along strike, ranging from lepidolite and minor elbaite, albite, and quartz to a complex heterogeneous assemblage of lepidolite, spodumene, petalite, amblygonite, and lithiophilite.

The core zone at the north end of the Stewart mine open cuts, ~120 m from the southern end of the dike, is largely lepidolite and has a 2 m transition into the lower intermediate zone. The 2 m transition there consists of fine- to medium-grained, quartz-rich pegmatite containing disseminated fine-grained, light-colored lepidolite and meter-size, lens-shaped masses of schorl-muscovite–K-feldspar–quartz pegmatite characteristic of the lower intermediate zone. Included in this transition are 3–15 cm ovoid to irregular-shaped lepidolite aggregates, commonly containing abundant minute pink elbaite prisms. Overlying this heterogeneous transition, lithology is 2–4 m of homogeneous fine- to coarse-grained isotropic lepidolite.

Analyses of samples collected over a 3 m interval from the base of the 2 m transition into the base of the lepidolite core are shown in Table 3. Overlying the lepidolite, there is ~1 m of quartz and perthite separating the core zone from the upper intermediate zone. Twenty meters south along strike, the perthite-quartz thickness increases to 4–6 m.

One hundred meters downdip from the open cut, the core zone is a 4- to 8-m-thick complex of lithium and boron mineral segregations. Textures are extremely variable, ranging from isotropic to flow-textured to foliated, and (or) protoclastic.

The heterogeneous core zone consists of, from base to top, lepidolite containing elbaite overlain by altered spodumene, which in turn is overlain by petalite and heulandite. Quartz-rich pegmatite, commonly containing large masses of amblygonite, overlies the petalite-heulandite.

The uppermost core zone is not exposed, but in the old Stewart mine, caving above lepidolite and amblygonite mined areas exposed abundant lithiophilite crystals in the uppermost core zone. Figure 6 is a longitudinal, diagrammatic cross section of the dike that, in part, illustrates the heterogeneity of the core zone.

Core zone texture and structure. The texture is isotropic where the core zone is essentially fine- to coarse-grained lepidolite that contains minor elbaite and cleavelandite. Where the core zone consists of lepidolite-spodumene-petalite-amblygonite, most textures are isotropic, and grain size ranges from aplitic and fine-grained to meter-sized crystals (Fig. 10). Locally, 1- to 35-cm-thick, discontinuous, fine-grained, flow-textured rock is defined by well-aligned albite crystals and lenses of protoclastic quartz and lepidolite (Figs. 11A and 11B). Some flow-textured rock grades into albite-lepidolite and lepidolite schistose-textured rock.

At places, in the outer parts of the core zone, 5- to 15-cm-thick pods of muscovite-albite-quartz and albite-quartz-schorl rock have a pronounced protoclastic texture (Fig. 12). Within isotropic-textured pegmatite, some albite-rich rock is deformed over a thin zone (e.g., 5 cm) grading from planar aligned albite and progressing into deformed to protoclastic-textured albite.

Faults, common within the dike, noticeably are more concentrated adjacent to, and within, a lepidolite-spodumene-petalite-amblygonite core. The faults are planar and shallow-dipping features (Fig. 13). Separation across faults ranges from a few centimeters to 25 cm. Similar small-scale faulting was not observed in the host gabbro, so it is considered to be related to processes restricted to the dike itself.

Common minerals of the core zone. There are several minerals that commonly occur in the core zone. These include albite, lepidolite, tourmaline, spodumene, petalite, amblygonite, lithiophilite, and hypogene clay.

Albite. Albite occurs throughout the core zone and ranges from aplitic textured to typical medium-grained cleavelandite. Aplitic-textured albite is white; cleavelandite is white or bluish-green (Fig. 10). Texture is mostly isotropic, but locally flow-textured, protoclastic, or schistose with interleaved foliated lepidolite (Figs. 11A and 11B). Bluish-green cleavelandite is relatively high in Cs, Ga, Li, Rb, and Sr (Table 4).

Lepidolite. Fine- to medium-grained lepidolite either constitutes the entire core zone or it is abundant in the lower part of a lepidolite-spodumene-petalite-amblygonite-lithiophilite core zone. Lepidolite occurs as lenses or layers and less commonly as rounded masses. Some lepidolite masses are essentially monomineralic, while others have minuscule to large amounts of elbaite and/or albite and quartz. Most lepidolite is light to dark violet, and less commonly very light-rose or silvery-white greasy-feeling masses. Silvery lepidolite is mostly devoid of albite and rubellite, which otherwise commonly accompany core zone lepidolite. In the

TABLE 3. WHOLE-ROCK ANALYSES OF 10 SAMPLES FROM THE LOWER PART OF THE LEPIDOLITE CORE ZONE

Sample no.	SiO_2 (%)	Al_2O_3 (%)	Fe_2O_3 (%)	B_2O_3 (%)	MgO (%)	MnO (%)	CaO (%)	Na_2O (%)	K_2O (%)	Li_2O (%)	P_2O_5 (%)	F (%)	LOI (%)	Sum (%)	Ba (ppm)	Be (ppm)	Ga (ppm)	Nb (ppm)	Rb (ppm)	Sn (ppm)	Sr (ppm)	Ta (ppm)	Tl (ppm)	Zn (ppm)
B-1	65.5	19.6	<0.01	0.09	0.05	0.45	0.19	4.26	4.37	1.72	0.21	2.33	2.10	100.87	19.3	74	75	91	5080	72	9.1	60.3	26.1	85
B-2	66.9	19.0	0.06	0.25	0.03	0.65	0.22	3.29	4.52	1.82	0.21	2.40	2.32	101.67	21.4	195	78	77	5110	102	12.0	49.9	25.4	340
B-3	66.0	19.5	0.04	0.18	0.03	0.53	0.24	3.86	4.48	1.78	0.23	2.42	2.18	101.47	21.9	133	78	77	5210	72	10.8	53.	26.6	201
I-1	67.1	16.9	<0.01	0.16	0.02	0.20	0.17	0.34	6.19	3.29	0.41	4.09	2.61	101.48	17.6	237	60	154	9370	30	34.4	96.7	62.2	5
I-2	66.8	17.6	<0.01	0.29	0.03	0.20	0.18	1.15	5.88	3.16	0.25	3.76	2.33	101.63	21.1	135	62	151	8840	30	22.3	113	58.8	5
I-3	66.8	17.5	<0.01	0.21	0.04	0.18	0.20	1.91	5.33	2.86	0.26	3.33	2.24	100.86	17.2	250	58	99	8000	28	18.6	84.3	52.1	<5
U-1	53.6	26.5	<0.01	2.10	0.04	0.51	0.10	0.47	6.62	3.83	0.05	4.14	3.86	101.82	15.4	243	126	98	9960	42	9.1	38.6	60.8	12
U-2	51.6	28.1	<0.01	2.91	0.02	0.58	0.09	0.62	6.37	3.77	0.02	4.23	3.71	102.02	16.5	236	134	95	9590	41	7.7	43.2	60.6	7
LC-1	50.2	28.9	<0.01	2.85	0.02	0.59	0.08	0.61	6.73	4.11	0.02	4.35	3.99	102.45	16.2	19	141	99	>10000	43	7.4	38.2	63.1	11
LC-2	51.4	28.0	<0.01	2.56	<0.01	0.53	0.06	0.52	6.91	4.03	0.01	4.42	3.80	102.24	16.0	20	138	103	>10000	45	7.5	34.7	64.6	9

Note: Samples were taken at close, but irregular, intervals in the lower part of the core zone beginning about 1 m above the contact with the lower intermediate zone, and continuing upward into the central part of the massive lepidolite bodies in the lower core zone. Irregular spacing of samples was dictated by availability of exposures. B samples in the table are from the basal part of the total sampled interval; I samples are from the intermediate part; U samples are from the upper part; and LC samples are from the core of the massive lepidolite bodies. LOI—loss on ignition.
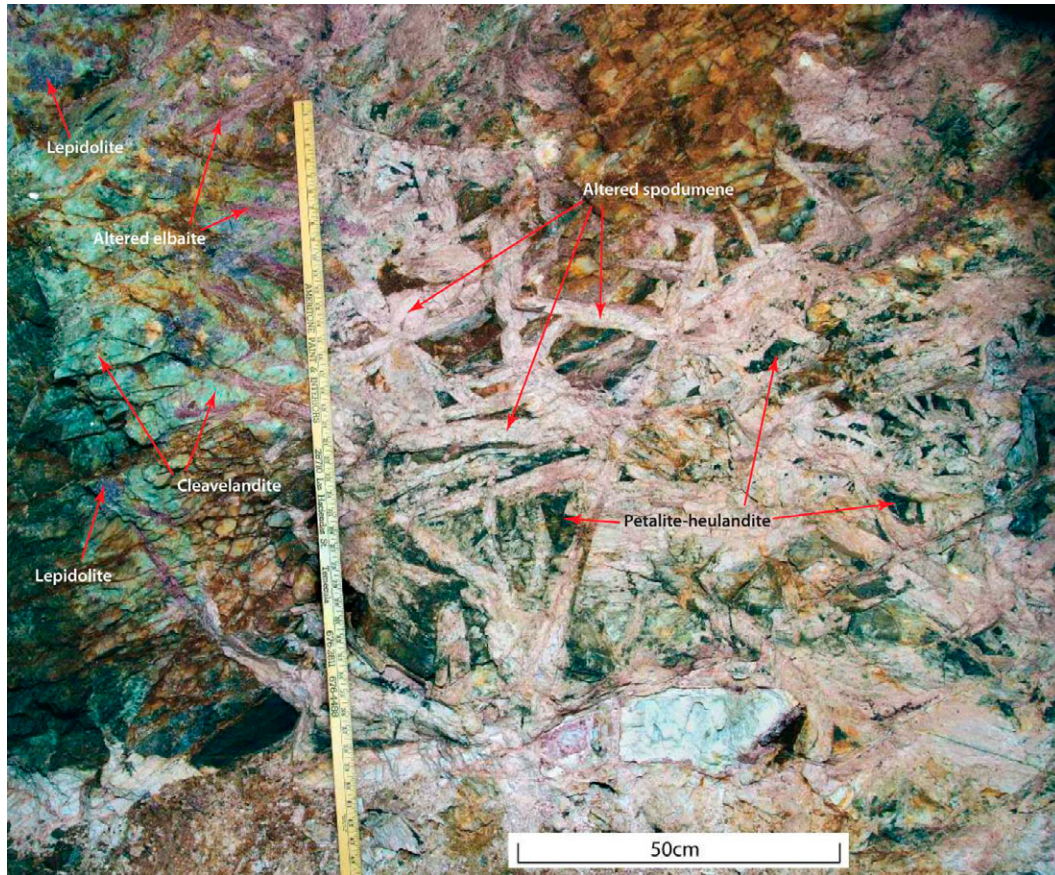
Figure 10. Central part of complex core zone. To the right of the yard stick, 20–40-cm-long altered spodumene crystals are interlaced. Dark gray to black petalite-heulandite fills interstices between the spodumene. To the left of the yard stick, the rock is made up of dark pink altered elbaite, green cleavelandite, and purplish-blue lepidolite.
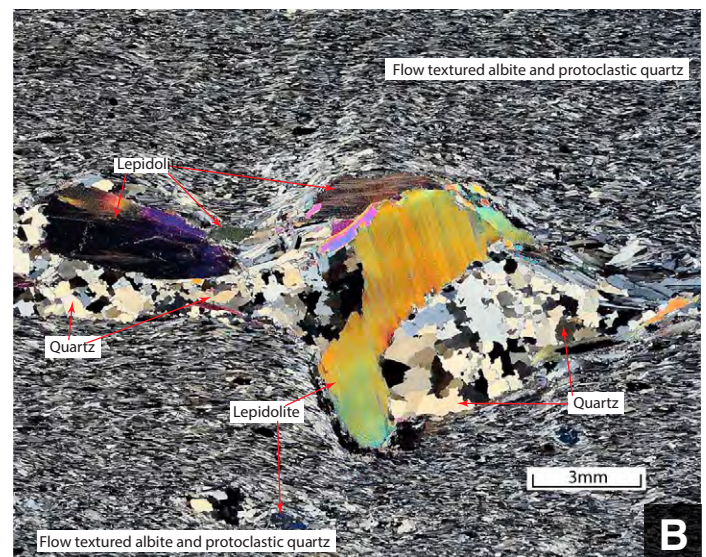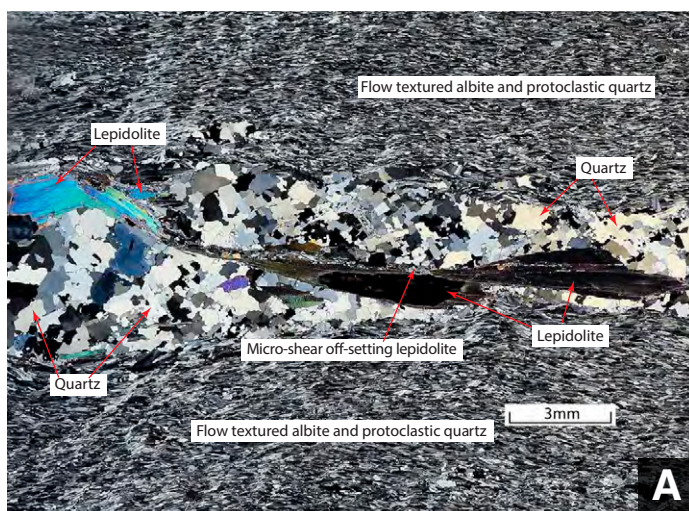

Figure 11. (A) Photomicrograph of flow-textured albite and protoclastic quartz and lepidolite from the core zone. Cross nicols. Offset black mineral is lepidolite at full extinction. Microshear offsetting the lepidolite extends to the left through birefringent lepidolite and above it through microfractured quartz. (B) Photomicrograph of flow-textured albite and protoclastic quartz and lepidolite from the core zone. Cross nicols. Relatively coarse-grained quartz and lepidolite are structurally shaped by flowage and protoclasis.
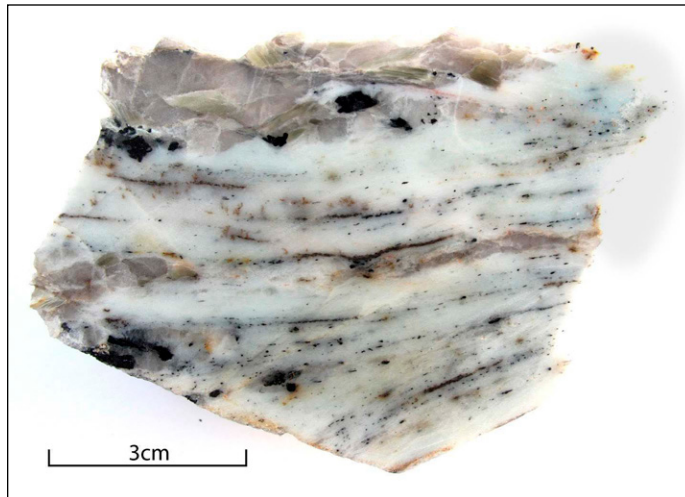
Figure 12. Slabbed face of protoclastic schorl-muscovite-quartz-albite rock from the upper part of the core zone.

3cm

Figure 13. Low-angle fault off-setting montmorillonitic clay and lepidolite ~10 cm in the lower part of a chimney in the perthite zone. Note two other shorter, roughly parallel faults just above main fault.

20 cm

TABLE 4. ALBITE CHEMISTRY

		SiO$_2$ (%)	Al$_2$O$_3$ (%)	Fe$_2$O$_3$ (%)	MgO (%)	CaO (%)	Na$_2$O (%)	K$_2$O (%)	P$_2$O$_5$ (%)	LOI (%)	Sum (%)	B (ppm)	Ba (ppm)	Cs (ppm)	Ga (ppm)	Li (ppm)	Rb (ppm)	Sr (ppm)
Core zone		67.6	20.5	<0.01	<0.01	0.10	11.3	0.24	0.17	0.61	100.52	80	2.7	50.9	34	510	196	11.0
		66.5	20.0	0.01	<0.01	0.11	11.3	0.13	0.16	0.50	98.71	60	2.7	15.2	31	120	36.7	18.9
		68.4	20.3	0.02	<0.01	0.16	11.5	0.12	0.20	0.56	101.26	60	2.6	4.8	36	100	14.9	10.8
		67.1	20.5	0.02	0.03	0.14	11.0	0.33	0.20	0.78	101.10	80	3.3	95.8	35	770	311	44.8
		68.8	19.9	0.01	0.03	0.15	10.9	0.16	0.17	0.87	100.99	70	2.4	44.6	33	240	58.3	59.1
Chimney 1	Terminus	67.6	19.2	<0.01	0.07	0.16	11.2	0.19	0.16	0.48	99.06	60	2.3	14.4	27	70	36.5	11.5
		67.9	20.8	0.01	0.11	0.18	11.3	0.19	0.16	0.71	101.36	50	3.8	9.2	27	50	21.9	8.4
		68.3	20.3	0.03	0.09	0.16	11.5	0.16	0.16	0.66	101.36	50	2.0	5.8	27	40	16.8	8.7
		67.7	20.3	<0.01	0.07	0.16	11.5	0.18	0.17	0.52	100.60	20	1.2	3.3	25	30	13.0	3.7
		68.4	20.3	0.01	0.07	0.10	11.4	0.12	0.13	0.44	100.97	40	2.1	2.2	26	50	9.9	6.7
		67.8	20.6	0.01	0.07	0.09	11.3	0.13	0.14	0.63	100.77	40	3.7	1.2	23	60	7.9	11.0
	Base	68.2	20.5	<0.01	0.04	0.07	11.2	0.52	0.11	0.56	101.20	20	1.9	2.5	25	70	76.7	6.8
Average	Core zone	67.7	20.2	—	—	0.13	11.2	0.20	0.18	0.66		70	2.7	44.1	34	348	123	28.9
	Chimney 1	68.0	20.3	—	0.07	0.13	11.3	0.21	0.15	0.57		40	2.4	5.5	26	53	26.1	8.1

Note: For comparison, includes albite from core zone and from chimneys. See also Figure 26 for graphical representation of three elements of albite from chimney 1. LOI—loss on ignition.

Figure 14. Typical occurrence of lepidolite and elbaite in the lower core zone. Lepidolite here does not show the more typical lavender coloration found in coarser-grained lepidolite in much of the Stewart dike (see Figs. 15 and 40 for comparison).
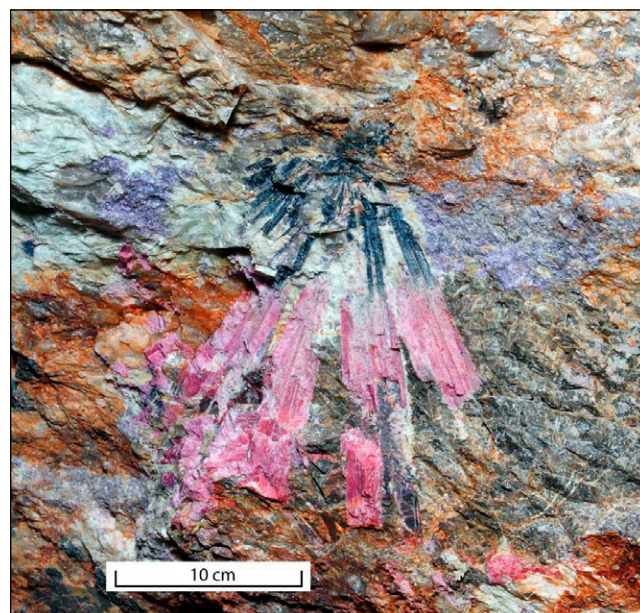

Figure 15. Radial spray of color-zoned elbaite from the core zone. Black base of each ray grades into gray, grayish pink, and then dark pink at the terminal ends. Clots of lavender lepidolite flank both sides of the base.

old workings, lepidolite lenses up to 6 m thick were reported (Jahns and Wright, 1951). Elbaite, mostly pink, occurs as small scattered individual prismatic crystals (Fig. 14) and as spherical radiating crystal groups. Some lepidolite contains both single pink elbaite and black tourmaline prisms 0.6–1.2 cm wide by 8 to 10 cm long enclosed in light blue-green, 0.6–1.2 cm cleavelandite rims. Some of the black tourmaline has a 2.4 mm rim of pink elbaite. The sequence of crystallization is black tourmaline, pink elbaite, albite, lepidolite. Analysis of lepidolite is given in Table 5.

Tourmaline. In addition to the small elbaite crystals intergrown with lepidolite, large elbaite crystals occur as single crystals and as radiating sprays. Tourmaline is semitransparent to opaque, both as uniform-colored crystals and longitudinally and (or) concentrically color-zoned (watermelon) crystals. Longitudinally color-zoned (versicolor) crystals have a black base and transition through gray to grayish-pink, and then to pink or red in the termination (Fig. 15). Four longitudinally color-zoned crystals, 10, 18, 30.5, and 53 cm long, were sampled for chemical analysis. Several elements vary systematically from base to terminus, with Fe and Zn

showing the greatest changes. Iron decreases nonlinearly from the base, ranging from several percent to a few hundredths of a percent. Mn and Zn increase from the base to medial part of the crystal and then decrease toward the terminal end. The amount of Zn from the medial parts of the crystal to the terminus decreases from 12,400–12,800 ppm to 12–69 ppm. Al, Li, and Ga increase from slight to moderate amounts from the base to the terminus. Lithium content doubles from the base to terminus in some crystals, and in one, it increases sixfold. Longitudinal color-zoned tourmaline chemistry is given in Table 6 and Figure 16.

The chemical composition of schorl in the upper part of the core zone differs from schorl in the overlying perthite zone (Table 7). Of the major elements, Fe is notably lower, and Mn is notably higher in the core zone schorl than it is in the lower perthite zone schorl. Several minor elements have significant changes, especially Zn and Li, both showing higher values in the core zone schorl (Fig. 17).

Most tourmaline from the Stewart dike has relatively high levels of Zn. Tourmaline samples from other Pala pegmatites and other pegmatite districts

TABLE 5. LEPIDOLITE CHEMISTRY

Sample no.	SiO$_2$ (%)	Al$_2$O$_3$ (%)	TiO$_2$ (%)	Fe$_2$O$_3$ (%)	MnO (%)	MgO (%)	CaO (%)	Li$_2$O (%)	Na$_2$O (%)	K$_2$O (%)	Rb$_2$O (%)	Cs$_2$O (%)	F (%)	LOI (%)	Sum (%)
L-1	50.8	25.7	<0.01	0.03	0.13	0.06	<0.01	5.30	0.25	10.4	1.68	0.20	7.00	3.22	104.77
L-2	51.5	24.9	<0.01	<0.01	0.17	0.03	<0.01	5.42	0.17	10.4	1.68	0.27	6.21	3.69	104.44
L-3	49.8	28.1	0.02	0.08	0.79	0.03	<0.01	3.66	0.26	10.1	1.28	0.11	4.53	3.78	102.54
L-4	52.0	24.9	<0.01	0.02	0.13	0.03	<0.01	5.36	0.32	9.99	1.75	0.18	6.86	2.36	103.90
L-5	49.3	29.0	0.01	<0.01	0.50	0.05	<0.01	3.90	0.55	10.1	1.40	0.09	5.52	3.33	103.75
L-6	48.8	29.2	<0.01	<0.01	0.39	0.03	0.05	4.48	0.69	7.07	1.14	0.15	5.14	3.01	100.15
L-7	51.9	26.5	<0.01	0.03	0.32	0.04	<0.01	4.00	0.63	9.54	1.42	0.12	5.54	2.75	102.69
L-8	51.6	25.3	<0.01	0.04	0.11	0.06	0.01	5.12	0.70	9.92	1.43	0.17	6.72	2.19	103.37
L-9	54.0	20.1	<0.01	<0.01	<0.01	0.07	<0.01	6.44	0.27	9.77	1.83	1.31	8.19	1.93	103.91
L-10	49.9	26.6	<0.01	<0.01	0.18	0.03	0.02	5.17	0.49	9.19	1.65	0.16	7.05	2.28	102.72

Note: Typical lepidolite from various locations in core zone. Crude relationship between the concentration of F in the lepidolite and the excess sum totals is typical of lithium micas (e.g., Fleet, 2003).
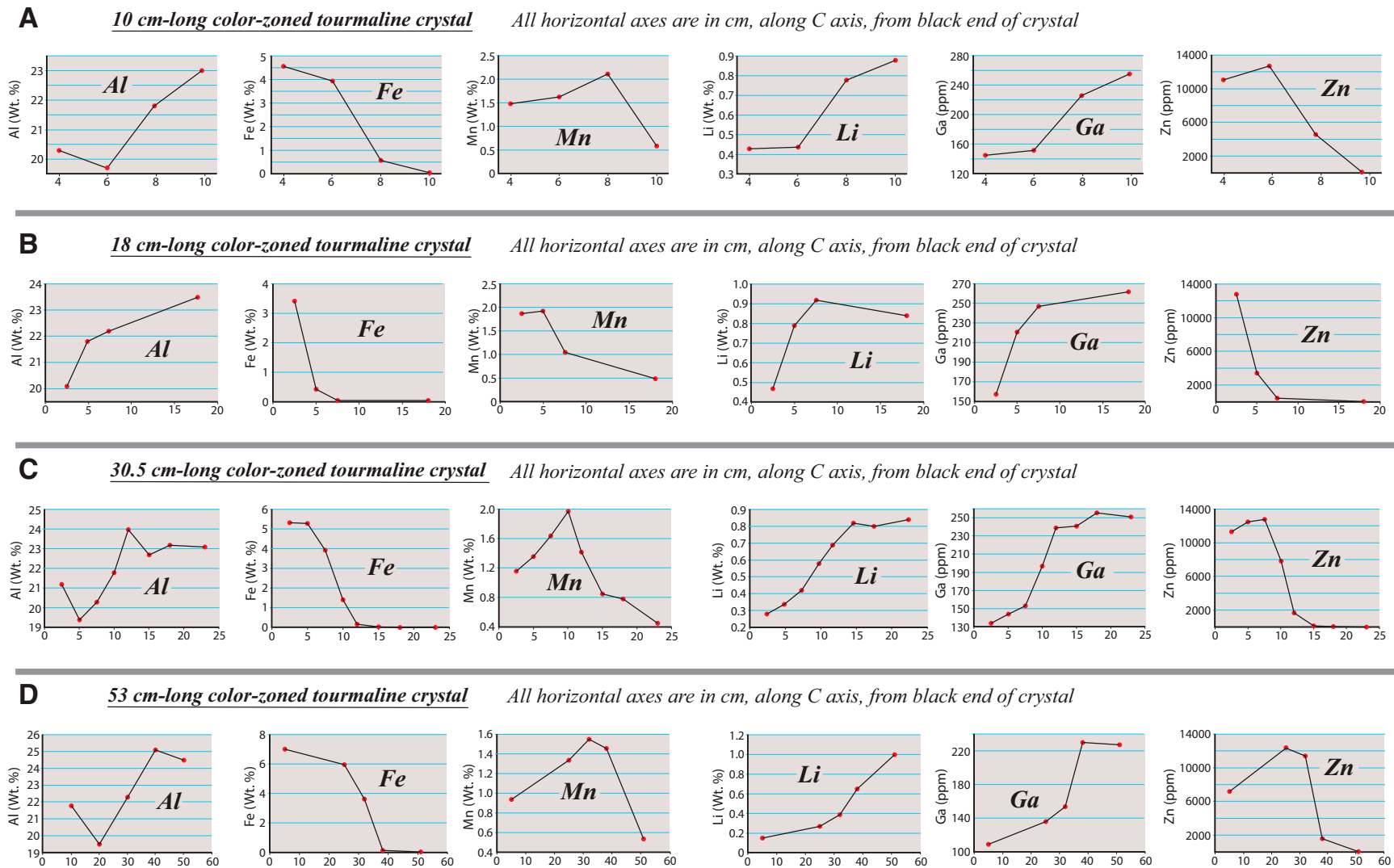
A   *10 cm-long color-zoned tourmaline crystal*   *All horizontal axes are in cm, along C axis, from black end of crystal*

B   *18 cm-long color-zoned tourmaline crystal*   *All horizontal axes are in cm, along C axis, from black end of crystal*

C   *30.5 cm-long color-zoned tourmaline crystal*   *All horizontal axes are in cm, along C axis, from black end of crystal*

D   *53 cm-long color-zoned tourmaline crystal*   *All horizontal axes are in cm, along C axis, from black end of crystal*

Figure 16. Chemistry of selected elements showing the chemical variability of four color-zoned elbaite crystals of different lengths: 10 cm, 18 cm, 30.5 cm, and 53 cm (see Table 6 for analyses). Sample points along the *c* crystallographic axes of the tourmalines are shown by positions of points relative to the horizontal axes of the graphs. Lines connecting analyses are a visual aid for comparisons between the four crystals and do not imply that analyses fall on the lines.

TABLE 6. CHEMISTRY OF SELECTED ELEMENTS FROM BASE TO TERMINUS OF COLOR-ZONED BLACK-TO-PINK ELBAITES OF DIFFERENT LENGTHS, AND A CONCENTRIC COLOR-ZONED GREEN-TO-PINK ELBAITE

Distance above base (cm)	Ti (%)	Al (%)	B (%)	Fe (%)	Mn (%)	Mg (%)	Ca (%)	K (%)	Li (%)	P (%)	F (%)	Cs (ppm)	Ga (ppm)	Rb (ppm)	Sr (ppm)	Zn (ppm)
10-cm-long color-zoned elbaite																
4	0.02	20.3	3.13	4.56	1.49	<0.01	0.2	<0.1	0.43	0.02	0.76	5.9	145	4.7	10.5	11,100
6	0.04	19.7	3.14	3.94	1.64	<0.01	0.2	<0.1	0.44	0.06	0.84	1.7	152	3.8	7.0	12,700
8	0.01	21.8	3.22	0.57	2.12	<0.01	0.2	<0.1	0.78	0.02	0.86	1.1	226	2.9	4.3	4620
10	<0.01	23.0	3.16	0.04	0.60	0.02	0.1	<0.1	0.88	0.01	0.68	3.7	255	13.5	8.0	59
18-cm-long color-zoned elbaite																
2.5	0.03	20.1	3.15	3.42	1.87	0.014	<0.1	<0.1	0.47	0.01	0.76	1.2	158	3.8	7.5	12,800
5	<0.01	21.8	3.18	0.44	1.92	<0.01	<0.1	<0.1	0.79	<0.01	—	0.9	221	2.9	4.2	3450
7.5	<0.01	22.2	2.94	0.05	1.05	0.02	<0.1	<0.1	0.92	<0.01	0.68	1.1	247	3.1	2.0	465
18	<0.01	23.5	3.27	0.05	0.49	<0.01	0.1	<0.1	0.84	0.02	0.58	1.8	262	11	7.9	12
30.5-cm-long color-zoned elbaite																
2.5	0.03	21.2	2.82	5.34	1.16	0.03	0.1	<0.1	0.28	<0.01	0.54	3.4	134	34.5	6.1	11,300
5	0.02	19.4	3.07	5.29	1.36	<0.01	0.1	0.1	0.34	<0.01	0.65	7.6	144	64.8	8.7	12,500
7.5	0.03	20.3	3.06	3.93	1.64	<0.01	0.1	<0.1	0.42	6.00	0.77	2.1	153	5.7	6.7	12,800
10	0.02	21.8	3.04	1.41	1.97	<0.01	0.1	<0.1	0.58	<0.01	0.91	4.9	197	28.8	4.8	7880
12	0.01	24.0	2.86	0.17	1.42	0.02	0.2	<0.1	0.69	<0.01	0.73	6.5	239	35.1	5.8	1690
15	0.03	22.7	3.03	0.03	0.85	0.01	0.2	0.2	0.82	0.02	0.91	56	241	270	6.4	151
18	<0.01	23.2	3.03	0.02	0.78	0.02	0.2	<0.1	0.80	0.01	0.74	8.9	256	51.3	4.8	91
23	<0.01	23.1	3.01	0.02	0.45	0.02	0.1	<0.1	0.84	<0.01	0.61	10.6	251	53.2	3.1	43
53-cm-long color-zoned elbaite																
5	0.02	21.8	2.81	7.04	0.94	0.01	0.1	<0.1	0.15	<0.01	0.16	0.5	109	0.9	9.2	7190
25	0.03	19.5	3.07	6.00	1.34	<0.01	0.1	0.1	0.27	<0.01	0.56	7.3	136	65.2	7.4	12,400
32	0.03	22.3	2.86	3.63	1.55	0.01	0.1	<0.1	0.39	<0.01	0.71	1.9	154	1.6	7.1	11,400
38	<0.01	25.1	2.81	0.14	1.46	0.02	0.2	<0.1	0.65	<0.01	0.24	4.7	230	38.4	7.8	1630
51	<0.01	24.5	2.53	0.03	0.54	0.02	0.3	0.2	1.00	0.02	0.94	35.8	227	265	7.8	69
Concentric-zoned elbaite																
Interior	0.02	23.5	2.79	2.02	1.82	0.02	0.4	<0.1	0.48	0.13	0.83	5.8	172	103	15.4	9130
Rim	0.01	26.0	2.63	0.13	1.32	0.03	0.08	0.1	0.61	0.33	0.79	10.6	213	89.1	31.6	1510

Note: Also see Figure 14 for graphical representation of the analyses.

TABLE 7. SCHORL FROM TOP OF CORE ZONE AND LOWER PERTHITE ZONE

Sample no.	Distance above core zone (cm)	Al (%)	Fe (%)	Mn (%)	F (ppm)	B (ppm)	Ga (ppm)	Li (ppm)	Rb (ppm)	Sr (ppm)	Sn (ppm)	Zn (ppm)
T6	155	18.6	8.40	0.78	4030	30700	93	1430	2.7	6.9	11	5850
T5	125	18.4	8.64	0.66	4750	30900	91	1620	1.0	6.9	11	4870
T4	112	18.4	8.13	0.82	3810	30600	95	1630	2.6	4.5	11	6150
T3	97	18.7	8.99	0.72	4550	31400	109	1500	3.0	5.5	13	5480
T2	66	19.5	8.21	0.96	3920	30900	99	1720	11.2	2.8	13	5920
T1	0	19.5	5.03	1.5	6230	31500	134	3260	8.1	6.7	22	12900

Note: Sample T1 is from the uppermost core zone, and samples T2 through T6 are from the indicated distances into the lower perthite zone. Also see Figure 15 for graphical representation of the analyses.

were analyzed (Table 8) to determine if the high Zn content of the Stewart tourmalines was typical or anomalous. Comparison of pegmatite tourmaline analyses from the numerous districts showed that schorl and green elbaite from Li-pegmatites throughout the NPRB consistently have high Zn content. Schorl from non-Li-bearing pegmatites in the Lakeview Mountains pluton has ZnO content that ranges from 0.23 to 0.24 wt%, and in pegmatites in the Green Acres gabbro, ZnO content that ranges from 0.17 to 0.19 wt%. The Zn content in these latter schorls is relatively low compared to those in the Li-bearing pegmatites (Table 8), but it is relatively high compared to Zn-bearing tourmaline (e.g., Adlakha and Hattori, 2016; Kassoli-Fournaraki and Michailidis, 1994; Roda-Robles et al., 2004). The highest Zn value, 4.42 wt%, was from a green elbaite from the Ocean View pegmatite, which is located less than 2 km northeast of the Stewart pegmatite.

High-Zn tourmaline is found in the McCombre pegmatite, Ontario, Canada (Tindle et al., 2005), pegmatites in the Borborema Pegmatite Province, Brazil (Soares et al., 2008, 2009), and the Julianna System, Poland (Pieczka et al., 2018), although these are pegmatites hosted in metamorphic rocks. The geologic settings of these pegmatites suggest the pegmatites are unlike the Pala district pegmatites in that they are not hosted by low-Sr_i gabbro/tonalite. It appears NPRB pegmatites hosted by low-Sr_i gabbro/tonalite may be relatively unique with respect their high Zn content.

Autometasomatically altered elbaite is widespread in the upper part of the core zone. Altered elbaite consists of a mixture of high-potassium zeolites and clays. Autometasomatism removed most of the B, Mn, Li, Na, and F and increased Si and K (Table 9).
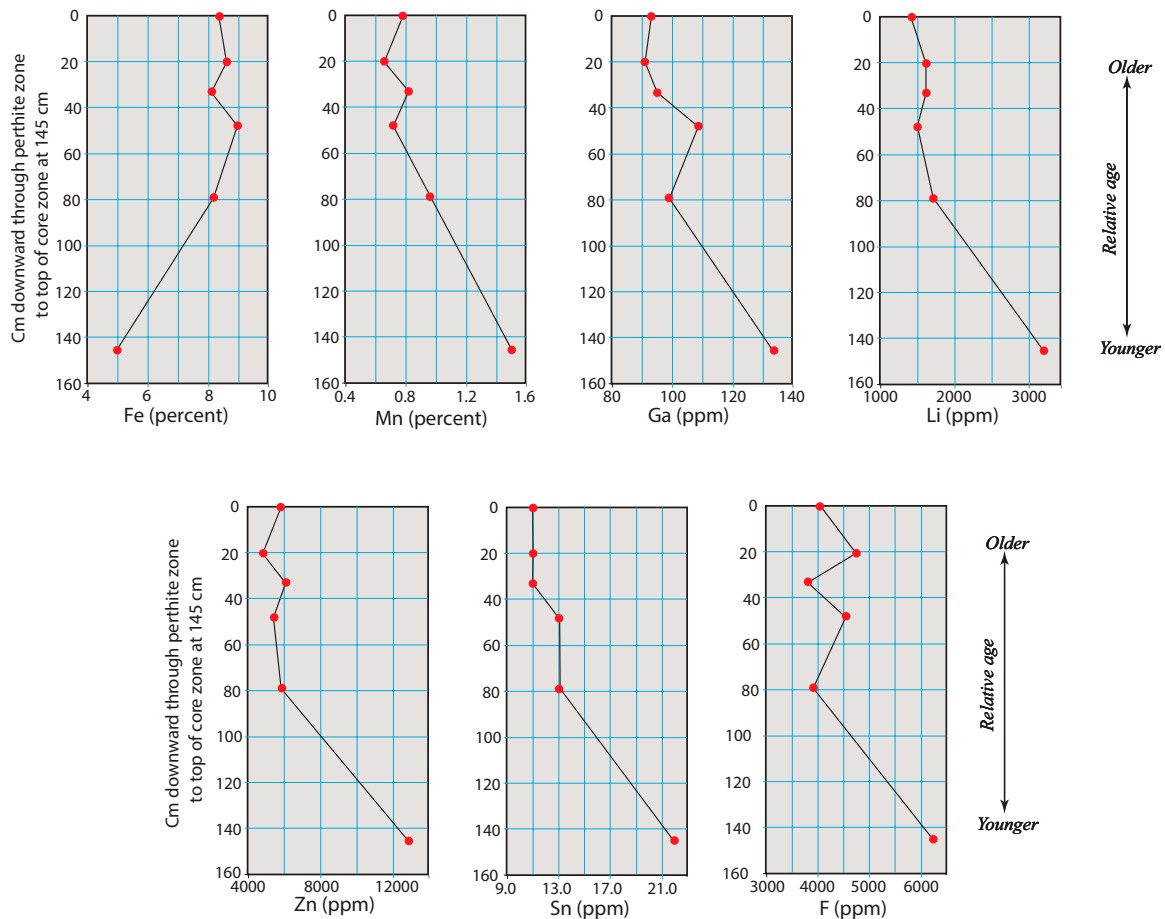
Figure 17. Selected element chemistry of schorl from the lower 145 cm of the perthite zone to the uppermost core zone. Lines connecting analyses are a visual aid for comparisons between elements and do not imply that analyses fall on the lines.

TABLE 8. COMPARISON OF ZnO IN STEWART DIKE TOURMALINES WITH ZnO IN TOURMALINES FROM OTHER LITHIUM PEGMATITES IN THE NORTHERN PENINSULAR RANGES BATHOLITH, AND WITH ZnO IN LAKEVIEW MOUNTAINS PLUTON AND GREEN ACRES GABBRO RARE EARTH ELEMENT PEGMATITES

Host rock	ZnO (%)		
Lakeview pluton pegmatites	0.24	0.23	—
Green Acres pluton pegmatites	0.19	0.17	—
Coahuila Mtn pegmatite	0.30	—	—
Stewart pegmatite	1.82	1.75	1.71
Oceanview pegmatite	2.34	4.22	1.77
White Queen pegmatite	0.63	0.32	0.49
Mission pegmatite	0.43	0.63	0.44
French Pete pegmatite	0.60	0.35	—
Blue Lady pegmatite	0.32	—	—
Emeralite pegmatite	0.24	—	—
Himalaya pegmatite	0.72	0.77	0.77

Note: Himalaya zinc values from Erlt et al. (2010).

Spodumene. Moderately abundant to abundant clusters and "jack-straw" masses of autometasomatically altered spodumene occur mostly above the basal lepidolite masses. These masses are 1–2 m thick and up to 10 m in length. Most crystals range in length from 15 to 60 cm (Fig. 10). The altered spodumene crystals consist of kaolinite, dickite, quartz, and spodumene. One X-ray diffraction (XRD) pattern indicated the presence

of tridymite. Alteration is largely hydration but includes decreases in Li and Si, and increases in Mg, Ca, Ba, Cs, and Sr (Table 10).

Spodumene is present, but rare, in the upper part of the perthite zone where the zone transitions to the upper intermediate zone. In the perthite zone, spodumene occurs as polycrystalline fine-grained to 0.5-cm-size crystals coexisting with quartz and thin seam-like concentrations of light pink elbaite needles up to 1.5 cm in length. Altered spodumene occurs within 1- to 2-m-size masses of quartz and albite containing abundant small petalite crystals, quartz, and minor muscovite. In these large quartz-albite masses, the altered spodumene occurs mostly as clusters of 1–6-cm-long white to light pink prisms and less commonly as isolated individual prisms up to 10 cm in length. Autometasomatic alteration of this spodumene was not the result of hydration reactions like the alteration of spodumene in the core zone. Alteration here significantly increased silica and significantly decreased alumina (Table 10). Pink quartz, interstitial to the altered spodumene, includes extremely small crystals of petalite and lepidolite. Very fine-grained, centimeter-size masses of lepidolite and included amblygonite, kaolinite, tosudite, and quartz are scattered through the large quartz-albite masses.

Petalite. Dark brown masses of petalite intergrown with heulandite, clinoptilolite, and minor quartz and lepidolite occur in the core zone above the spodumene and commonly fill interstices between altered spodumene crystals (Fig. 10). Some small masses are essentially all petalite (Fig. 18). The chemistry of petalite-heulandite rock is given in Table 11.

TABLE 9. CHEMISTRY OF AUTOMETASOMATIC ALTERED ELBAITE FROM THE UPPER PART OF THE CORE ZONE

Sample no.	SiO_2 (%)	TiO_2 (%)	B_2O_3 (%)	Al_2O_3 (%)	Fe_2O_3 (%)	MnO (%)	MgO (%)	CaO (%)	Na_2O (%)	K_2O (%)	Li_2O (%)	Rb_2O (%)	P_2O_5 (%)	F (%)	LOI (%)	Sum (%)	Ba (ppm)	Cs (ppm)	Sr (ppm)	Zn (ppm)
AE-1	40.3	<0.01	4.52	42.2	0.14	0.35	0.08	0.09	0.55	3.96	1.49	0.13	0.03	0.21	8.52	102.57	25.5	83.9	14.4	57
AE-2	45.4	<0.01	0.19	37.9	0.04	0.11	0.09	0.03	0.28	9.97	0.14	0.34	<0.01	0.04	5.91	100.44	7.9	343	8.6	28
AE-3	41.9	<0.01	2.46	41.1	0.03	0.10	0.09	0.06	0.44	6.17	0.90	0.21	<0.01	0.08	7.54	101.08	7.1	155	7.2	29
AE-4	44.5	<0.01	0.55	39.2	0.04	0.08	0.06	0.02	0.27	9.15	0.37	0.31	<0.01	0.05	6.05	100.65	7.1	373	8.9	19
AE-5	46.6	<0.01	0.15	38.3	0.02	0.12	0.12	0.03	0.31	10.6	0.04	0.38	<0.01	0.04	5.04	101.75	6.7	265	10.3	30
AE-6	45.7	0.04	0.17	36.6	2.13	0.08	0.12	<0.01	0.74	10.3	0.09	0.28	0.01	0.66	5.10	102.12	5.2	83.8	5.2	230
AE-7	44.1	0.04	1.34	39.2	0.40	0.21	0.10	0.00	0.43	8.36	0.52	0.28	0.02	0.18	6.36	101.44	9.9	217.3	9.1	66

Note: Elbaite samples taken where the Core Zone is a complex of lithium and boron mineral segregations.

TABLE 10. ANALYSES OF UNALTERED SPODUMENE FROM A MIAROLITIC CAVITY, ALTERED SPODUMENE FROM THE CORE ZONE,
AND ALTERED SPODUMENE FROM THE PERTHITE ZONE TO UPPER INTERMEDIATE ZONE

		Sample no.	SiO_2 (%)	Al_2O_3 (%)	MnO (%)	MgO (%)	CaO (%)	Na_2O (%)	Li_2O (%)	P_2O_5 (%)	F (%)	LOI (%)	Sum (%)	B (ppm)	Ba (ppm)	Cs (ppm)	Ga (ppm)	Rb (ppm)	Sr (ppm)
Unaltered		S-1	63.4	29.4	0.06	0.01	0.02	0.08	7.54	0.01	<0.01	0.38	100.9	85	8	2	47	1	<0.01
Spodumene, core zone	Altered	AS-1	55.7	30.3	0.08	0.33	0.49	0.07	3.49	0.01	0.02	9.94	100.5	30	66	84	36	7	392
		AS-2	57.2	30.5	0.05	0.31	0.23	0.04	4.80	0.02	0.02	7.56	100.7	30	16	59	31	3	13
		AS-3	60.7	28.9	0.05	0.13	0.02	0.04	5.88	<0.01	0.02	3.96	99.9	50	37	27	34	3	140
		AS-4	64.1	26.1	0.03	0.17	0.72	0.16	5.76	0.02	0.02	4.47	97.1	14	50	NA	NA	NA	680
Spodumene, perthite zone to upper intermediate zone	Altered	AS-5	74.7	19.5	0.05	0.05	0.04	0.28	4.71	0.01	NA	0.98	100.5	60	1	7	15	90	5
		AS-6	79.8	15.8	0.02	0.04	0.02	0.41	4.05	0.02	NA	0.42	100.7	<0.01	1	4	12	42	3
		AS-7	78.6	17.0	0.01	<0.01	0.02	0.37	4.15	0.01	NA	0.49	100.7	<0.01	2	3	13	23	2
		AS-8	77.6	16.8	0.02	0.06	0.03	0.74	3.66	0.01	NA	0.82	99.9	280	<0.05	8	13	74	1
Unaltered spodumene			63.4	29.4	0.06	0.01	0.02	0.08	7.54	0.01	<0.01	0.38		85	8	2	47	1	<0.01
Altered C.Z. spodumene average			59.4	29.0	0.05	0.24	0.41	0.08	4.98	0.02	0.02	7.16		31	42	57	34	4	306
Altered P.Z. to U.I.Z spodumene average			77.7	17.3	0.02	0.05	0.03	0.45	4.14	0.01	NA	0.68		40	1	6	13	57	2
Δ unaltered minus C.Z. altered			−4.0	−0.4	−0.01	+0.23	+0.39	0.00	−2.56	+0.01	—	+6.78		−54	+34	+55	−13	+3	+306
Δ unaltered minus P.Z. to U.I.Z. altered			+14.3	−12.1	−0.04	+0.04	+0.01	+0.37	−3.40	0.00	—	+0.30		−45	−7	+4	−34	+56	+2

Note: Table shows comparison of each with unaltered spodumene. LOI—loss on ignition; NA—not applicable; C.Z.—core zone; P.Z.—perthite zone; U.I.Z.—upper intermediate zone.
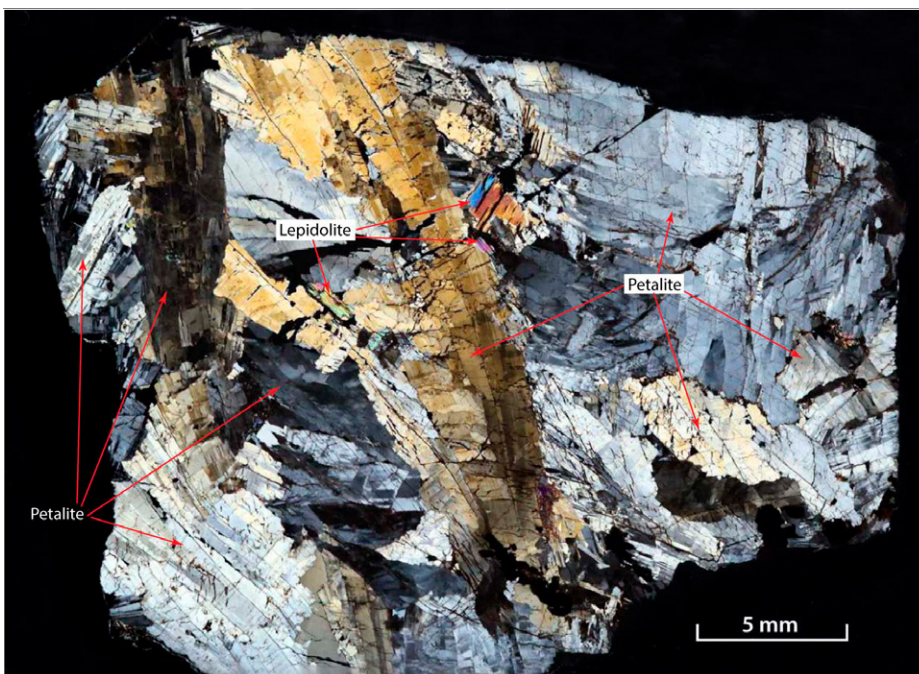

Figure 18. Photomicrograph of petalite and minor lepidolite from the core zone. Crossed nicols.

TABLE 11. ANALYSES OF PETALITE-HEULANDITE FROM CORE ZONE WHERE THE CORE ZONE IS A COMPLEX OF LITHIUM
AND BORON MINERAL SEGREGATIONS

Sample no.	SiO_2 (%)	Al_2O_3 (%)	CaO (%)	MgO (%)	MnO (%)	K_2O (%)	Na_2O (%)	Li_2O (%)	LOI (%)	Sum (%)	F (ppm)	Ba (ppm)	Cs (ppm)	Rb (ppm)	Sr (ppm)
PH-1	69.9	15.4	3.23	0.08	<0.01	0.64	0.42	2.22	8.54	100.43	<25	19.3	670	20.6	48.1
PH-2	69.4	16.5	2.03	0.03	<0.01	0.51	2.15	2.35	7.04	100.01	40	15.0	4060	28.6	42.0
PH-3	69.4	18.8	2.03	0.14	0.04	0.19	0.16	3.38	6.17	100.31	100	38.0	423	24.2	580
PH-4	71.0	15.4	2.88	0.20	0.02	0.28	0.35	2.50	7.95	100.58	40	22.5	595	11.0	441
PH-5	68.7	15.2	3.61	0.29	0.03	0.37	0.55	1.80	9.96	100.51	40	24.2	1090	14.0	714

Note: Petalite and heulandite are intergrown to such a degree that they could not be separated for analysis. Analyses of the mixed pairs are presented here to show bulk compositions. LOI—loss on ignition.

TABLE 12. ANALYSES OF ALTERED AND UNALTERED AMBLYGONITE

	Sample no.	SiO_2 (%)	Al_2O_3 (%)	MgO (%)	CaO (%)	MnO (%)	Na_2O (%)	K_2O (%)	P_2O_5 (%)	Li_2O (%)	F (%)	LOI (%)	Sum (%)
Unaltered	A-1	1.14	30.0	0.03	4.77	<0.01	<0.01	<0.01	44.5	7.97	3.06	8.44	102.91
	A-2	1.30	35.0	0.02	0.37	<0.01	0.04	0.03	46.7	9.39	4.48	6.15	103.48
	A-3	1.91	33.8	<0.01	2.57	0.02	0.10	0.11	46.0	8.89	4.17	6.04	103.61
	AA-1	28.0	26.7	0.14	17.5	0.06	<0.01	0.03	13.6	0.46	1.07	13.3	100.86
	AA-2	37.1	33.3	0.15	8.02	0.07	0.02	0.03	5.91	0.35	0.47	15.5	100.92
Altered	AA-3	58.6	30.1	0.30	0.21	0.05	0.14	0.01	0.02	1.92	0.02	8.05	99.42
	AA-4	30.0	35.3	0.06	2.82	<0.01	0.04	0.02	14.2	1.0	0.83	16.0	100.27
	AA-5	79.0	16.0	0.02	0.03	0.03	0.11	0.03	<0.01	2.0	0.02	0.61	97.85
Average unaltered		1.45	33.9	0.03	2.57	—	0.07	0.07	45.7	8.75	3.90	6.88	
Average altered		46.5	28.3	0.13	5.72	0.05	0.08	0.02	8.4	1.15	0.48	10.04	
Difference		+45.0	−5.6	+0.10	+3.15	—	+0.01	−0.05	−37.3	−7.60	−3.42	+3.16	

Note: As in the lepidolite, sums greater than 100 are in the high F-bearing amblygonite. LOI—loss on ignition.

Amblygonite. White equant-shaped, 75- to 100-cm-long masses of amblygonite occur in the upper part of the core zone. In 1903, "a large mass of amblygonite," 12 m long, 0.6–4.5 m wide, and 5 m thick at its thickest point, was encountered in the old workings (Jahns and Wright, 1951, p. 59). Most amblygonite is translucent white, but some is transparent light blue. Some crystals consist of amblygonite intergrown with montebrasite. The outer parts of amblygonite masses are autometasomatically altered to a white powdery material depleted in Li, P, and F, and enriched in Si (Table 12).

Lithiophilite. Lithiophilite occurs mainly in the upper part of the core zone above amblygonite, as crystal groups 10–15 cm in width, and less commonly as single crystals 2.5–40 cm in length. Lithiophilite was particularly abundant in the old workings. In the early 1950s, numerous large lithiophilite crystals were exposed as a result of caving in the back of rooms where lepidolite was mined.

All lithiophilite crystals are partly to entirely autometasomatically altered to a variety of secondary phosphates and Fe-Mn oxides/hydroxides and have attracted the attention of mineralogists for many years (e.g., Schaller, 1912). Several phosphate minerals were first described from the Stewart mine. Partly altered crystals have a lithiophilite core typically surrounded progressively by hureaulite, sicklerite, heterosite, phosphosiderite, purpurite, and stewartite (Fig. 19). A more recent study of the phosphates was conducted by Shigley and Brown (1985).

Hypogene clay. Hypogene clay occurs throughout the core zone, interstitially and within elliptical-shaped cavities a few centimeters in diameter. The cavities are commonly lined by inward-projecting quartz and/or cleavelandite crystals. The mineral composition of the clay is variable, consisting of montmorillonite, kaolinite, tosudite, and minor very fine-grained disseminated spodumene, and quartz. No tourmaline was found within these cavities. The chemistry of hypogene clay is given in Table 13.

In the old mine, in the lower part of the core zone, bismuth crystals up to 4 cm in length, some altered to bismutite, were locally abundant

in massive quartz. Bismuth, entirely altered to secondary minerals, is associated with altered spodumene.

Perthite Zone and Autometasomatic Chimneys

Overlying a lepidolite-spodumene-petalite-amblygonite core zone, there is a 3- to 6-m-thick perthite zone, which is essentially monomineralic perthite crystals, up to 3 m in length, but also includes sparsely scattered
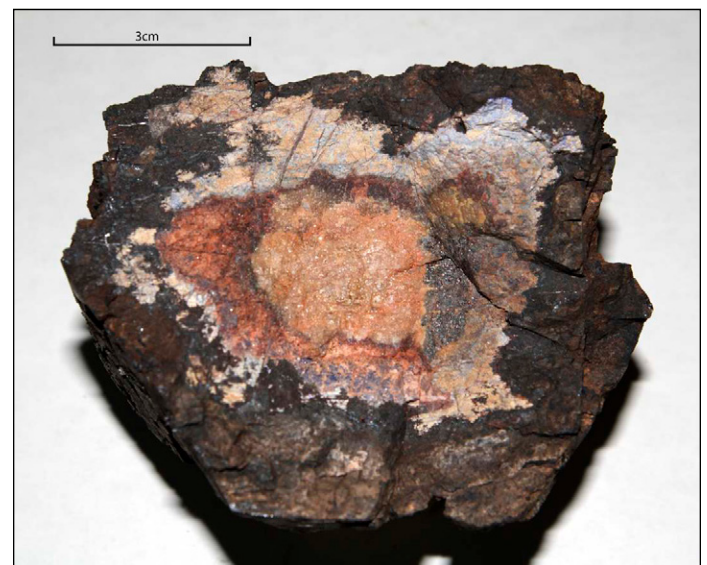

Figure 19. Altered lithiophilite crystal. Core is lithiophilite surrounded by secondary phosphates: hureaulite, sicklerite, heterosite, phosphosiderite, purpurite, and stewartite.

TABLE 13. ANALYSES OF HYPOGENE CLAY THAT FORMS THE MATRIX OF THE MIAROLITIC CAVITIES

Sample no.	SiO_2 (%)	Al_2O_3 (%)	Fe_2O_3 (%)	MgO (%)	CaO (%)	Na_2O (%)	K_2O (%)	MnO (%)	Li_2O (%)	F (%)	LOI (%)	Sum (%)
C-1	51.7	21.7	0.03	3.23	1.09	0.11	0.21	0.53	0.74	0.18	21.5	101.02
C-2	73.4	19.4	0.02	0.26	0.12	0.06	0.10	0.11	4.50	0.06	2.5	100.53
C-3	51.6	20.9	0.21	2.99	1.35	0.10	0.02	0.42	0.04	0.04	23.1	100.77
C-4	52.1	27.4	0.02	1.83	1.52	0.02	0.04	0.21	0.64	0.06	16.6	100.44
C-5	58.4	19.9	0.19	2.16	0.24	0.11	0.32	0.89	0.26	NA	18.1	100.57

Note: LOI—loss on ignition.

muscovite and schorl. This zone probably correlates with "massive quartz with coarse, blocky perthite" and "coarse, blocky perthite" units of Jahns and Wright (1951, their Plate 4). Analyses of K-feldspar from this zone are given in Table 14.

Myriad discrete, upward-tapering autometasomatic bodies, informally termed chimneys, emanate upward from the lepidolite-spodumene-petalite-amblygonite core zone into, and some through, the perthite zone (Fig. 6). The upper part of these chimneys may be what Jahns (1979, p. 19) referred to as "irregular near-vertical feeder paths toward underlying lepidolite lenses or other parts of the main pocket horizon." Most small chimneys, having a basal diameter of ~1 m, are singular, but some bifurcate upward (Figs. 20A and 20B). Most chimneys extend 1.5–5 m into the perthite zone, and some extend entirely through the perthite zone into the upper part of the dike. The larger chimneys commonly branch upward and anastomose, forming a chimney complex (Fig. 21). Some chimneys have a planar boundary along a crystal, cleavage face, or planar fracture of the host perthite (Figs. 20A, 20B, and 21).

Chimneys are concentrically zoned, consisting of an outer layer of coarse-grained muscovite-albite-quartz-perthite granite and an interior core of fine-grained white albite. Muscovite is absent or sparse in approximately the lower 30 cm of a chimney, where there is also an abrupt substitution of albite for perthite. Additionally, at the transition from the core zone to the perthite zone and extending ~30 cm, or rarely a meter, into the perthite zone, the interiors of chimneys consist of lepidolite and albite (Figs. 20A and 20B). Albite interiors consist of radial platy albite aggregates 2–3 cm in length. Schematic cross-section chemistry of the medial part of chimney 1 (Figs. 20A and 20B) is given in Figure 22 and Table 15.

Schorl occurs in the apexes of chimneys. In chimneys having a broad terminus, schorl occurs as radiating sprays and randomly oriented crystals, 15–60 cm in length (Fig. 23). In chimneys that taper upwards to a "point," schorl crystals are oriented parallel or subparallel to the chimney walls. The apices of chimneys that extend beyond the perthite zone consist largely of quartz and schorl crystals up to 90 cm in length. The schorl commonly includes disseminated muscovite. Some schorl extends above the albite core as individual crystals surrounded by a corona of quartz (Fig. 24). The compositions of schorl from the apices of chimneys in the perthite zone and those that extend above the perthite zone are given in Table 16. The only noticeable chemical difference between the two schorl sets is a roughly three times greater amount of fluorine and zinc in the schorl from the chimneys that extend above the perthite zone. Single lithiophilite crystals occur in the lower albite interior of some chimneys (Figs. 20A, 20B, and 23).

The relatively small chimney 1, exposed from its base to its terminus (Figs. 20A and 20B), was selected for detailed study. Muscovite was collected at intervals from the base to the terminus on both sides of the chimney. Muscovite chemistry systematically changes in the 1.85 m from the base to the terminus of the chimney (Table 17). Of the major elements, Mn decreases from 0.23 to 0.13 wt% on the right side of the chimney and from 0.21 to 0.10 wt% on the left side. Cesium has the greatest variation of the minor elements, decreasing from 162 ppm at the base to 58 ppm at the terminus on the right side. On the left side, Cs decreases from 132 ppm to 44 ppm. Li, Rb, Sn, and Zn all decrease from the base to the chimney apex (Fig. 25).

Albite was collected at 30 cm intervals from the base of the albite interior to the apex. From the base to near the apex, K_2O, Cs, and Rb gradually decrease upward, but then they show a strong increase at the apex. This increase at the apex is interpreted to reflect incomplete replacement of perthite (Fig. 26). The trace-element composition of albite in the chimney's interior differs significantly from that in the core zone albite: B, Cs, Li, Rb, and Sr are notably higher in the core zone (Table 4).

Volume of autometasomatic rock. Calculation of the volume of the autometasomatically altered perthite zone was based on point counts

TABLE 14. ANALYSES OF POTASSIUM FELDSPAR FROM THE PERTHITE ZONE AND FROM MIAROLITIC CAVITIES

	SiO_2 (%)	Al_2O_3 (%)	Fe_2O_3 (%)	MgO (%)	CaO (%)	Na_2O (%)	K_2O (%)	Li_2O (%)	Rb_2O (%)	Cs_2O (%)	BaO (%)	P_2O_5 (%)	LOI	Sum
	64.3	19.7	0.03	0.04	0.04	1.74	13.6	0.06	0.43	0.02	0.001	0.21	1.02	101.19
Perthite zone	64.9	18.9	0.05	0.03	0.01	2.22	13.1	0.06	0.45	0.02	<0.001	0.17	0.33	100.24
	65.1	19.2	0.08	0.02	<0.01	2.71	12.5	0.07	0.27	0.01	<0.001	0.16	0.35	100.47
	65.1	19.0	0.04	0.02	0.01	2.91	12.2	0.06	0.21	0.01	0.001	0.16	0.57	100.29
	62.1	19.9	0.01	0.03	<0.01	1.04	14.3	0.60	0.42	0.27	0.110	0.19	1.17	100.14
Cavities	63.0	19.0	0.03	0.03	<0.01	1.12	14.3	0.13	0.68	0.25	0.001	0.37	0.80	99.71
	62.3	20.3	<0.01	0.06	<0.01	1.07	14.2	0.10	0.44	0.28	0.180	0.22	0.66	99.81
	62.4	18.6	0.03	0.02	<0.01	1.06	14.4	0.12	0.58	0.22	0.030	0.28	0.70	99.44
Perthite zone average	64.8	19.2	0.05	0.03	—	2.40	12.8	0.06	0.34	0.02	—	0.18		
Cavities average	62.4	19.4	—	0.04	—	1.07	14.3	0.24	0.53	0.26	0.080	0.26		
Percent increase or decrease in cavities	−4	+1		+25		−124	+10	+75	+36	+93		+31		

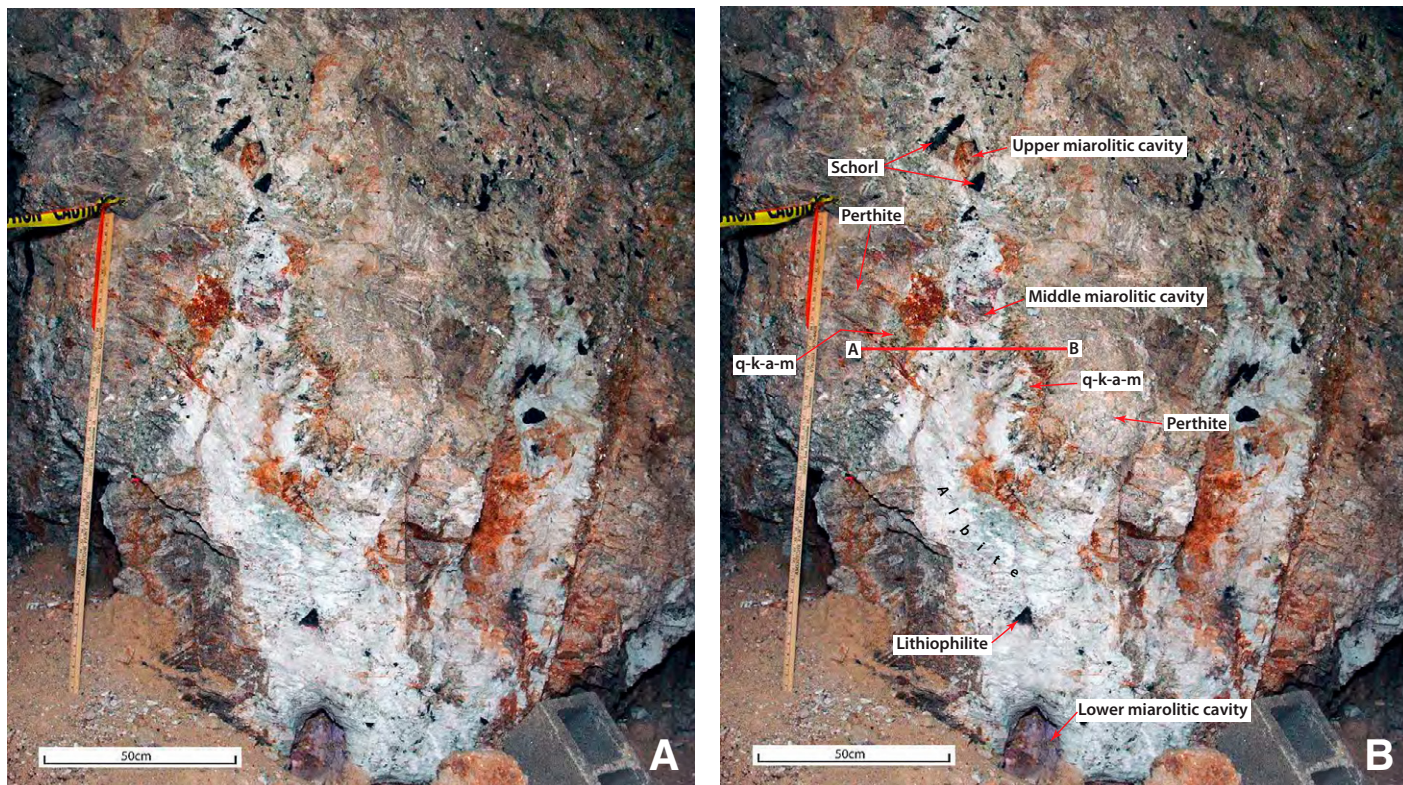*Note*: LOI—loss on ignition.

Figure 20. Small bifurcated chimney in the basal part of the perthite zone. Chimney on left, termed chimney 1, had three miarolitic cavities; the lower cavity was in lepidolite; upper cavities were in albite. This chimney was sampled for muscovite and albite chemistry (Tables 4 and 17; also see Fig. 25). Note that schorl is restricted to the upper part of the chimneys. Triangular-shaped black crystal ~20 cm above the lowest cavity is altered lithiophilite. q-k-a-m—quartz–K feldspar–albite-muscovite rock. (A) Photograph without annotation, which would obscure some features. (B) Photograph with annotated features discussed in text.
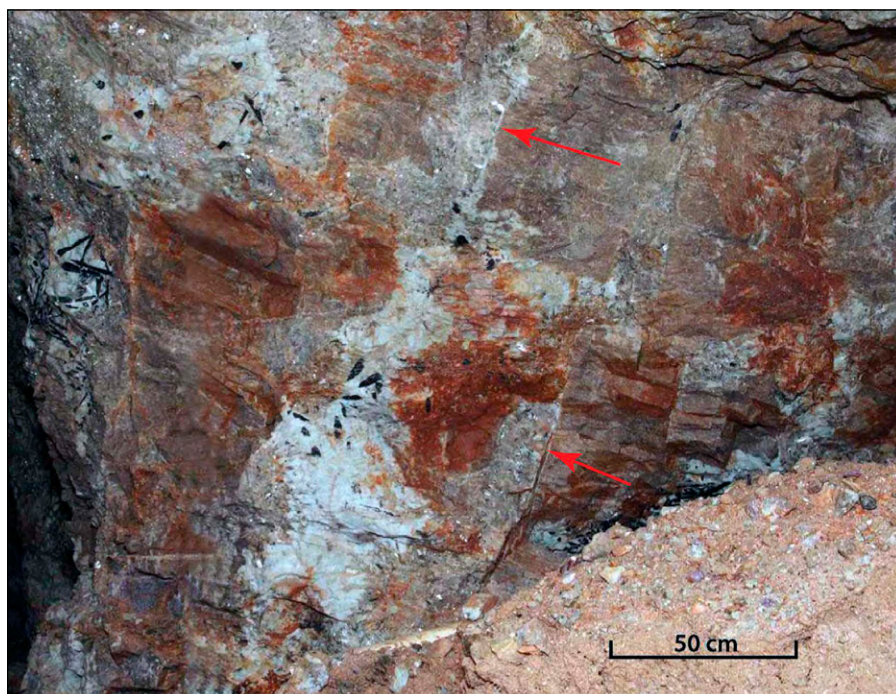
Figure 21. Chimney complex in the perthite zone. Light brown rock hosting the chimneys consists of massive perthite crystals. Straight contact indicated by arrows is chimney material emplaced against a perthite crystal face almost 50 cm long.
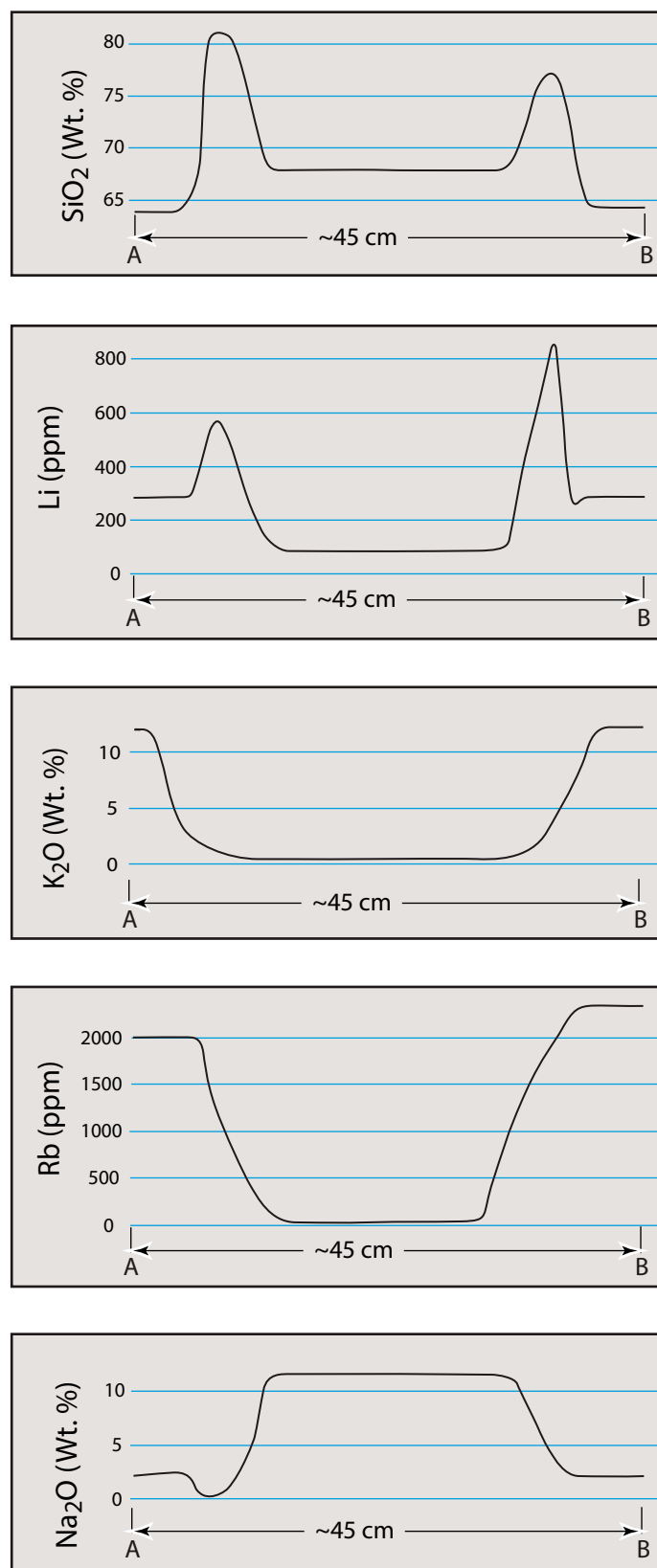
Figure 22. Selected elements from whole-rock chemical analyses across the medial part of chimney 1 (sampling was along the line A–B shown in Fig. 20B). The quartz–K feldspar–albite-muscovite outer part of the chimney is reflected in all the curves, as is the albite core of the chimney.

on vertical exposures at 14 surface and underground locations. The size of the areas point counted underground ranged from 2 to 3 m wide and 2–2.5 m high. Surface locations covered a width of ~5 m. Points counted at each location ranged from 98 to 216 and averaged 133. Based on point counts, the lower 2–3 m of the perthite zone ranges from 34% to 78.5% autometasomatic chimneys and averages ~53% (Table 18).

Based on a 1:240 scale mine map of the underground workings within the perthite zone, ~10,400 m^2 of the perthite zone has been excavated. The thickness of the excavated part of the perthite zone, with included chimneys, averages ~2.5–3 m, resulting in a volume of ~26,000 m^3 excavated, roughly half of which was autometasomatized rock. Based on the excavated volume, percentage autometasomatized, and the perthite and chimney chemistry, autometasomatism decreased K_2O by ~7% and increased Na_2O by ~9% for ~13,000 m^3 of the perthite zone.

Miarolitic cavities. With the exception of the Stewart dike, gem-bearing pegmatites in the Pala pegmatite district appear to conform to Jahns' subdivision category: "asymmetrically zoned pegmatite dike with aplitic footwall portion," with crystal-bearing cavities located below "very coarse-grained perthite" (Jahns, 1982, p. 296–297). Foord and Shigley (1991, p. 132) stated that for gem-bearing pegmatites of San Diego County, "the main pocket zone or horizon ordinarily is found along the footwall side of these coarse-grained units" of the core zone. Contrary to these relationships found in other gem-bearing dikes of the NPRB, an inspection of over 100 gem-bearing miarolitic cavities in the Stewart dike showed that all cavities, without exception, were located in the autometasomatic chimneys above the core zone in the perthite and upper intermediate zones.

However, Jahns (1979, 1982) mapped a vertical cross section of a 22 × 8 cm miarolitic cavity in the "back of old exploratory drift" (Jahns, 1979, p. 20) and later described it as located in the "lower main workings of the Stewart mine" (Jahns, 1982, p. 306). This cavity is unlike the cavities we examined. Jahns' map shows most of the miarolitic cavity wall is perthite with lesser quartz, schorl, and albite. It is not clear where the location of this cavity is in the dike.

Miarolitic cavities, commonly referred to as pockets by gemstone miners, are located in the cores of chimneys. The cavities range in size from a few cubic centimeters to 2.5 m^3. Gem elbaite, spodumene (kunzite), beryl (morganite), K-feldspar, and quartz are restricted to these cavities. Crystals line the cavity walls and occur as isolated euhedral crystals within the cavity interior. Inward-growing lepidolite or cleavelandite, quartz, and elbaite, and less commonly beryl, spodumene, and K-feldspar, line the cavity walls. Elbaite commonly occurs at the crest of cleavelandite mounds (Fig. 27). K-feldspar occurs as large, up to 8 cm, corroded colorless transparent crystals on the cavity wall. Compared to K-feldspar in the perthite zone, the K-feldspar in the miarolitic cavities is higher in K, Li, and Cs, and lower in Ca, Na, and Fe (Table 14). The cavity interiors are filled by hypogene clay and zeolites, which act as a matrix for included broken crystals, euhedral quartz, elbaite, spodumene, beryl, muscovite, and lepidolite crystals. As noted by Jahns et al. (1974, p. 198), the major mineralogy within a cavity is consistent ".... but varied considerably from one pocket to another."

In chimneys with multiple miarolitic cavities, the mineralogy of individual cavities systematically changes relative to the position of the cavity in the chimney. Pink elbaite, morganite, and kunzite occur in cavities in the lower parts of chimneys, bicolored elbaite occurs in intermediate positions, and green elbaite occurs in the highest parts. The chimney shown in Figures 20A and 20B contained three small miarolitic cavities. The lowest cavity, 15 × 20 cm, located where the chimney core changes from lepidolite to albite, contained pink elbaite and kunzite. The intermediate cavity, 10 × 13 cm, contained bicolored pink-green elbaite and

Figure 23. Schorl sprays in the upper parts of a chimney complex in the perthite zone. Lower large black crystal is altered lithiophilite (arrow). Note schorl crystals widen toward the terminal ends. Units of ruler are inches.
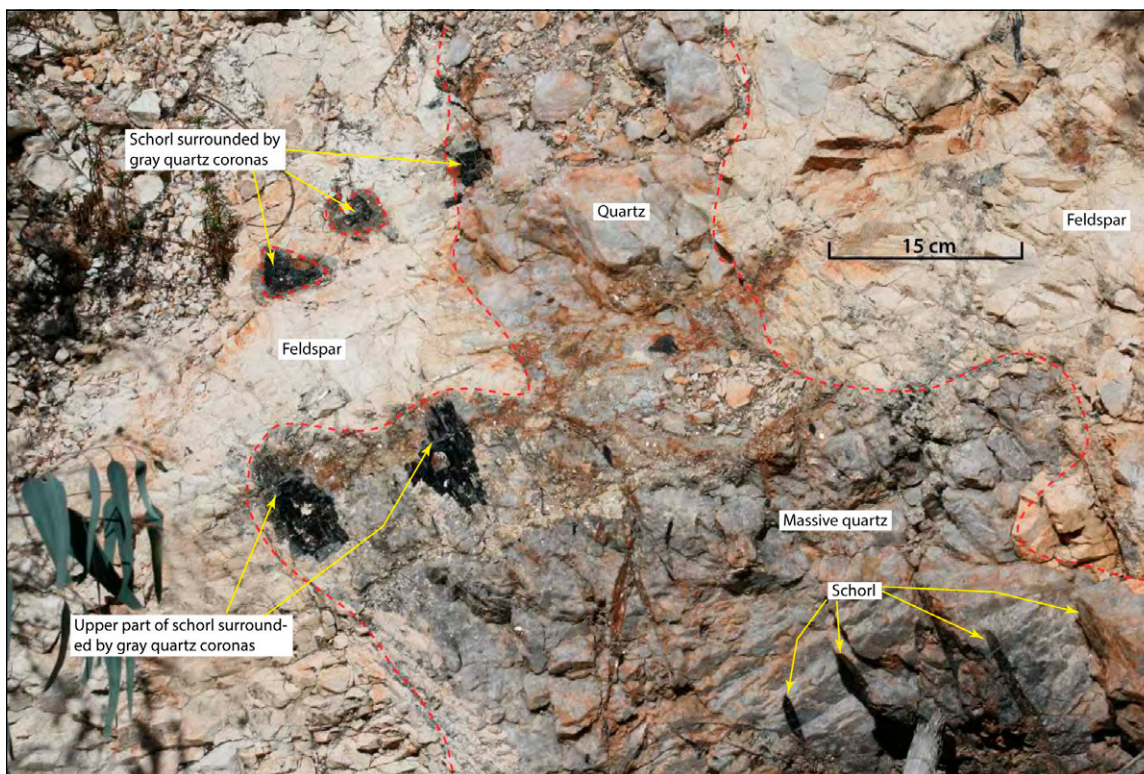

Figure 24. Schorl surrounded by coronas of gray quartz in the uppermost part of a chimney in the perthite zone. Dashed red line roughly outlines the chimney. *C* axis of schorl crystals is oriented parallel to chimney length.

TABLE 15. WHOLE-ROCK CHEMISTRY CROSS SECTION OF CHIMNEY 1

Sample description	SiO₂ (%)	Al₂O₃ (%)	Fe₂O₃ (%)	MgO (%)	CaO (%)	Na₂O (%)	K₂O (%)	MnO (%)	P₂O₅ (%)	LOI (%)	Sum (%)	Ba (ppm)	Bi (ppm)	Cs (ppm)	Ga (ppm)	Li (ppm)	Rb (ppm)	Sr (ppm)	Sn (ppm)	Ta (ppm)	Tl (ppm)	Zn (ppm)	Zr (ppm)
Perthite outside chimney (left side)	64.5	18.8	0.03	0.05	0.02	2.84	12.20	0.02	0.16	0.38	99.00	3	2	49	15	310	2010	4.0	1	<0.5	16	<0.5	<0.5
Outer part of outer layer of chimney (left side)	81.1	12.7	0.75	0.03	<0.01	0.64	3.25	0.08	<0.01	1.71	100.26	6	0.02	23	51	580	1050	1.0	41	3	6	148	1
Inner part of outer layer of chimney (left side)	74.3	16.9	0.36	0.04	0.06	6.19	1.99	0.07	0.08	1.00	100.99	4	1	21	39	400	708	1.0	25	3	4	86	1
Albite core of chimney	68.4	20.0	0.06	0.07	0.16	11.5	0.20	0.06	0.18	0.33	100.96	5	2	5	24	70	27.5	1.0	1	1	<0.5	6	0.5
Inner part of outer layer of chimney (right side)	73.6	16.8	0.36	0.07	0.03	4.70	2.50	0.07	0.05	0.15	99.68	6	1	65	45	880	866	<0.1	30	2	5	96	17
Outer part of outer layer of chimney (right side)	77.0	12.8	0.20	0.03	0.01	2.07	7.17	0.01	0.10	0.53	99.92	5	1	31	14	280	1300	0.3	4	1	10	14	1
Perthite outside chimney (right side)	64.1	18.8	0.04	0.04	<0.01	2.56	12.40	0.02	0.17	0.34	98.47	4	2	69	16	310	2360	1.0	3	<0.5	19	<0.5	<0.5

Note: See also Figure 22. LOI—loss on ignition.

TABLE 16. CHEMISTRY OF SELECTED ELEMENTS FOR SCHORL IN CHIMNEYS IN THE PERTHITE ZONE, AND CHIMNEYS ABOVE THE PERTHITE ZONE

	Ti (%)	Al (%)	B (%)	Fe (%)	Mn (%)	Mg (%)	Ca (%)	K (%)	Li (%)	F (%)	Cs (ppm)	Ga (ppm)	Rb (ppm)	Sr (ppm)	Zn (ppm)
A Schorl in the apex of chimneys in the perthite zone	0.08	17.3	3.05	8.85	0.23	0.95	<0.1	0.1	0.02	0.14	0.5	112	9.8	7.0	1630
	0.05	17.8	3.08	9.52	0.52	0.12	<0.1	<0.1	0.06	0.18	0.8	114	3.3	6.5	3540
	0.07	17.5	3.05	9.57	0.45	0.20	<0.1	<0.1	0.06	0.19	1.0	103	4.3	5.5	3260
	0.07	17.4	3.00	9.47	0.51	0.16	<0.1	<0.1	0.07	0.23	2.2	104	4.4	5.5	3520
	0.07	18.5	2.96	9.58	0.48	0.17	0.1	0.1	0.07	0.22	3.4	116	7.2	13.3	3480
	0.08	22.4	2.70	9.84	0.48	0.24	0.2	<0.1	0.08	0.15	2.0	140	23	11.6	3470
	0.08	21.0	2.73	8.77	0.42	0.19	0.1	0.1	0.07	0.23	43.4	118	24.9	11.4	3070
	0.07	19.3	2.91	9.17	0.50	0.15	0.1	<0.1	0.07	0.23	2.9	118	19	8.0	3440
B Schorl in the apex of chimneys above the perthite zone	0.03	19.2	3.01	4.48	1.68	<0.01	0.2	0.1	0.35	0.74	2.1	173	4.2	11.9	14,600
	0.03	18.9	3.06	5.19	1.50	<0.01	0.1	<0.1	0.31	0.67	2.5	153	1.4	8.8	14,100
	0.04	19.3	3.08	4.58	1.52	<0.01	0.1	<0.1	0.39	0.90	1.9	164	0.9	10.0	13,800
	0.05	18.1	2.93	9.30	0.67	0.04	0.1	<0.1	0.12	0.42	1.7	109	2.8	11.0	5190
	0.03	18.7	3.07	5.72	1.37	<0.01	0.1	<0.1	0.26	0.61	2.3	154	1.1	8.6	13,900
	0.07	17.6	3.00	9.65	0.35	0.51	0.1	<0.1	0.04	0.19	1.1	113	3.7	10.7	2160
Average A	0.07	18.9	2.94	9.35	0.45	0.27	—	—	0.06	0.20	7.0	116	7.3	8.6	3176
Average B	0.04	18.6	3.03	6.49	1.18	—	0.1	—	0.25	0.59	1.9	144	2.4	10.2	10,625

TABLE 17. CHEMISTRY OF MUSCOVITE FROM BOTH SIDES OF CHIMNEY 1

	Sample no.	Distance (cm)	Al (%)	Fe (%)	Mg (%)	Mn (%)	K (%)	P (%)	Ti (%)	B (ppm)	Ba (ppm)	Cs (ppm)	Ga (ppm)	Li (ppm)	Nb (ppm)	Rb (ppm)	Sr (ppm)	Sn (ppm)	Zn (ppm)
Right side of chimney	CMr-1	30	18.1	0.84	0.02	0.23	8.1	0.02	0.02	410	5.6	162	171	2110	147	4650	5.7	152	635
	CMr-2	61	18.6	1.18	0.02	0.21	8.4	<0.01	0.02	280	9.1	101	170	1710	206	4200	7.0	157	561
	CMr-3	122	18.7	1.16	0.02	0.14	8.4	0.03	0.03	240	3.5	66.6	168	1440	234	3430	5.2	122	367
	CMr-4	152	19.2	1.28	0.03	0.12	8.7	0.03	0.03	190	3.5	60.0	162	1650	229	2940	11.0	109	280
	CMr-5	183	18.7	1.22	0.03	0.13	9.0	<0.01	0.03	190	<0.5	57.9	155	1720	219	2760	<0.1	103	252
Left side of chimney	CMl-1	30	18.9	1.15	0.02	0.21		0.02	0.03	310	10.1	132	180	2660	192	4200	0.3	172	512
	CMl-2	91	18.8	1.31	0.01	0.20		<0.01	0.02	280	10.1	98.8	177	1670	210	3880	0.4	156	533
	CMl-3	122	19.2	1.32	0.01	0.17		0.01	0.02	260	12.9	77.7	178	1480	218	3630	1.1	139	453
	CMl-4	152	18.8	1.29	0.01	0.16		<0.01	0.02	240	11.6	67.3	173	1330	224	3420	<0.1	134	436
	CMl-5	183	19.1	1.18	0.02	0.13		<0.01	0.03	220	9.1	52.6	178	1390	210	2760	<0.1	111	287
	CMl-6	229	19.1	1.47	0.05	0.10		0.01	0.03	180	3.6	43.6	166	1220	200	2490	<0.1	96	271

Note: See also Figure 25. All analyses are elemental, not oxides. Distance column indicates distance above base.
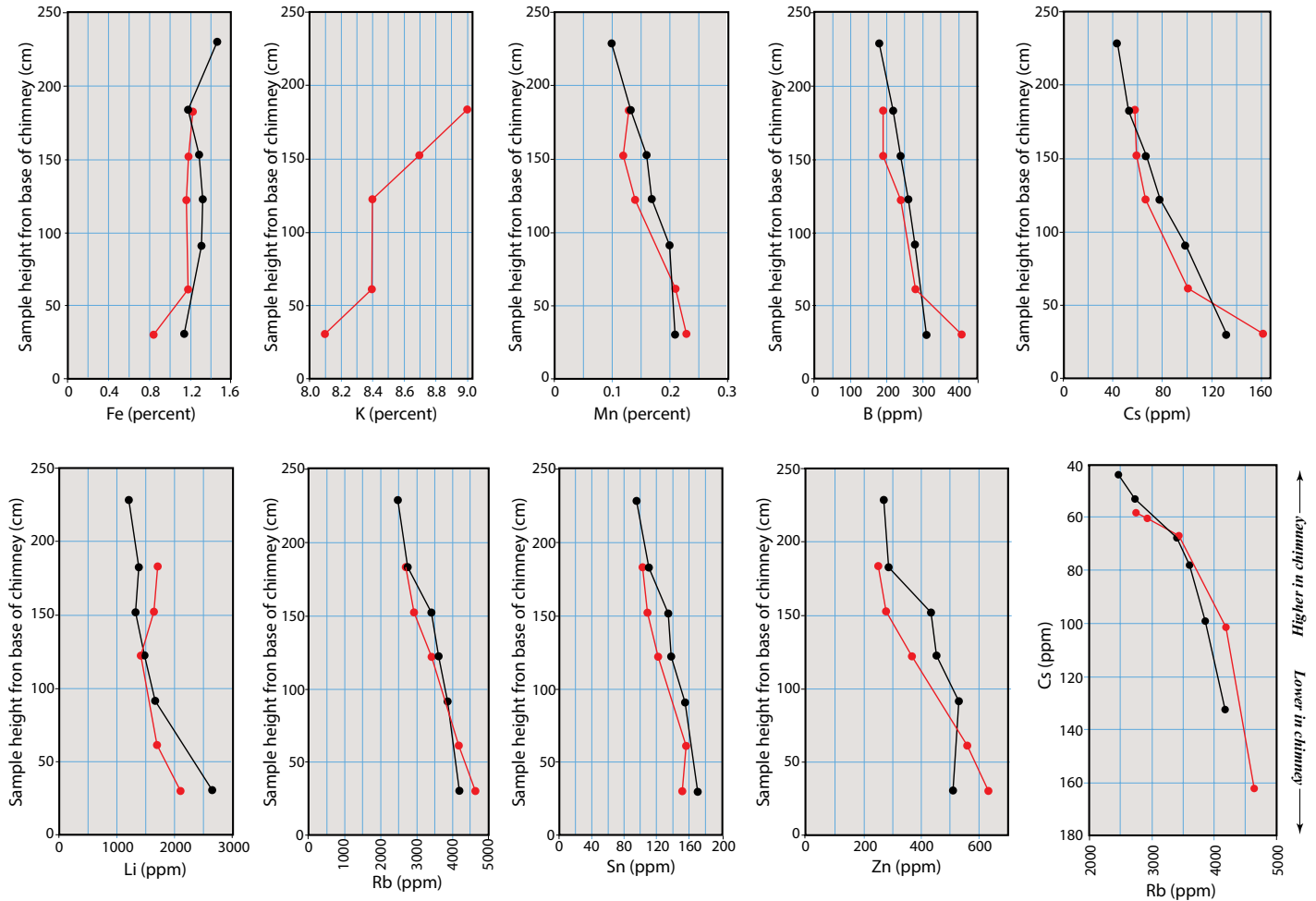
Figure 25. Muscovite composition from samples taken along both sides of chimney 1 (Figs. 20A and 20B), base to apex, with black curves for the left side of chimney and red curves for the right side. Lines connecting analyses are a visual aid for comparisons between elements and do not imply that analyses fall on the lines. Potassium analyses for the left side of the chimney were unavailable. All analyses are elemental, not oxides.
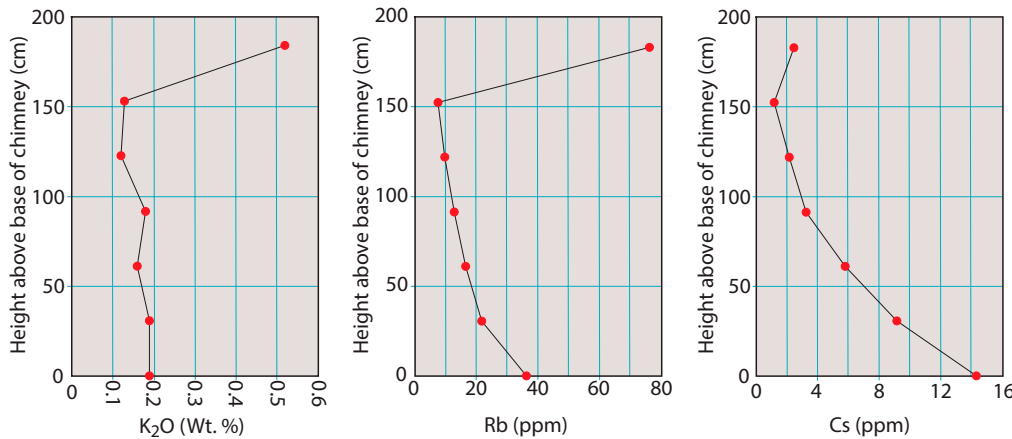

Figure 26. Albite composition from the base to apex of chimney 1. The prominent increase, especially in potassium and rubidium, at the apex is interpreted to reflect incomplete replacement of perthite. Lines connecting analyses are a visual aid for comparisons between elements and do not imply that analyses fall on the lines.

TABLE 18. PERCENT OF PERTHITE ZONE AUTOMETASOMATIZED

Site	Points counted	Percent metasomatized
1	98	44
2	98	51
3	98	55
4	98	47
5	98	57
6	116	62
7	126	52
8	132	49
9	132	67
10	140	49
11	197	58
12	206	47
13	211	34
14	216	78

Note: Calculations are based on point counts.
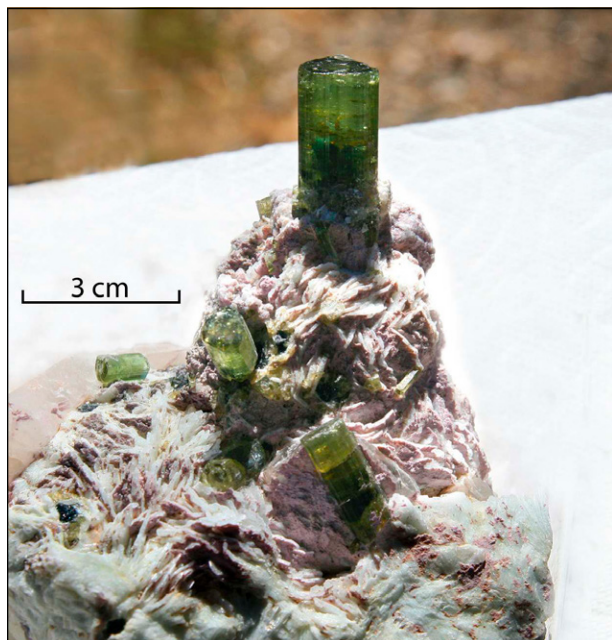
Figure 27. First-generation green elbaite with black inner base on cleavelandite mound from cavity in upper part of a chimney.

morganite. The highest pocket, 8 × 8 cm, contained green elbaite, some capped with blue elbaite.

Green elbaite crystals lining the cavity walls are color zoned, having a black-appearing basal interior rimmed by green elbaite and a green terminus (Fig. 28). The black-appearing core contains ~1.5% Zn, and the green elbaite contains ~0.2% Zn (Fig. 29). Chemical maps show an abrupt linear boundary between the relatively high-Zn, black-appearing crystal core of the zoned green elbaites (Fig. 29). These tourmaline prisms are dichroic. For light transmitted normal to the c axis, the black core appears red, and in a thin plate, for light transmitted parallel to the c axis, the black core is opaque, informally termed "closed c axis."

Unusual miarolitic cavity minerals include bismuthotantalite, bismuth-ostibiotantalite, stibiotantalite, and manganotantalite-manganocolumbite. Jahns et al. (1974) noted that every miarolitic cavity examined in the Stewart mine had experienced an explosive rupture that broke early-formed crystals lining the cavity wall. However, small cavities such as those in chimney 1 (Figs. 20A and 20B) appear to not have experienced an explosive rupture. In cavities exhibiting the more extreme explosions, the cavity wall is also fragmented, resulting in a breccia consisting of wall fragments intermixed with broken crystals and euhedral postrupture crystals.

Ruptured cavities contain two or three generations of elbaite and quartz. First-generation elbaite crystals are relatively stout and have an etched pinacoid termination (Fig. 30). Commonly, first-generation elbaite occurs at the crest of a lepidolite or albite mound. Some of these first-generation elbaite crystals have small, second-generation elbaite crystals attached on a termination or broken end. In the upper part of the larger miarolitic cavities, some broken first-generation elbaite crystals show

Figure 28. Cavity wall segment from cavity in upper part of a chimney, showing first-generation elbaite (larger, dark-green crystals), second-generation elbaite (A arrows), and second-generation quartz (B arrow). Orange material is hypogene montmorillonitic clay.

Figure 30. First-generation pink elbaite on lepidolite and cleavelandite base, from miarolitic cavity in lower part of a chimney in the perthite zone.
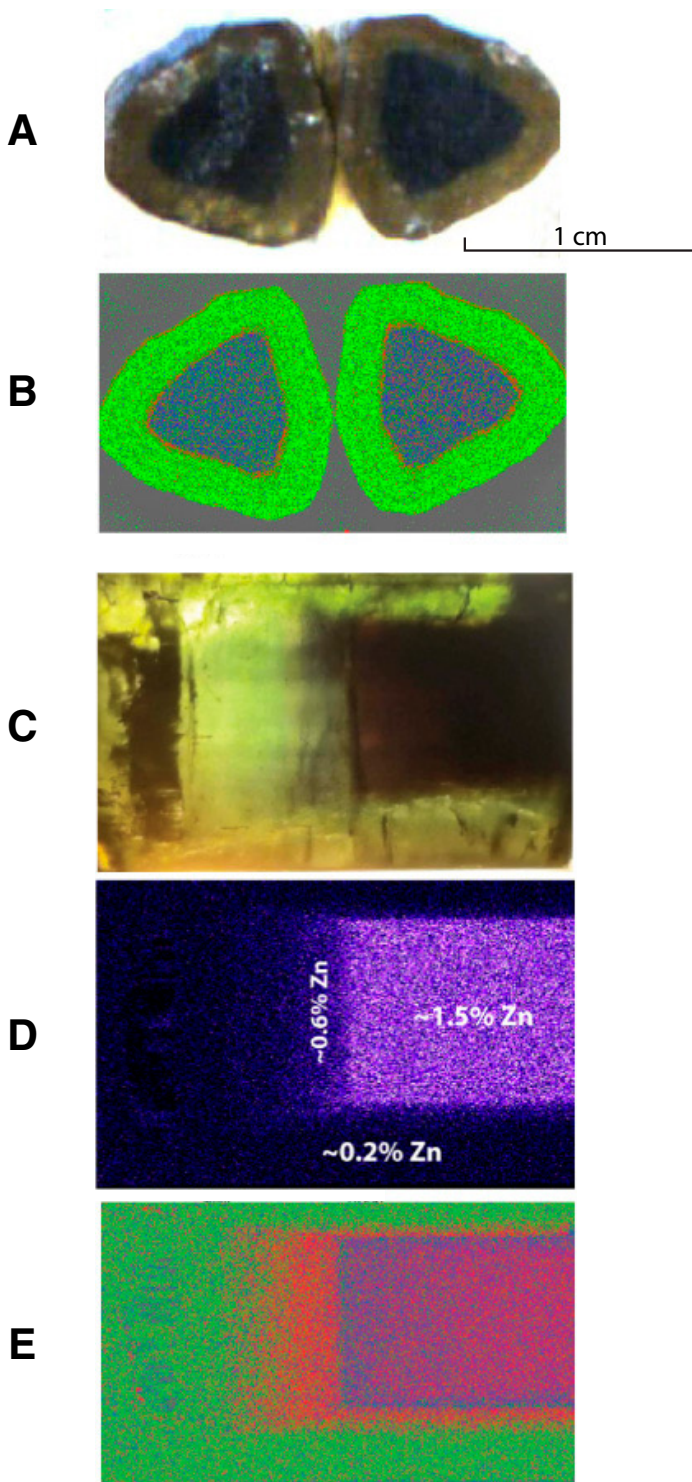
Figure 29. Chemical maps of green elbaite crystal that has a black base. (A) Normal-light photograph of the crystal. (B) Area inside the green border showing the high (~1.5%) Zn content of the core. (C) Back-lit normal-light photograph of the crystal showing the dark-colored high-Zn core. (D–E) False-color shading showing the areas of high zinc content. A and B are looking down the *c* crystallographic axis; C, D, and E are views normal to the *c* crystallographic axis.

the effects of having been tumbled and abraded. Postexplosive, second-generation elbaite crystals are thin hexagonal prisms (Fig. 28), and some have a sharp trigonal pyramid termination. Third-generation elbaite crystals are smaller thin prisms.

First- and second-generation pink elbaite samples from a cavity in the lower part of a chimney were analyzed for comparison (Table 19). Only slight differences appear between the two generations; Cs, Li, and Rb decrease in the second generation, and Sr and Bi increase.

First-, second-, and third-generation green elbaite samples from a cavity in the upper part of a chimney were analyzed for comparison (Table 19). First-generation crystals are color zoned and have an interior black base, a green outer part, and a green terminus similar to tourmaline in Figure 27. The black bases are high in Zn and Fe. Li and Sn show moderate increases, and Bi shows significant increases from first to third generation.

First-generation quartz crystals lining cavity walls commonly have a prism diameter of 15–30 cm, and they have typical alpha quartz morphology (Fig. 31A). In contrast, second-generation euhedral quartz crystals within the cavity interior are misshapen (e.g., Frondel, 1962). In many cases, the broken base of a first-generation quartz crystal is encrusted with second-generation quartz crystals (Fig. 31B). Typically, the misshapen second-generation quartz crystals have a maximum dimension of 1–3 cm (Fig. 32A), are euhedral, and have diminutive prism faces or lack prism faces. Some crystals have isometric (cubic)-, orthorhombic-, or monoclinic-appearing symmetry, and others are thin plates. The cubic-appearing quartz is a rhombohedral cube (Fig. 32B). Some first-generation quartz crystals have misshapen second-generation quartz randomly located on their faces (Fig. 33) or as sheet-like crystals enclosing the host first-generation crystal (Fig. 34). Other second-generation quartz has intergrown or attached second-generation elbaite (Figs. 35A and 35B).

Third-generation quartz crystals are diminutive, commonly have typical alpha quartz morphology (Fig. 36), and commonly occur as isolated single crystals or are attached to first- or second-generation quartz crystals (Fig. 37). Less common are aggregates of first-, second-, and third-generation quartz crystals (Fig. 38).

The changes in crystal morphology from the first generation, having typical alpha quartz crystals lining cavity walls, to second-generation misshapen crystals and then diminutive third-generation alpha quartz morphology clearly reflect radical changes in the growth environment.

TABLE 19. SELECTED ELEMENT CHEMISTRY OF FIRST-, SECOND-, AND THIRD-GENERATION ELBAITES

	Ti (%)	B (%)	Fe (%)	Mn (%)	Mg (%)	Ca (%)	K (%)	Li (%)	Cs (ppm)	Ga (ppm)	Rb (ppm)	Sr (ppm)	Bi (ppm)	Sn (ppm)	Zn (ppm)
First-generation pink elbaite	<0.01	3.12	0.02	0.53	0.01	0.01	<0.01	0.75	1.6	125	1.6	4.9	20.4	3	46
	<0.01	3.00	0.01	0.08	0.02	<0.01	<0.01	0.75	1.8	104	3.0	4.2	6.4	2	24
	<0.01	3.02	<0.01	0.12	0.01	<0.01	<0.01	0.71	0.6	250	0.4	4.1	4.5	6	<5
	<0.01	2.92	0.01	0.08	0.02	<0.01	<0.01	0.73	1.1	226	1.2	4.2	19.1	6	16
Second-generation pink elbaite	<0.01	2.25	0.02	0.25	0.04	<0.01	<0.01	0.61	0.08	159	1.6	7.0	44.7	11	23
	<0.01	2.73	0.01	0.72	0.04	<0.01	<0.01	0.72	0.03	188	0.9	4.1	38.9	15	64
	<0.01	1.91	1.00	0.31	0.06	0.01	<0.01	0.52	0.04	141	2.3	6.5	53.0	9	30
	<0.01	2.49	0.01	0.08	0.05	0.03	<0.01	0.74	1.6	167	0.6	6.9	193	8	<5
First-generation green elbaite—basal core	0.02	2.61	2.95	1.66	0.02	<.1	<.1	0.38	3.3	158	21.2	6.0	1.6	24	11,299
	0.02	2.90	4.12	1.64	0.01	<.1	<.1	0.40	2.7	146	5.1	4.8	4.1	22	12,298
First-generation green elbaite—terminal	0.02	2.36	0.61	1.32	0.04	0.1	<.1	0.55	0.4	211	0.7	3.2	36.1	27	697
	0.02	2.48	0.66	1.45	0.03	0.1	<.1	0.58	0.4	211	3.1	4.1	58.2	31	720
Second-generation green elbaite	0.02	2.49	1.01	1.58	0.04	0.3	<.1	0.64	0.5	187	2.8	4.6	162	32	1353
	0.01	1.81	0.74	0.80	0.06	0.1	<.1	0.48	0.3	148	0.7	6.2	103	28	358
Third-generation green elbaite	0.03	3.07	0.88	2.17	<0.01	0.2	<.1	0.78	0.5	207	3.1	5.1	173	42	932
	0.03	3.05	0.86	2.16	<0.01	0.2	<.1	0.77	0.3	201	2.3	18.7	180	41	903

Note: Elbaites were collected from miarolitic cavities in chimneys.
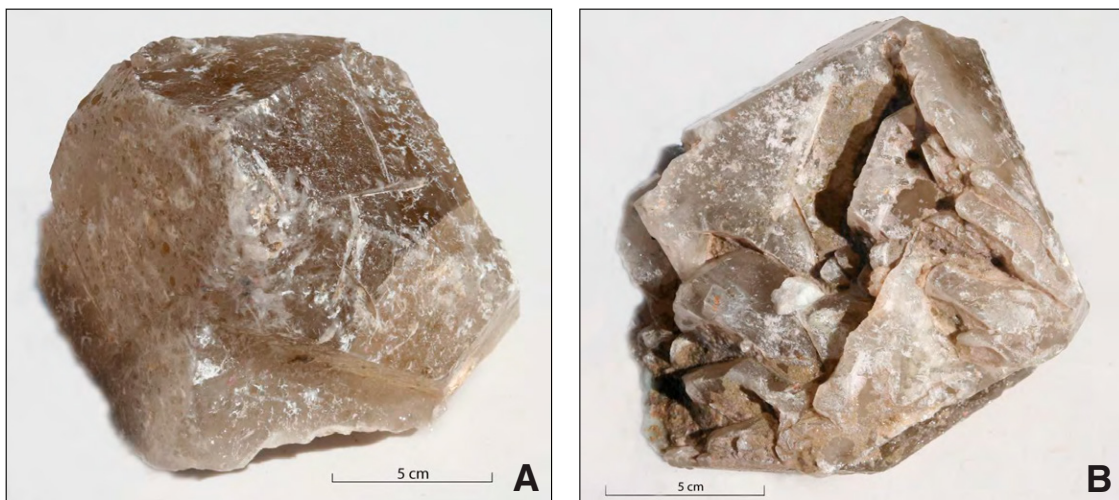
Figure 31. (A) Termination of broken first-generation quartz. (B) Broken end of crystal in part A "healed" by second-generation quartz. Quartz is from a miarolitic cavity in the lower part of a chimney in the perthite zone.
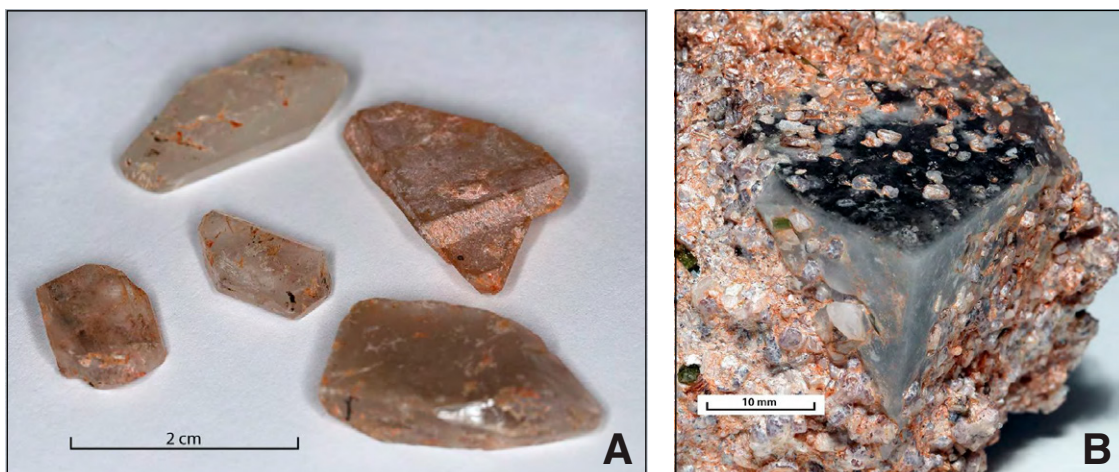
Figure 32. (A) Second-generation misshapen quartz crystals. (B) Single rhombohedral cubic quartz crystal with numerous third-generation quartz and third-generation elbaite. Rhombohedral cubic quartz crystal shows parts of three large faces and parts of two small faces. Samples were collected from a miarolitic cavity in the upper part of a chimney in the perthite zone.

Figure 33. Small second-generation quartz showing anomalous crystal morphology attached to a large first-generation quartz crystal, from miarolitic cavity in the lower part of a chimney in the perthite zone.

Figure 34. Sheet-like second-generation quartz on termination of first-generation quartz, from miarolitic cavity lower part of a chimney in the perthite zone.
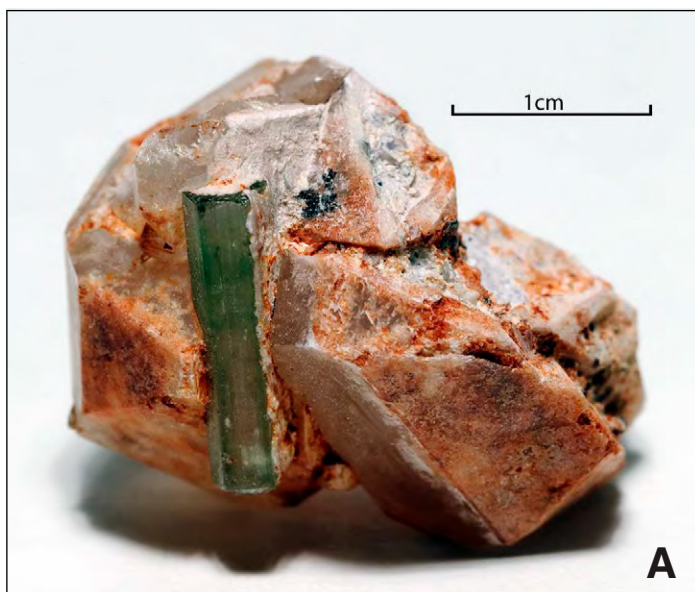
Figure 35. (A–B) Second-generation quartz and second-generation elbaite, both from a miarolitic cavity in the upper part of a chimney in the perthite zone.

Figure 36. Third-generation quartz and third-generation elbaite, from a miarolitic cavity in the upper part of a chimney in the perthite zone.

Figure 37. Tabular second-generation quartz and attached cluster of third-generation quartz, from miarolitic cavity in upper part of a chimney in the perthite zone.
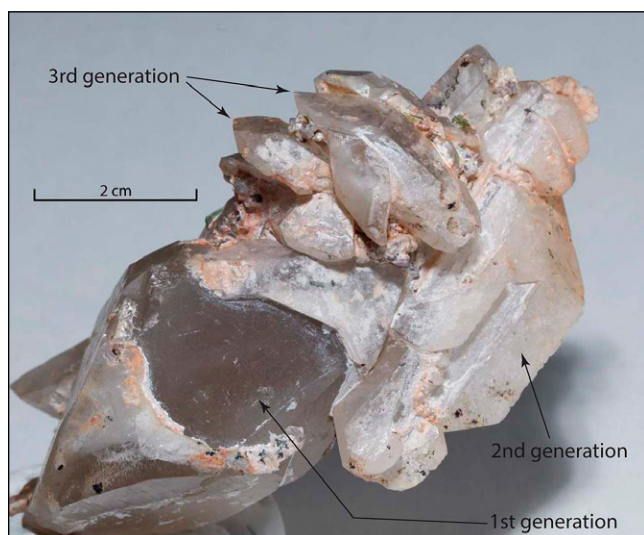
Figure 38. Group of first-, second-, and third-generation quartz, from a miarolitic cavity in the upper part of a chimney in the perthite zone.

Upper Intermediate Zone

Where the core zone is lepidolite, the core zone transitions into the upper intermediate zone. Where the core zone is lepidolite-spodumene-petalite-amblygonite, the overlying perthite zone transitions upward into the upper intermediate zone. The upper intermediate zone is a thick section of mixed quartz-perthite-schorl-muscovite rock that contains both planar and lenticular discontinuous pegmatitic layers (Figs. 39A and 39B). This zone correlates with Jahns and Wright's (1951, their Plate 4) "graphic granite; medium- to coarse-grained perthite-quartz pegmatite, with minor albite and muscovite" and includes "numerous fracture-filling units of quartz, albite, muscovite, lepidolite, and tourmaline, parallel to walls of graphic-granite unit."

Open cuts in the southern part of the Stewart mine expose a complex section of the upper intermediate zone (Figs. 39A and 39B). Some pegmatite of the layered part of the upper intermediate zone interfingers with the upper part of the perthite zone. In places, the lower layers of the upper intermediate zone contain lenses of lepidolite (Fig. 40). Layering is regular and planar in parts of the zone. These more regular and planar layers are 15–50 cm thick. Some layers are distinctly different in composition from adjacent layers, whereas others have similar mineralogy but differ in grain size. The most noticeable features are layers containing abundant schorl crystals oriented at high angles to the layer boundary (Fig. 41). Some similar schorl-rich layers occur in the upper part of the perthite zone.

Hanging-Wall Zone

The ~2-m-thick graphitic granite hanging-wall zone of the dike includes both typical platy habit muscovite, mostly 0.25–0.75 cm in diameter, and conical-shaped radiating clusters of composite muscovite blades (Fig. 42). Most clusters are 5–20 cm in length. The muscovite clusters are sparse to absent in the upper 10 cm of the zone and are common below 10 cm. Most of the individual muscovite "blades" in the conical-shaped clusters enlarge in width toward the terminal end of the cluster. Radiating crystals that appear to be individual crystals are composite structures consisting of numerous smaller crystals. In some clusters, biotite is interleaved with the muscovite. Extremely small prisms of elbaite occur within the radiating muscovite crystals.

The upper 76 cm section of the hanging wall was sampled at 25 cm intervals. The chemistry is given in Table 20. Although only three samples were analyzed, they appear to show relatively little change in chemistry through the upper part of the hanging-wall zone. Silica, iron, and the alkalis show relatively little variation, suggesting there was no substantial chemical exchange from the host gabbro. However, visible alteration effects of the gabbro at and near the dike contact, and the graphs shown in Figure 5 indicate that fluids forming the hanging-wall zone did have a chemical influence on the gabbro.

INTERPRETATIONS

LCT Pegmatite Family

The Stewart pegmatite-aplite conforms to LCT pegmatites, which contain spodumene, petalite, lepidolite, elbaite, and multiple primary phosphates (Cerny et al., 2012). Cerny et al. (2012, p. 291) stated, "The main characteristics of the LCT pegmatites, however, are derived from previously unmelted, mica-rich metamorphic rocks, irrespective of the tectonic regime in which their initial partial melting occurs." Martin and De Vito (2005) interpreted phosphorus- and Cs-rich lithium pegmatites to be diagnostic of S-type sources for the LCT pegmatite family. The average Sr_i of 0.7039 of the western part of the batholith and the 0.7042 Sr_i of the Stewart pegmatite-aplite preclude an origin from melting of prebatholithic metamorphic rocks.
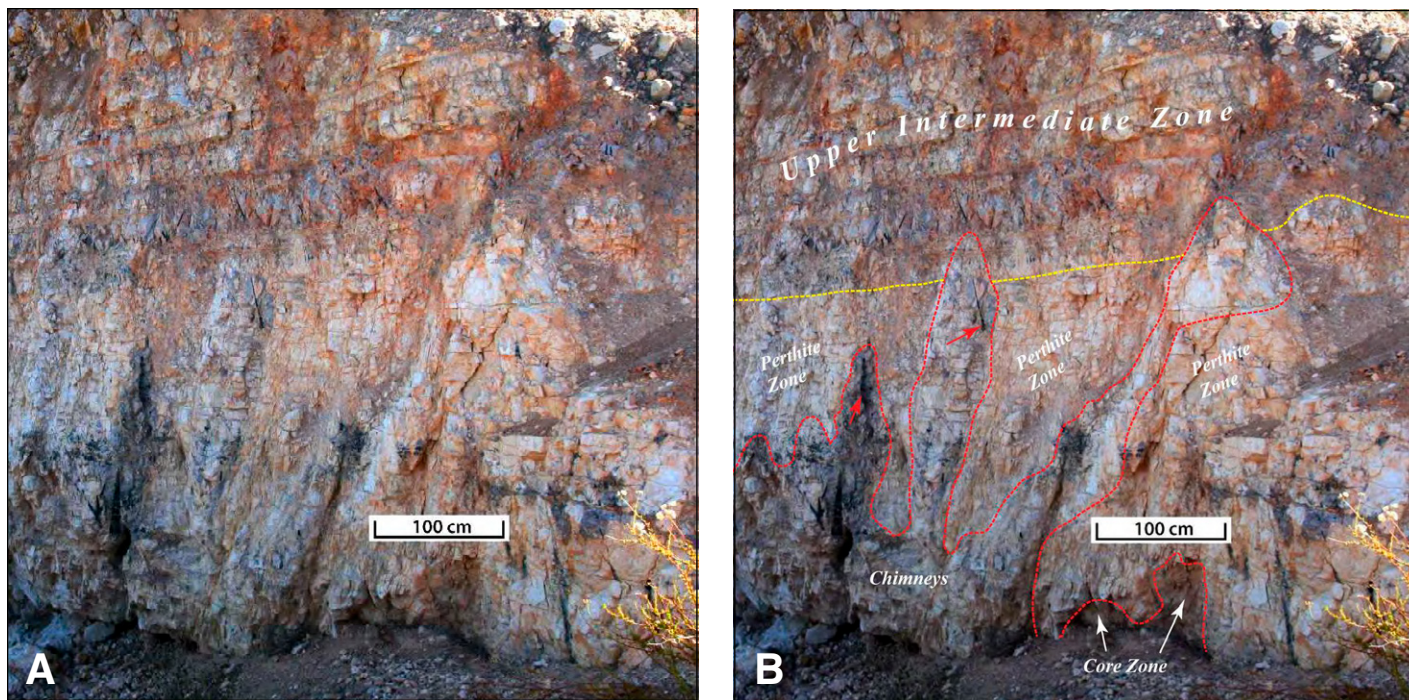
Figure 39. (A) Layered upper intermediate zone overlying perthite zone, showing some chimneys that penetrate the lower part of the upper intermediate zone. **(B)** Same as A, but showing labels and rough outlines of zones and chimneys. Red arrows point to long schorl crystals at the apex of chimneys. Note schorl crystals are oriented at high angles to the layering.
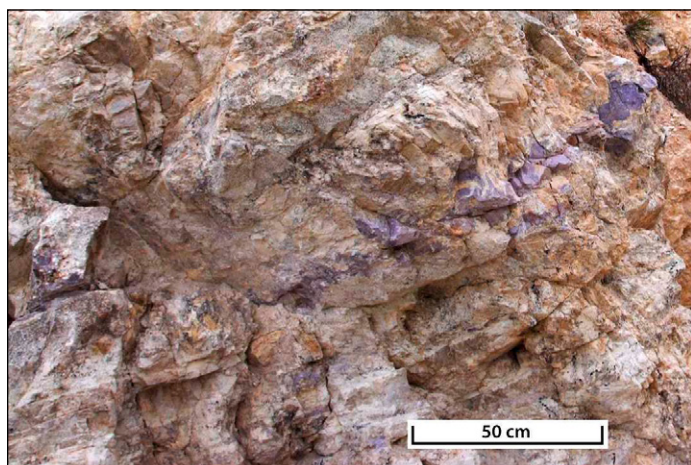

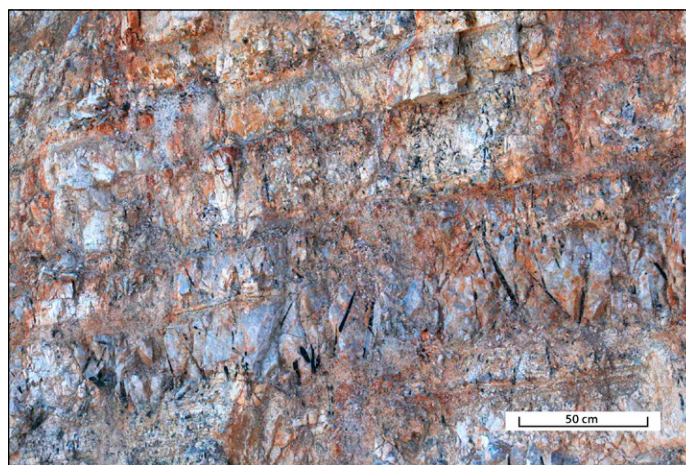**Figure 40. Discontinuous lepidolite lens in the upper intermediate zone.**

Figure 41. Layered upper intermediate zone; schorl is oriented at high angles to the layering.

TABLE 20. WHOLE-ROCK CHEMISTRY OF THE HANGING-WALL ZONE

	Distance (cm)	SiO$_2$ (%)	TiO$_2$ (%)	Al$_2$O$_3$ (%)	MgO (%)	Fe$_2$O$_3$ (%)	MnO (%)	CaO (%)	Na$_2$O (%)	K$_2$O (%)	P$_2$O$_5$ (%)	LOI (%)	Sum (%)	F (ppm)	B (ppm)	Ba (ppm)	Li (ppm)	Sr (ppm)	Zn (ppm)
HW-1	0–25	79.3	0.01	12.9	0.01	0.26	<0.01	0.97	5.50	0.68	0.05	0.55	100.23	194	<10	56.6	46	37.8	10
HW-2	26–51	77.0	0.02	14.2	0.11	0.79	0.14	0.63	4.73	1.62	0.05	1.02	100.31	284	<10	17.6	68	14.8	27
HW-3	52–76	78.3	0.01	14.1	0.03	0.43	0.10	0.50	5.84	1.22	0.07	0.60	101.20	217	<10	10.2	51	10.5	27

Note: Boron is essentially not present. LOI—loss on ignition. Distance column indicates distance from base.

Figure 42. Sample of hanging-wall zone showing plumose muscovite aggregates. The radial composite blades include minor biotite.

Pegmatite-Forming Fluid: Cogenetic or Allogenic

Despite the recognition by a number of workers that the Pala district pegmatites were exclusively restricted to Pala gabbro/mafic tonalite, all interpretations of the source of the pegmatite-forming fluid(s) concluded that the fluid(s) were allogenic, derived from some designated or undesignated granitic body. These interpretations are rooted in the belief that the pegmatites represent very late NPRB igneous activity, and therefore they are related to what were thought to be the youngest intrusions. This was first stated and reiterated by Larsen (1948, 1951, 1954), who considered the sequence of emplacement of the batholith to be based on the extent of evolution of the magmas, or essentially their silica and mafic content. He clearly expressed that, "The gabbros were intruded first, then the tonalites, then the granodiorites, and finally granites. This is the succession commonly found in batholiths" (Larsen, 1948, p. 137). Larsen's sequence of lithology emplacement has been invoked for over 60 yr (e.g., Jahns and Wright, 1951; Jahns, 1979; Shigley and Brown, 1985; Snee and Foord, 1991; Webber et al., 1999; Patterson, 2009). Jahns (1979, p. 6) reiterated "the pegmatites…represent the youngest igneous activity within the batholith complex …." Shigley and Brown (1985, p. 404) concurred: "The granitic pegmatites around Pala crystallized from residual, highly-differentiated magmas left over following the consolidation of the Peninsular Ranges batholith."

Zircon U/Pb ages for the nongabbroic part of the batholith have a range of ages from 126 to 91 Ma (Premo et al., 2014), implying at least a 35 m.y. age difference from gabbro to pegmatite emplacement. Extensive isotopic dating of Peninsular Ranges batholith plutons since the 1970s has well established the sequential west-to-east emplacement history of the batholith (e.g., Armstrong and Suppe, 1973; Silver and Chappell, 1988; Todd et al., 2003; Ortega-Rivera, 2003; Premo et al., 2014) and that gabbro and granite, at numerous localities, were being emplaced at essentially the same time. Kimbrough's U-Pb dating of zircons from gabbro plutons in the NPRB makes it incontrovertible that many granite and granodiorite plutons are significantly older than gabbros that were emplaced even a short distance from them (Kimbrough et al., 2015). The oldest high-silica granitic rocks in the NPRB are in the western zone (Morton et al., 2014a).

The isotopically established sequence of pluton emplacement, showing that gabbro is not the oldest batholithic rock, exacerbates the problem that there is an absence of a nearby suitable source for pegmatite-forming

fluid. Jahns and Wright (1951, p. 44) noted that: ".... the Pala pegmatites do not appear to be closely related either in time or in space, to any nearby igneous rocks now exposed." Later, Snee and Foord (1991, p. 139) reiterated the dilemma, stating, "Within the western portion of the Peninsular Ranges batholith, complex granitic pegmatites such as those in the Pala, Ramona, and Mesa Grande districts are known to be the youngest rocks of the batholith. No direct source for the pegmatites has been located…."

Taylor et al. (1979) suggested that a parent granodiorite, derived by melting sediments that included marine clays, could provide a source for the lithium and boron, and they noted that there are several large granodiorite plutons west of the Pala gabbro. However, these granodiorite plutons are ruled out as a source of the pegmatite-forming fluids because they are older than the Pala gabbro and its included pegmatites (Snee and Foord, 1991; Morton et al., 2014a).

The most recent petrogenetic interpretation of the Stewart dike concluded it is a composite body consisting of 22 zones formed from at least 10 magmatic pulses (Patterson, 2009, p. 339). Patterson interpreted that the magmatic pulses were derived from a granodiorite body located 10 km northwest of the Pala gabbro-tonalite (Patterson, 2009, p. 339). Based on a hornblende $^{40}Ar/^{39}Ar$ age of 113 Ma (Snee and Foord, 1991), this granodiorite body is at least 10 m.y. older than the Pala gabbro, making it an impossible source of the Stewart pegmatite-aplite.

Recent modeling of the cooling history of the Stewart dike used a 20 m.y. age difference between emplacement of gabbro and the dike. The assumed temperature of gabbro at the time of pegmatite emplacement was 150 °C (Webber et al., 1999), a temperature difference of 580–550 °C from the 730–700 °C temperature that has been the proposed for the pegmatite-forming fluid (Taylor et al., 1979). This temperature difference should have produced a quench fabric for both the footwall and hanging wall of the dike.

Based on the Pala gabbro composition, we estimate that its crystallization temperature was near 1075 °C (Huang and Wyllie, 1986). Muscovite from an intermediate zone of the dike has an $^{40}Ar/^{39}Ar$ age of 100.4 Ma, and lepidolite from the core zone is 99.3 Ma (L.W. Snee, 2009, personal commun.). This is essentially the same as the 99.4 Ma $^{40}Ar/^{39}Ar$ age of muscovite from the Pala Chief pegmatite, located 1.2 km northeast of the Stewart mine (Snee and Foord, 1991). The argon closure temperature for muscovite is ~350 °C (McDougall, and Harrison, 1999). Within the precision of the two isotopic dating systems, the Pala gabbro-tonalite pluton and the Stewart pegmatite-aplite are essentially contemporaneous. Cooling from 1075 °C to 350 °C, therefore, may have taken no more 1 m.y., resulting in an averaged cooling rate 700 °C/m.y. Crystallization itself likely took place within much shorter time scales.

Foord and Shigley (1991, p. 130) stated, "More recent studies suggest that the pegmatites are related to the emplacement of the younger La Posta–type plutons in the central and eastern portions of the PRB (98–89 Ma) [Walawender et al., 1990]." The nearest La Posta–type pluton to the Stewart dike is the Coahuila Valley pluton, 25 km east of the Pala gabbro. Other La Posta–type plutons are located 45–55 km from Pala. At present erosion levels, there is no evidence for a path by which material from the Coahuila Valley pluton could have reached the location of the Stewart dike. The Coahuila Valley pluton (Sharp, 1967; Morton et al., 2014a) has Li-bearing pegmatite dikes within the pluton (e.g., Anita mine), greisen-like pegmatitic masses at and/or near the roof of the pluton (e.g., French Pete mine), and dikes that extend a short distance into adjacent metamorphic rock (e.g., Cyro-Genie mine).

Tonalite of the Coahuila Valley pluton has zircon U-Pb ages of 96.5, 95.5, and 92.6 Ma and a biotite $^{40}Ar/^{39}Ar$ age of 91.9 Ma (Morton et al., 2014a) postdating the $^{40}Ar/^{39}Ar$ age of 100.4 Ma from muscovite of the Stewart dike. The age of the Stewart dike therefore predates the 98–89 Ma

age range of the La Posta–type plutons (Foord and Shigley, 1991). The Sr_i of the Coahuila Valley pluton is 0.7051–0.7055, considerably greater than the 0.7042 of the Stewart dike. La Posta–type plutons are therefore ruled out as having any relationship with the Stewart dike on the basis of their age, Sr_i, and distance/location.

In conclusion, the regional geologic setting and field, chemical, and isotopic data collectively indicate that the Stewart dike pegmatite-aplite–forming fluid was not allogenic, but cogenetic. This conclusion is consistent with the observation that all major complex REE and Li pegmatite districts in the NPRB are located within gabbro and/or mafic tonalite plutons with similar initial Sr compositions, ranging from 0.7036 to 0.7057.

Single or Multiple Pegmatite-Forming Fluids

Most previous descriptions interpreted, or assumed, the dike formed from a single fluid (e.g., Taylor et al., 1979). Based on the repetition of lithologic units in a quarry wall, Jahns and Wright (1951, p. 29) interpreted the Stewart pegmatite-aplite to be a composite dike, because "a layer of graphic granite 5 to 9 feet thick is overlain by a 5-foot zone of massive quartz with giant euhedral perthite crystals. It is underlain by a very thick zone rich in coarse blocky perthite and this unit in turn is underlain by rock similar to that overlying the graphic granite." Their interpretation does not appear to require two separate influxes of pegmatite-forming fluid. Taylor et al. (1979, p. 203), based on chemical and isotopic data for gem-bearing pegmatite-aplite dikes in San Diego County, including the Stewart dike, concluded, "Subsequent to solidification of the pegmatite along the upper contact, the dikes behaved grossly as chemically and isotopically closed systems." We have not found any evidence for multiple allogenic fluid emplacements. In contrast, Patterson (2009, p. 339) interpreted the dike to have formed from at least 10 separate pegmatite magmatic pulses "... with time delays ranging from weeks to years."

There appears to be no evidence that the Stewart dike resulted from more than a single pegmatite-forming fluid. Lithologic variation within the dike is consistent with the Jahns-Burnham model (Jahns and Burnham, 1969; Jahns, 1982). Mineralogic variation within the dike is best explained by differentiation, mineral segregation, distribution and concentration of volatiles, and autometasomatism of a single pegmatite-forming fluid in an essentially closed system.

Origin and Emplacement of the Pegmatite-Forming Fluids

The NPRB was formed by subduction of oceanic crust, transitioning from beneath thin oceanic crust to beneath thick continental crust (Morton et al., 2014a). Systematic and sequentially increasing Sr_i values in the western zone, western transition zone, eastern transition zone, and then eastern zone reflect subduction beneath progressively more continental crust eastward.

Seafloor basalts and serpentinites of both seafloor spreading and subduction zones have been shown to contain significant amounts of boron and lithium (e.g., Agranier et al., 2007; Benton et al., 2001; Chan, et al., 1992; Lee et al., 2008; Li and Lee, 2006; London, 2008; Noll et al., 1996). The average Sr_i of 0.7039 for the western zone of the NPRB is consistent with a juvenile origin or an origin of metasomatic fluids from altered oceanic crust. The Sr_i of 0.7036–0.7037 of the Pala gabbro is similarly consistent with such an origin.

The shallow depth of gabbro emplacement led to relatively rapid crystallization of gabbro, too fast to allow for significant crystal-liquid segregation and generation of intermediate derivative magmas. The rapid cooling and crystallization may have only allowed for an extremely late-stage fluid, that is, an aqueous and highly mobile incompatible-element–enriched

pegmatite-forming fluid, to escape and eventually be congregated into dike-like bodies. A similar scenario was suggested by Lee and Morton (2015) and Farner and Lee (2017 to explain the enigmatic observation that highly silicic magma bodies are found in the more mafic parts of the batholith and are actually poorly represented in more felsic batholiths.

Pegmatite-forming fluids likely crystallized at ~690–680 °C (Taylor et al., 1979). During the time between cooling from 1075 °C to 690–680 °C, initial differentiation of the pegmatite-forming fluid resulted in fluxing of incompatible elements upward from the footwall into the core zone and above. We speculate that loss of these highly incompatible elements from the basal part of the pegmatite-forming fluids may have raised the solidus temperature of the pegmatite-forming fluid in the footwall zone, causing rapid "quench-like" crystallization to generate the aplitic texture characteristic of the basal footwall zone. In the medial and upper part of the footwall zone, the passage of incompatible elements and components may have served as a fluxing agent, coarsening the grain size from aplite to fine- to coarse-grained granite. Crystallization of the dike progressed upward from the footwall zone and downward from the hanging wall. Above the footwall zone, upward transport of incompatible elements and fluids produced the lower intermediate zone, resulting in typical pegmatite-textured granite, including large schorl crystals.

The hanging wall of the dike crystallized when the temperature of the gabbro equaled the solidus temperature of the hanging-wall pegmatite-forming fluid. Based on the isotopic data of Taylor et al. (1979), this temperature is taken as ~690–680 °C. Crystallization progressed downward from the hanging wall, with further concentration of fluids and incompatible elements facilitating the growth of the giant crystals of the upper intermediate zone. Moving upward from the core zone, potassium-rich fluids formed the perthite zone. The progressive upward movement of potassium-rich fluids from the core zone to the perthite zone enriched the core zone fluid in sodium. Crystallization of mainly anhydrous phases of the lower and upper intermediate zones and perthite zone progressively increased the fluxing ability of the core zone fluid.

Abundant lepidolite and elbaite crystallized in the lower part of the core zone, followed by crystallization of spodumene. Most of the spodumene was autometasomatized by residual fluids, followed by crystallization of intergrown petalite and heulandite. Above the petalite-heulandite rock, Li-charged fluids formed large masses of amblygonite, the outer parts of which were autometasomatized to a mixture of secondary phosphates. Higher yet in the core zone, lithiophilite crystals formed, and these were in turn partly to completely altered to a variety of secondary phosphates and Fe-Mn oxides.

Sodium-rich fluids escaping the core zone replaced perthite and formed autometasomatic chimneys. Schorl crystals, essentially restricted to the apices of the chimneys, reflect the upward concentration of the fluxing elements boron and fluorine. Potassium-rich fluids liberated from the perthite zone by the formation of the albite chimneys autometasomatized overlying elbaite to a mixture of potassium-rich clay and zeolites.

The upward movement of sodium-rich fluids into the perthite zone resulted in a dynamic setting within the core zone. Local pressure reduction produced some aplitic-textured rock, and flowage within sodium-rich fluid produced flow-textured albitic rock. A progression from flow-textured to protoclastic and cataclastic albitic rock indicates that deformation was active when the core zone was crystallizing and persisted after crystallization. Removal of the sodic-rich fluids from the core zone reduced the volume of the zone and produced cataclastic-textured rock in earlier-formed parts of the core zone, followed by formation of numerous low-angle faults.

In the chimneys, the concentration of gaseous fluids rich in boron, fluorine, and lithium formed miarolitic cavities in the cores of albite chimneys.
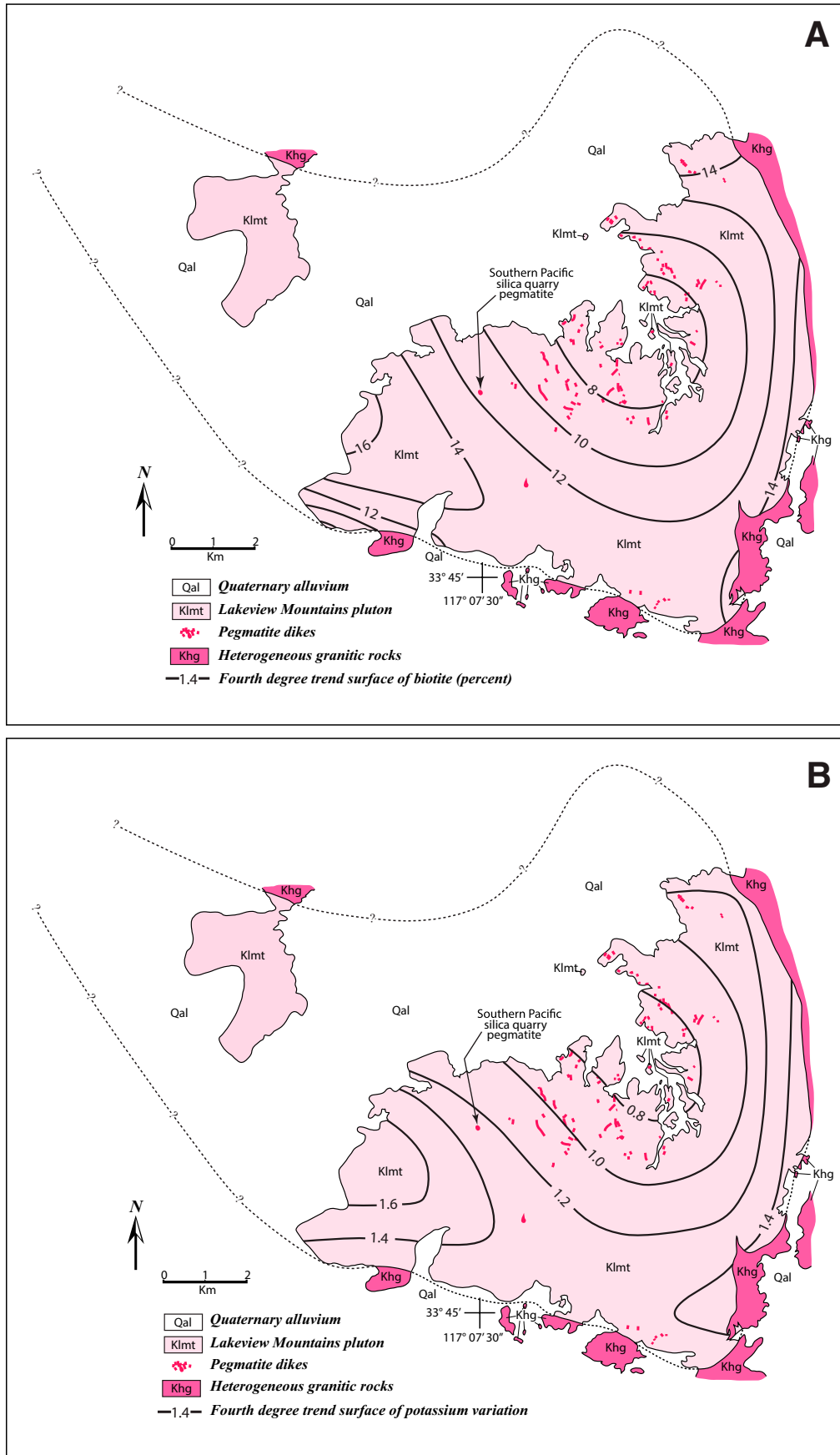
Figure 43. Generalized geologic maps of the Lakeview Mountains tonalite pluton showing distribution of pegmatite dikes (after Morton et al., 2014b). (A) Variation in biotite content. (B) Variation in potassium concentration. Tonalite is devoid of K-feldspar. Almost identical contours for potassium and biotite indicate that essentially all potassium in the rock is contained in the biotite.

The subsequent crystallization of mainly anhydrous phases, i.e., quartz, K-feldspars, albite, and elbaite, led to a pressure increase that exceeded the confining pressure and ruptured the cavities. Release of pressure resulted in rapid crystallization of second-generation elbaite and quartz within the core of the cavity. Second-generation euhedral quartz crystals are misshapen, and elbaite formed thin, hexagonal prismatic crystals (e.g., Fig; 28; compare thin second-generation tourmaline crystals, labeled A, with the unlabeled stout first-generation tourmaline). Broken second-generation elbaite attached to second-generation quartz indicates a continuation of a dynamic setting, but less violent than the cavity rupturing. Crystallization in an easing dynamic setting produced third-generation quartz and elbaite. Crystallization ceased with zeolites and clays.

Regional Implications

The common position of all major pegmatite districts in the NPRB—occurring within low-Sr_i gabbro and/or mafic tonalite plutons—strongly suggests a genetic relationship between the host plutons and their included pegmatites. Satisfactory isotopic data are lacking for ages of host gabbro/tonalite and pegmatites for most of the pegmatite districts. However, one district, the Lakeview district, 50 km north of the Stewart pegmatite-aplite (Fig. 3), does have adequate isotopic data (Morton et al., 2014a).

The Lakeview pegmatites are within the Lakeview Mountains pluton, a mafic biotite-hornblende tonalite that is devoid of K-feldspar. Complex REE-bearing pegmatites are concentrated in the low-potassium, late-crystallizing core of the pluton (Fig. 43). Like the Pala gabbro, there are no intermediate compositions between the tonalite and pegmatites.

A 9-cm-thick pegmatite has a diffuse, gradational boundary between the pegmatite and the host tonalite. In this pegmatite, biotite crystals growing inward from the contact of the dike are 4 cm in length (Fig. 44). The 4 cm size of biotite at the dike margin is interpreted to indicate that the temperature of the tonalite was essentially the same as that of the pegmatite-forming fluid at the time the pegmatite crystallized.

The age of the pegmatites and the age of the host tonalite are the same. The zircon U/Pb age of the tonalite from the outer, early crystallized part of the pluton is 100.2 Ma, the medial part has ages of 97.4 Ma and 100.6 Ma, and core of the pluton is 99.3 Ma. Monazite from the intermediate zone of the Southern Pacific silica quarry pegmatite (Fig. 43), which is one of the larger pegmatites in the pluton, has a $^{207}Pb/^{235}U$ age of 99.6 Ma (Morton et al., 2014a).

Initial strontium values for 96 systematically collected composite tonalite samples have an average Sr_i of 0.70485 (Fig. 45). Initial strontium values for the Southern Pacific silica quarry pegmatite and a pegmatite in the core of the pluton are the same, 0.7049. Based on the temporal tonalite-pegmatite equivalency and equivalent Sr_i values of the tonalite and pegmatites, the Lakeview pegmatites are interpreted as being cogenetic.

Based on isotopic data from the Pala gabbro and Stewart pegmatite-aplite and the Lakeview Mountains tonalite and its included pegmatites, we interpret the pegmatite bodies to be cogenetic with their respective host plutons, and we conclude they are the products of late-crystallizing pegmatite-forming fluids derived from their respective mafic host rocks.

CONCLUSIONS

The age of the Stewart pegmatite, 100.4 Ma (muscovite $^{40}Ar/^{39}Ar$), and host gabbro, 103 Ma (zircon U/Pb), is essentially the same, and initial Sr_i values for the host gabbro, 0.7036–7, and the Stewart pegmatite, 0.7042, are similar. The low 0.7042 Sr_i precludes ancient metasediments as the source of the pegmatite melt. The similarity of Sr_i values supports the interpretation that the host gabbro and the Stewart pegmatite are cogenetic.

Figure 44. A 9-cm-thick pegmatite containing 4 cm biotite crystals from central part of the Lakeview Mountains pluton. Coarse grain size extends to the border of the dike; no chill effects are apparent.
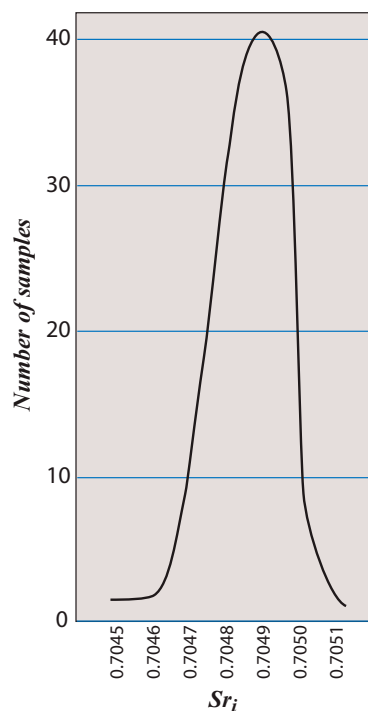

Figure 45. Variation of Sri in Lakeview Mountains pluton.

Although all previous interpretations concluded the dike is allogenic, all interpreted/suggested sources for the dike-forming melt have been ruled out on the basis of age, initial Sr_i values, or distance (>20 km) between the Stewart dike and the potential granitic source. Based on available data, the Stewart pegmatite-aplite is interpreted as cogenetic with the host gabbro.

The structural, textural, and mineralogic variation, including metasomatism, within the Stewart pegmatite-aplite is compatible with the evolution of an initial single melt in an essentially closed system. Upward movement of fluxing elements resulted in the formation of a fine- to medium grained footwall. Concentration of fluxing elements inside the footwall and hanging wall resulted in crystallization of large- to giant-size

crystals. The core of the dike had hydrous concentrations of B, Li, Cs, and Rb. A discontinuous perthite zone formed above the core zone. Half of the perthite zone was replaced by autometasomatic gaseous Na-rich melt that formed upward-tapering bodies, which contained gemstone-bearing miarolitic cavities. Miarolitic cavities ruptured, dislodging and breaking first-generation quartz and tourmaline crystals that lined the miarolitic cavity walls. Following cavity rupture, second-generation mis-shapen quartz and tourmaline formed, followed by third-generation quartz and tourmaline crystals.

All major pegmatite districts in the NPRB are hosted by gabbro and/or tonalite. Most of the plutons hosting the pegmatites have only minor isotopic data available. One district, however, has adequate isotopic data available: the rare earth–bearing pegmatites in the Lakeview Mountains pluton. The pegmatites in the Lakeview Mountains pluton are the same age as the host tonalite, and initial Sr values of the pegmatites are essentially the same as the host tonalite. Based on the commonality of gabbro/tonalite-hosting pegmatites and similarity of Sr_i values and ages of the pegmatite and host pluton, we interpret the pegmatites of all these bodies in the NPRB as cogenetic not allogenic.

The two most critical elements in the interpretation that the Stewart pegmatite and pegmatites in the Lakeview Mountains pluton are cogenetic with their host gabbro/tonalite are the extensive initial Sr_i and isotopic age regional databases. Without the initial Sr_i database and zircon U/Pb age of the Pala gabbro, no defensible interpretation of the dike could be made, either allogenic or cogenetic. We conclude that establishment of regional initial Sr_i and isotopic age databases is essential to understanding the origin of granitic pegmatites.

APPENDIX

Major-element analysis was by conducted wavelength-dispersive X-ray fluorescence. Minor-element analysis was conducted by inductively coupled plasma–optical emission spectroscopy–mass spectroscopy (ICP-OES-MS) and sodium peroxide fusion (ICP). Fluoride was determined by ion-selective electrode (ISE) following a sodium hydroxide fusion. Chemical maps of tourmaline (Fig. 29) were obtained using a Horiba Instruments XGT-7000 micro X-ray fluorescence (mXRF) system. The samples were analyzed with an X-ray spot size of 100 mm. The maps are accumulations of four scans of 500 s for each accumulation and were acquired at 512 by 512 pixel resolution. The maps are the intensity counts of the corresponding energy peak selected to represent that element. In the case of the red-blue-green (RGB) image, it is a simple mix of the intensities of three elements, each assigned to red, green, or blue.

REFERENCES CITED

Adlakha, E.E., and Hattori, K., 2016, Paragenesis and composition of tourmaline types along the P2 fault and McArthur River uranium deposit, Athabasca Basin, Canada: Canadian Mineralogist, v. 54, p. 661–679, https://doi.org/10.3749/canmin.1500057.

Agranier, A., Lee, C.-T.A., Li, Z.-X.A., and Leeman, W.P., 2007, Fluid-mobile element budgets in serpentinized oceanic lithospheric mantle: Insights from B, As, Li, Pb, PGEs and Os isotopes in the Feather River ophiolite, California: Chemical Geology, v. 245, p. 230–241, https://doi.org/10.1016/j.chemgeo.2007.08.008.

Armstrong, R.L., and Suppe, J., 1973, Potassium-argon geochronometry of Mesozoic igneous rocks in Nevada, Utah, and southern California: Geological Society of America Bulletin, v. 84, p. 1375–1391, https://doi.org/10.1130/0016-7606(1973)84<1375:PGOMIR>2.0.CO;2.

Bose, E. and Wittich, E., 1913, Infoirme relativa a la exploracion de laregion norte de costa occidental de la Baja Californa: Parergones del Inst. Geol. Mexico, v. 4, p. 307–529.

Benton, L.D., Ryan, J.G., and Tera, F., 2001, Boron isotope systematics of slab fluids as inferred from a serpentine seamount, Mariana forearc: Earth and Planetary Science Letters, v. 187, p. 273–282, https://doi.org/10.1016/S0012-821X(01)00286-2.

Cerny, P., London, D., and Novak, M., 2012, Granitic pegmatites as reflections of their sources: Elements, v. 8, p. 289–294, https://doi.org/10.2113/gselements.8.4.289.

Chan, L.H., Leeman, W.P., and You, C.F., 1992, Lithium isotopic composition of Central American volcanic arc lavas: Implications for modification of subarc mantle by slab-derived fluids: Chemical Geology, v. 160, p. 255–280.

Clausen, B.L., Morton, D.M., Kistler, R.W., and Lee, C.-T.A., 2014, Low-initial-Sr felsic plutons of the northwestern Peninsular Ranges batholith, southern California, and the role of mafic-felsic magma mixing in continental crust formation, in Morton, D.M., and Miller, F.K., eds., Peninsular Ranges Batholith, Baja California and Southern California: Geological Society of America Memoir 211, p. 317–344.

Ertl, A., Rossman, G.R., Hughes, J.M., London, D., Wang, Y., O'Leary, J.A., Dyar, M.D., Prowatke, S., Ludwig, T., and Tillmanns, E., 2010, Tourmaline of the elbaite-schorl series from the Himalaya Mine, Mesa Grande, California: A detailed investigation: The American Mineralogist, v. 95, p. 24–40, https://doi.org/10.2138/am.2010.3271.

Fairbanks, F.H., 1893, Notes on the occurrence of rubellite and leopidolite in southern California: Science, v. 21, p. 35–36, https://doi.org/10.1126/science.ns-21.520.35-a.

Farner, M.J., and Lee, C.-T.A., 2017, Effects of crustal thickness on magmatic differentiation in subduction zone volcanism: A global study: Earth and Planetary Science Letters, v. 470, p. 96–107, https://doi.org/10.1016/j.epsl.2017.04.025.

Fleet, M.E., 2003, Sheet silicates, in Fleet, M.E., Rock-Forming Minerals: Volume 3A, Micas (2nd ed.): London, The Geological Society, p. 651–690.

Foord, E.E., 1991, Geologic setting, in Walawender, M.J., and Hanan, B.B., eds., Geological Excursions in Southern California and Mexico: San Diego, California, San Diego State University, Department Geological Sciences, p. 129–130.

Foord, E.E., and Shigley, J.E., 1991, Description of the pegmatites, in Walawender, M.J., and Hanan, B.B., eds., Geological Excursions in Southern California and Mexico: San Diego, California, San Diego State University, Department Geological Sciences, p. 130–132.

Frondel, C., 1962, The System of Mineralogy: Volume III, Silica Minerals: New York, John Wiley and Sons, 334 p.

Hanley, J.B., 1951, Economic Geology of the Rincon Pegmatites, San Diego County, California: California Division of Mines Special Report 7-B, 24 p.

Huang, W.-L., and Wyllie, P.J., 1986, Phase relationships of gabbro-tonalite-granite water at 15 kbar with applications to differentiation and anatexis: American Mineralogist, v. 71, p. 301–316.

Jahns, R.H., 1948, Discussion, in Gilluly, J., Chairman, Origin of Granite: Geological Society of America Memoir 28, p. 91–96.

Jahns, R.H., 1979, Gem bearing pegmatites in San Diego County, California: The Stewart Mine, Pala district, and the Himalaya Mine, Mesa Grande district, in Abbott, P.L., and Todd, V.R., eds., Mesozoic Crystalline Rocks: San Diego, California, San Diego State University, Department of Geological Sciences, p. 3–38.

Jahns, R.H., 1982, Internal evolution of pegmatite bodies, in Cerny, P., ed., Granitic Pegmatites in Science and Industry: Mineralogical Association of Canada Short Course 8, p. 293–327.

Jahns, R.H., and Burnham, C.W., 1969, Experimental studies of pegmatite genesis. I. A model for the derivation and crystallization of granitic pegmatites: Economic Geology and the Bulletin of the Society of Economic Geologists, v. 64, p. 843–864, https://doi.org/10.2113/gsecongeo.64.8.843.

Jahns, R.H., Swoboda, E.R., and Larson, W.F., 1974, Tourmaline-bearing pockets in pegmatites of the Pala district, San Diego County, California: Geological Society of America Abstracts with Programs, v. 6, p. 197–198.

Jahns, R.H., and Wright, L.A., 1951, Gem- and Lithium-Bearing Pegmatites of the Pala District, San Diego County, California: California Division of Mines Special Report 7-A, 72 p.

Kassoli-Fournaraki, A., and Michailidis, K., 1994, Chemical composition of tourmaline in quartz veins from Nea Roda and Thasos areas in Macedonia, northern Greece: Canadian Mineralogist, v. 32, p. 607–615.

Kennedy, M.K., 2000, Geologic map of the Pala 7.5' quadrangle, San Diego County, California: A Digital Database: California Division of Mines and Geology, scale 1:24,000.

Kimbrough, D.L., Grove, M., and Morton, D., 2015, Timing and significance of gabbro emplacement within two distinct plutonic domains of the Peninsular Ranges batholith, southern and Baja California: Geological Society of America Bulletin, v. 127, p. 19–37, https://doi.org/10.1130/B30914.1.

Kistler, R.W., Wooden, J.L., Premo, W.R., and Morton, D.M., 2014, Pr-Sr-Nd-O isotopic characterization of Mesozoic rocks throughout the northern end of the Peninsular Ranges batholith: Isotopic evidence for the magmatic evolution of oceanic arc–continental margin accretion during the Late Cretaceous of southern California, in Morton, D.M., and Miller, F.K., eds., Peninsular Ranges Batholith, Baja California and Southern California: Geological Society of America Memoir 211, p. 263–316.

Kunz, G.F., 1905, Gems, Jewelers' Materials, and Ornamental Stones of California: California Division of Mines Bulletin 37, 171 p.

Larsen, E.S., Jr., 1948, Batholith and Associated Rocks of the Corona, Elsinore, and San Luis Rey Quadrangles Southern California: Geological Society of America Memoir 29, 182 p., https://doi.org/10.1130/MEM29-p1.

Larsen, E.S., Jr., 1951, Crystalline rocks of the Corona, Elsinore, and San Luis Rey quadrangles, southern California, in Crystalline Rocks of Southwestern California: California Division of Mines Bulletin 159, p. 7–50.

Larsen, E.S., Jr., 1954, The Batholith of Southern California: California Division of Mines Bulletin 170, p. 25–30.

Lee, C.-T.A., and Morton, D.M., 2015, High silica granites: Terminal porosity and crystal settling: Earth and Planetary Science Letters, v. 409, p. 23–31, https://doi.org/10.1016/j.epsl.2014.10.040.

Li, Z.-X.A., and Lee, C.-T.A., 2006, Geochemical investigation of serpentinized oceanic lithospheric mantle in the Feather River ophiolite, California: Implications for the recycling rate of water by subduction: Chemical Geology, v. 235, p. 161–185, https://doi.org/10.1016/j.chemgeo.2006.06.011.

London, D., 2008, Pegmatites: The Canadian Mineralogist Special Publication 10, 347 p.

Martin, R.F., and De Vito, C., 2006, The patterns of enrichment in felsic pegmatites ultimately depend on tectonic setting: The Canadian Mineralogist, v. 43, p. 2027–2048.

McDougall, I., and Harrison, T.M., 1999, Geochronology and Thermochronology by the $^{40}Ar/^{39}Ar$ Method (2nd ed.): New York, Oxford University Press, 212 p.

Morton, D.M., Miller, F.K., Kistler, R.W., Premo, W.R., Lee, C.-T.A., Langenheim, J.L., Wooden, J.L., Snee, L.W., Clausen, B.L., and Cossette, P., 2014a, Framework and petrogenesis of the northern Peninsular Ranges batholith, southern California, in Morton, D.M., and Miller, F.K., eds., Peninsular Ranges Batholith, Baja California and Southern California: Geological Society of America Memoir 211, p. 61–143, https://doi.org/10.1130/2014.1211(03).

Morton, D.M., Kistler, R.W., Miller, F.K., Langenheim, V.E., Premo, W.R., Wooden, J.L., Cossette, P.M., and Jachens, R.C., 2014b, Lakeview Mountains pluton: A dynamically emplaced pluton, northern Peninsular Ranges batholith, southern California, in Morton, D.M., and Miller, F.K., eds., Peninsular Ranges Batholith, Baja California and Southern California: Geological Society of America Memoir 211, p. 395–420, https://doi.org/10.1130/2014.1211(11).

Noll, P.D., Jr., Newsome, H.E., Leeman, W.P., and Ryan, J.G., 1996, The role of hydrothermal fluids in the production of subduction zone magmas; evidence from siderophile and chalcophile trace elements and boron: Geochimica et Cosmochimica Acta, v. 60, p. 587–611, https://doi.org/10.1016/0016-7037(95)00405-X.

Ortega-Rivera, A., 2003, Geochronological constraints on the tectonic history of the Peninsular Ranges batholith of Alta and Baja California: Tectonic implications for western Mexico, in Johnson, S.E., Paterson, S.R., Fletcher, J.M., Girty, G.H., Kimbrough, D.L., and Martin-Barajas, A., eds., Tectonic Evolution of Northwestern Mexico and the Southwestern U.S.A.: Geological Society of America Special Paper 374, p. 297–335, https://doi.org/10.1130/0-8137-2374-4.297.

Patterson, J.E., 2009, Fracture Mechanics and Geochemical Factors Influencing the Emplacement Mechanisms of the Stewart Lithia Gem Bearing Granitic Pegmatite, Pala District, San Diego County, California [Ph.D. thesis]: Calgary, Alberta, Canada, University of Calgary, 502 p.

Pieczka, A., Golebiowska, B., Jelen, P., Wlodek, A., Szeleg, E., and Szuszkiewicz, A., 2018, Towards Zn-dominant tourmaline: A case of Zn-rich fluor-elbaite and elbaite from the Julianna System at Pilawa Gorna, Lower Silesia, SW Poland: Minerals (Basel), v. 8, p. 126, https://doi.org/10.3390/min8040126.

Premo, W.R., Morton, D.M., Wooden, J.L., and Fanning, C.M., 2014, U-Pb zircon geochronology of plutonism in the northern Peninsular Ranges batholith, southern California: Implications for the Late Cretaceous tectonic evolution of southern California, in Morton, D.M., and Miller, F.K., eds., Peninsular Ranges Batholith, Baja California and Southern California: Geological Society of America Memoir 211, p. 145–180, https://doi.org/10.1130/2014.1211(04).

Roda-Robles, E., Pesquera, A., Gill, P.P., Torres-Ruiz, J., and Fontan, F., 2004, Tourmaline from the rare-element Pinilla pegmatite (Central Iberian zone, Zamora, Spain): Chemical variation and implications for pegmatitic evolution: Mineralogy and Petrology, v. 81, p. 249–263, https://doi.org/10.1007/s00710-004-0042-8.

Schaller, W.T., 1912, New manganese phosphates from the gem tourmaline field of southern California: Washington Academy of Science Journal, v. 2, p. 143–145.

Sharp, R.V., 1967, San Jacinto fault zone in the Peninsular Ranges of southern California: Geological Society of America Bulletin, v. 78, p. 705–729, https://doi.org/10.1130/0016-7606(1967)78[705:SJFZIT]2.0.CO;2.

Shigley, J.E., 1991, The Stewart lithia mine, in Walawender, M.J., and Hanan, B.B., eds., Geological Excursions in Southern California and Mexico: San Diego, California, San Diego State University, Department Geological Sciences, p. 132–134.

Shigley, J.E., and Brown, G.E., Jr., 1985, Occurrence and alteration of phosphate minerals at the Stewart pegmatite, Pala district, San Diego County, California: The American Mineralogist, v. 70, p. 395–408.

Silver, L.T., and Chappell, B.W., 1988, The Peninsular Ranges batholith: An insight into the evolution of the Cordilleran batholiths of southwestern North America: Transactions of the Royal Society of Edinburgh–Earth Sciences, v. 79, p. 105–121, https://doi.org/10.1017/S0263593300014152.

Snee, L.W., and Foord, E.E., 1991, $^{40}Ar/^{39}Ar$ geochronology and thermochronology of the granitic pegmatites of San Diego County, California, in Walawender, M.J., and Hanan, B.B., eds., Geological Excursions in Southern California and Mexico: San Diego, California, San Diego State University, Department Geological Sciences, p. 139.

Soares, D.R., Beurlen, H., Barreto, S.B., Da Silva, M.R.R., Ferreira, A.C.M., and Anastacio, E.M., 2008, Compositional variation of tourmaline-group minerals in the Borborema Pegmatite Province, northeastern Brazil: Canadian Mineralogist, v. 46, p. 1097–1116, https://doi.org/10.3749/canmin.46.5.1097.

Soares, D.R., Beurlen, H., Fetteira, A.C.M., Gomes, M.M.C., Barreto, S.B., and Anastacio, E.M., 2009, Elevated zinc contents in elbaites from pegmatites of Borborema Pegmatite Province, NE Brazil: Estudos Geologicos, v. 9, no. 2, p. 348–351.

Taylor, B.E., Foord, E.E., and Friedrichsen, H., 1979, Stable isotope and fluid inclusion studies of gem-bearing granitic pegmatite-aplite dikes, San Diego Co., California: Contributions to Mineralogy and Petrology, v. 68, p. 187–205, https://doi.org/10.1007/BF00371900.

Tindle, A.G., Selway, J.B., and Breaks, F.W., 2005, Liddicoatite and associated species from the McCombe spodumene-subtype rare-earth granitic pegmatite northwestern Ontario, Canada: Canadian Mineralogist, v. 43, p. 769–793, https://doi.org/10.2113/gscanmin.43.2.769.

Todd, V.R., Shaw, S.R., and Hammarstrom, J.M., 2003, Cretaceous plutons of the Peninsular Ranges batholith, San Diego and westernmost Imperial Counties, California: Intrusions across a Late Jurassic continental margin, in Johnson, S.E., Paterson, S.R., Fletcher, J.M., Girty, G.H., Kimbrough, D.L., and Martin-Bara, A., eds., Tectonic Evolution of Northwestern Mexico and the Southwestern USA: Geological Society of America Special Paper 374, p. 185–235, https://doi.org/10.1130/0-8137-2374-4.185.

Todd, V.R., Hernandez, J.L., and Busch, L.L., 2014, The zoned Ramona plutonic complex and Early Cretaceous mid- to upper-crustal intrusive sequence, Peninsular Ranges batholith, southern California, in Morton, D.M., and Miller, F.K., eds., Peninsular Ranges Batholith, Baja California and Southern California: Geological Society of America Memoir 211, p. 583–608, https://doi.org/10.1130/2014.1211(17).

Tulloch, A.J., and Kimbrough, D.L., 2003, Paired plutonic belts in convergent margins and the development of high Sr/Y magmatism: Peninsular Ranges batholith of Baja California and Median batholith of New Zealand, in Johnson, S.E., Paterson, S.R., Fletcher, J.M., Girty, G.H., Kimbrough, D.L., and Martin-Barajas, A., eds., Tectonic Evolution of Northwestern Mexico and the Southwestern U.S.A.: Geological Society of America Special Paper 374, p. 275–295, https://doi.org/10.1130/0-8137-2374-4.275.

Walawender, M.J., Gastil, R.G., Clinkenbeard, J.P., McCormick, W.V., Eastman, B.G., Wernicke, R.S., Wardlaw, M.S., Gunn, S.H., and Smith, B.M., 1990, Origin and evolution of the zoned La Posta–type plutons, eastern Peninsular Ranges batholith, southern and Baja California, in Anderson, J.L., ed., The Nature and Origin of Cordilleran Magmatism: Geological Society of America Memoir 174, p. 1–18

Webber, K.L., Simmons, W.B., and Falster, A.U., 1999, Cooling rates and crystallization dynamics of shallow level pegmatite-aplite dikes, San Diego County, California: The American Mineralogist, v. 84, p. 708–717, https://doi.org/10.2138/am-1999-5-602.

Weber, F.H., Jr., 1963, Mines and Mineral Resources of San Diego County, California: California Division of Mines and Geology County Report 3, 309 p.

Woodford, A.O. and Harriss, T.F., 1938, Geological reconnaissance across Sierra San Pedro Martir, Baja California: Geological Society of America Bulletin, v. 45, p. 1297–1336.